University of Zurich[UZH]

LOW ENERGY CALIBRATION FOR GERDA AND CHARACTERIZATION OF WAVELENGTH-SHIFTERS AND REFLECTORS IN LIQUID ARGON FOR LEGEND-200

MASTER'S THESIS

Vera Hiu-Sze Wu

from

HONG KONG SAR

Zurich, May 2021

Supervisors:

Prof. Dr. Laura Baudis

Dr. Junting Huang

Dr. Neil McFadden

Dr. Chloe Ransom

MSc Gabriela R. Araujo

Summary

Neutrinos, being the only electrically neutral fermions in the Standard Model, might be Majorana particles, i.e. particles that are their own antiparticles. The Majorana nature of neutrino will imply that neutrinos acquire masses through the seesaw mechanism and that it is possible to explain the matter-antimatter asymmetry problem through leptogenesis [51].

The GERDA and LEGEND experiments are two experiments dedicated to determine the Majorana nature of neutrinos, by searching for neutrinoless double-beta decay ($0\nu\beta\beta$), a lepton-number violating process. They use high purity germanium detectors enriched in ^{76}Ge, the isotope that undergoes double-beta decay. If neutrinos are indeed Majorana particles, apart from the ordinary two neutrinos double-beta decay, the isotope would have a probability of undergoing $0\nu\beta\beta$, producing a peak at the Q-value in the summed energy spectrum.

This thesis is divided into two parts. The first part explains the low energy calibration for GERDA. Motivated by the physics of low-energy searches and better background modelling, a special calibration run with a lower threshold was conducted. The goal for this project is to determine, by analyzing the data from the special calibration, whether extrapolating the existing calibration curves down to the low energy region is valid. From the analysis, it is found that the assumption of linear energy response of the detector down to the lower energy region is valid.

The second part describes the optical characterization of wavelength-shifters and reflectors in liquid argon (LAr). Mainly two samples were tested, including the witness sample of wavelength-shifting reflectors (WLSR) used in LEGEND-200, which is a reflective foil, Tetratex® (TTX), coated with tetraphenyl butadiene (TPB). Another sample was a non-optically coupled combination of polyethylene naphthalate (PEN) and TTX. The goal of the experiment is to measure the shifted and reflected light yield of the samples in LAr. The experimental results show that both samples increase light yield in LAr compare to the setup without the wavelength-shifting and reflective samples. While the light yield enhancement of WLSR is more compared to the composite of PEN and TTX in the experiment, it does not imply that the quantum efficiency of the former is greater. A quantitative result on the efficiency of the samples can only be made with the help of simulation, which is not part of this work.

Chapter 1 provides an introduction to $0\nu\beta\beta$ together with the motivation to search for such a rare decay. Chapter 2 describes the two experiments, GERDA and LEGEND. Chapter 3 is on the low energy calibration for GERDA PhaseII+ data. It covers the motivation for this calibration, the methodology, and the results. Chapter 4 discusses the optical characterization project. The details of the experiment, including the motivations, the properties of the samples, the experimental setup and procedures, the analysis, and the results, are reported. Chapter 5 provides the conclusion of both projects and the outlook of the LEGEND experiment.

Acknowledgements

During the two-year journey of my master's study in the Physics Institute of the University of Zurich, the experience is fruitful and rewarding. It would have not been possible without the guidance, help, and companionship from many people that I have met.

Firstly, I would like to thank my supervisor, Prof. Dr. Laura Baudis, for giving me the opportunity to work in this field as a master's student and for her guidance and support. The experience in the group is fruitful and rewarding. Most importantly, I have found my interest in the field during the journey.

I would also like to express my gratitude to everyone in the group, especially the deepest one to Gabriela R. Araujo, who proposed the very interesting and well-designed hardware project and guided me through the challenges with a great amount of patience and understanding. In addition to the technical knowledge, I have also learned the logical way of thinking and gained inspiration from her through the tight cooperation for the experiment. My gratitude also goes to Dr. Junting Huang and Dr. Chloe Ransom for providing me guidance and helps with the calibration project. Besides, I would like to thank Adam, Frédéric, Kevin, Lars, Michelle, Neil, Patricia, Stefan, and Yanina for the discussions, helps, and/or inviting me for beers. To everyone I have met in the group, it has been a real pleasure to meet you all and the journey has been more colorful and easier with your presence. I wish you all the best and success!

I would like to thank the GERDA and the LEGEND collaboration for the warm welcoming. Although the time is short, it has been my pleasure to work for the collaborations. Also, I would like to give a special thanks to the chemistry department at the University of Zurich for being very helpful and lending us to use their spectroscopy in the laboratory.

In the end, I am very grateful for the help from Alvin, Angel, Karwai, Mannie for proofreading this work. I would also like to take this special opportunity to thank my family, my father, mother, and my sister, for their never-ending love, encouragement, and tolerance. Finally, a big thanks to Sharp for proofreading my thesis, for sharing my doubts and happiness all the time, and for the companionship in Zurich.

Table of Contents

List of Tables

List of Figures

Acronyms

$0\nu\beta\beta$ Neutrinoless Double Beta Decay

$2\nu\beta\beta$ Two Neutrino Double Beta Decay

MAJORANA Majorana Demonstrator

ADC Analog-to-digital Converter

BEGe Broad Energy Germanium

Coax Coaxial

CP Charge-parity

DAQ Data Acquisition

DC Dark Count

DEP Double Escape Peak

DPE Double Photoelectron

ER Electronic Recoil

FADC Flash Analog to Digital Converter

FEP Full Energy Peak

FWHM Full Width at Half Maximum

GAr Gas Argon

GERDA Germanium Detector Array

HPGe High-purity Germanium

IC Inverted coaxial

LAr Liquid Argon

LArS Liquid Argon Setup

LED Light-emitting Diode

LEGEND Large Enriched Germanium Experiment for Neutrinoless $\beta\beta$ Decay

LNGS Laboratori Nazionali del Gran Sasso

NR Nuclear Recoil

PE Photo-electron

PEN Polyethylene Naphthalate

PMNS Pontecorvo–Maki–Nakagawa–Sakata

PMT Photomultiplier Tube

PSD Pulse Shape Discrimination

PTFE Polytetrafluoroethylene

QE Quantum Efficiency

SEP Single Escape Peak

SiPM Silicon Photomultipliers

SM Standard Model

SPE Single Photoelectron

Super-WIMP Super Weakly Interacting Massive Particle

TPB Tetraphenyl Butadiene

TTX Tetratex®

VUV Vacuum Ultra-violet

WLSR Wavelength-shifting Reflector

ZAC Zero Area Cusp

Chapter 1

Introduction

Neutrinos are light, chargeless fermions in the Standard Model (SM). They only interact via the weak force. The neutrinos were first postulated by Wolfgang Pauli in December 1930 to resolve the "energy crisis" of beta decay [35]. At that time, scientists had been expecting to see a sharp energy peak of the beta particles, as in a two body decay. However, a continuous energy spectrum was observed instead. While Niels Bohr was about to abandon the energy conservation law to explain this disagreement between theory and observation, Pauli postulated the neutrino, an unnoticeable neutral particle carrying away the energy in the beta decay [35]. In 1934, Fermi formulated a theory to explain beta decay with neutrinos [79] under the postulate that neutrinos interact very weakly. After more than 30 years, in 1956, Cowan and Reines obtained the first evidence of the existence of electron neutrino through inverse beta decay [43]:

$$\bar{\nu}_e + p \rightarrow n + e^+. \tag{1.1}$$

Due to the tiny interaction cross-section of less than 10^{-44} cm^2, the detector had to be placed next to the nuclear reactor, an intense source of neutrinos, for the first detection of neutrino.

With the subsequent efforts of physicists, more information regarding neutrinos was revealed, including the different flavors of neutrinos [44, 59]. In addition, neutrino oscillations (Section 1.1) were confirmed in 1998 and 2002 [50, 28], implying that neutrinos have non-zero masses.

Neutrinos are the least understood particles in the SM. The study of neutrinos is an active field for the following reasons. Firstly, the SM has yet to provide a full picture for how neutrinos acquire masses (Section 1.2). Besides, the mass of neutrino is much smaller than the masses of other fundamental fermions, which appears to be caused by new physics. Secondly, in case neutrinos are Majorana particles, which are particles being their own anti-particles, lepton number is not conserved and may explain the matter-antimatter asymmetry (Section 1.3).

In the following section, more details of neutrino oscillation (Section 1.1), the mass origin of neutrino (Section 1.2), and the matter-antimatter problem (Section 1.3) are covered, followed by the introduction of neutrinoless double-beta ($0\nu\beta\beta$) decay. Finally, the current

status and outlook for $0\nu\beta\beta$ decay is summarized (Section 1.5).

1.1 Neutrino Oscillation

Neutrino flavor eigenstates, ν_α, are the superposition of the neutrino mass eigenstates, ν_i:

$$\nu_\alpha = \sum_{i=1}^{3} U_{\alpha i}\nu_i, \tag{1.2}$$

with α being e, μ, τ. $U_{\alpha i}$ is the unitary Pontecorvo–Maki–Nakagawa–Sakata (PMNS) matrix:

$$U = \begin{pmatrix} 1 & 0 & 0 \\ 0 & c_{23} & s_{23} \\ 0 & -s_{23} & c_{23} \end{pmatrix} \begin{pmatrix} c_{13} & 0 & s_{13}e^{-i\delta} \\ 0 & 1 & 0 \\ -s_{13}e^{i\delta} & 0 & c_{13} \end{pmatrix} \begin{pmatrix} c_{12} & c_{12} & 0 \\ -s_{12} & c_{12} & 0 \\ 0 & 0 & 1 \end{pmatrix} \begin{pmatrix} 1 & 0 & 0 \\ 0 & e^{i\alpha_1} & 0 \\ 0 & 0 & e^{i\alpha_2} \end{pmatrix}, \tag{1.3}$$

where $c_{ij} \equiv \cos\theta_{ij}$, $s_{ij} \equiv \sin\theta_{ij}$, δ is the charge-parity (CP) violating phase, and α_1 and α_2 are the Majorana phases. All the phases have values ranging from 0 to 2π. α_1 and α_2 are non-zero only if neutrinos are Majorana particles.

In the case where the neutrino travels a distance x in vacuum, the oscillation probability from ν_α to ν_β is given by:

$$\begin{aligned} P(\nu_\alpha \to \nu_\beta) = \delta_{\alpha\beta} &- 4\sum_{i<j}^{3} \mathrm{Re}(U_{\alpha i}U^*_{\beta i}U^*_{\alpha j}U_{\beta j}) \sin^2\left(\frac{\Delta m^2_{ij}x}{4E}\right) \\ &+ 2\sum_{i<j}^{3} \mathrm{Im}(U_{\alpha i}U^*_{\beta i}U^*_{\alpha j}U_{\beta j}) \sin\left(\frac{\Delta m^2_{ij}x}{2E}\right), \end{aligned} \tag{1.4}$$

where $\delta_{\alpha\beta}$ is the Kronecker delta, $\Delta m^2_{ij} \equiv m^2_i - m^2_j$, E is the average energy of the initial neutrino [81]. If neutrinos are massless or the three mass eigenstates have the same mass, oscillations do not occur.

Neutrino oscillations were first observed by Super-Kamiokanda Observatory with atmospheric neutrinos in 1998 [50], and Sudbury Neutrino Observatory with solar neutrinos in 2002 [28]. The mass difference and the mixing angles have been measured by different experiments, such as the KamLAND experiment [49], the Daya-Bay experiment [32], and the T2K experiment [8]. For the mass-squared differences, the values is measured to be $\Delta m^2_{21} \sim 7.5 \times 10^{-5}$ eV^2 and $|\Delta m^2_{31}| \sim 2.5 \times 10^{-3}$ eV^2 [81]. While the sign of Δm^2_{21} is determined to be positive, meaning $m^2_2 > m^2_1$, that of Δm_{31} has not yet been determined. Hence, there are two possible orders of the masses, normal and inverted, as shown in Fig. 1.1.

1.2 Neutrino Mass

Although neutrinos have been confirmed to have mass by the fore-mentioned experiments, the mechanism of how they acquire mass is still unknown. Besides, the upper limit of

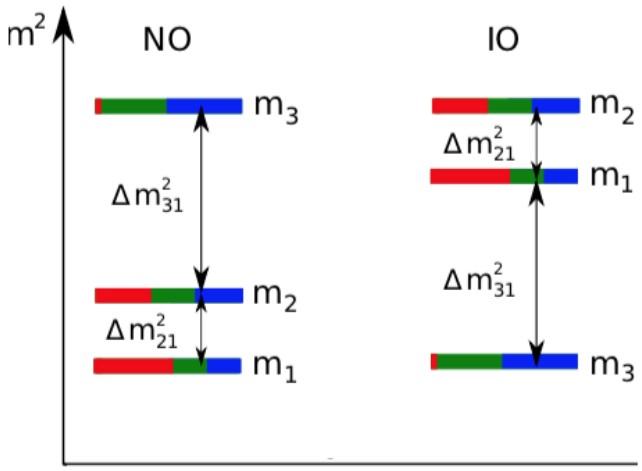

Figure 1.1: Possible mass ordering. NO refers to normal ordering with $\Delta m_{31} > 0$. IO refers to inverted ordering, with $\Delta m_{31} < 0$. Different colors illustrate the mixing components of different flavors for the mass eigenstates. Figure from [69].

neutrino mass is way smaller from the other fundamental fermions: the sum of the three neutrino mass is smaller than $0.11 - 0.54$ eV from cosmological measurements [81]. One possible explanation is that they obtain mass through electroweak symmetry breaking, similar to other fermions [45]. The SM can be extended with an extra Yukawa interaction term involving the right-chiral neutrino which does not interact weakly. Then, the neutrino acquires a Dirac mass m_D [45]:

$$m_D = \frac{v\lambda}{\sqrt{2}}, \tag{1.5}$$

where v is the vacuum expectation value of the Higgs field and λ is the Yukawa coupling. To explain why neutrino mass is much smaller than that of other fermions, their coupling to the Higgs boson has to be unnaturally small.

A more favourable theory is the seesaw mechanism, through which neutrinos acquire Majorana masses in addition to Dirac mass. To acquire Majorana mass, neutrinos have to be Majorana particles. In this case, the mass matrix, M, of neutrino is given by [45]:

$$M = \begin{pmatrix} 0 & m_D \\ m_D & m_R \end{pmatrix}, \tag{1.6}$$

where m_R is the Majorana mass. In case $m_R \ll m_D$, the eigenvalues of this mass matrix, which are the physical mass, become:

$$\lambda_+ \approx m_R, \qquad \lambda_- \approx m_D \frac{m_D}{m_R}. \tag{1.7}$$

Hence, the heavier m_R is, the lighter λ_- becomes. Such seesaw mechanism naturally accounts for the low neutrino mass, should neutrinos be Majorana particles.

1.3 Matter-Antimatter Asymmetry Problem

In the current SM, the three kinds of interaction, the electromagnetic interaction, the weak interaction, and the strong interaction, would only produce equal numbers of particles and anti-particles. Hence, SM predicts an equal amount of matter and anti-matter in the universe. However, the universe today is dominated by matter. Observations disfavor the possibility that anti-matter exists in significant amount in another corner of the universe [37]. Besides, the He/p ratio today requires asymmetry between particle and anti-particle. The dilemma between the SM and the existing universe is called the matter-antimatter asymmetry problem.

To create the matter-dominated universe today, and assuming that the asymmetry happened after inflation, the ratio of particle to antiparticle has to be around $(10^9 + 3)/10^9$ as predicted by the radiation-matter ratio at that time [37]. To achieve the asymmetry, Sakharov proposed three criteria [73]. Firstly, the universe was not in thermal equilibrium when the asymmetry was first created. This could be easily met at the time soon after the inflation. Secondly, CP-violation is needed. Although CP-violation has already been measured in quarks, baryonic CP-violation alone is not sufficient to account for the low amount of antiparticles in the universe. Hence, experiments have been conducted to look for the leptonic CP violation. From the most recent result by T2K [9], the possibility that lepton does not violate CP is excluded up to 3σ, and the most probable violating phase is close to the maximal violation. Finally, Baryon number violation is required. Lepton number violation induces baryon number violation via leptogenesis [51], and if neutrinos are Majorana particles, lepton number must not conserve.

1.4 Neutrinoless Double-beta Decay

For certain isotopes, as listed in Table 1.1, single-beta decay is forbidden, and they undergo double-beta decay as shown in Fig. 1.2 using ^{76}Ge as an example.

Table 1.1: List of isotopes for the search of $0\nu\beta\beta$ decay. The list is not exhaustive. Table adapted from [69]. $Q_{\beta\beta}$ is the energy released during the decay and $G^{0\nu}$ is the phase space integral.

Isotopes	$Q_{\beta\beta}$[keV]	Natural abundance [%]	$G^{0\nu}[10^{-14}\text{yr}^{-1}]$
^{76}Ge	2039.1	7.8	0.623
^{82}Se	2995.5	9.2	2.70
^{100}Mo	3035.0	9.6	4.36
^{130}Te	2530.3	34.5	4.09
^{136}Xe	2461.9	8.9	4.31

If neutrinos are Majorana particles, $0\nu\beta\beta$ decay is allowed. The Feynman diagram of double-beta decay is shown in Fig. 1.3. For the diagram on the right, which illustrates the $0\nu\beta\beta$ decay, as the neutrino was absorbed by the antineutrino, it is clear that the lepton number for such reaction is not conserved, with $\Delta L = +2$.

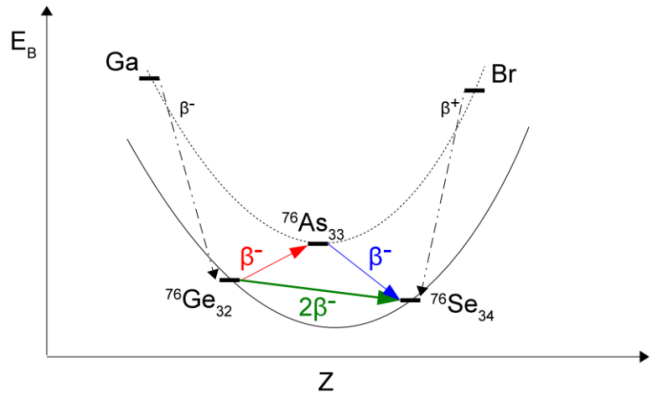

Figure 1.2: Mass parabolas showing that ^{76}Ge undergoes double-beta decay, as the single beta decay is energetically forbidden. Figure from [77].

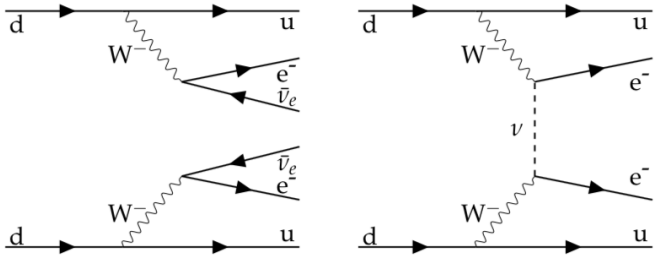

Figure 1.3: The Feynman diagrams for (left) $2\nu\beta\beta$ and (right) $0\nu\beta\beta$. Figure from [72].

If $0\nu\beta\beta$ decay is observed, the Majorana nature of neutrino can be confirmed, which will then naturally explain the lightness of neutrino mass compare to other fermions. Besides, leptonic number violation, of which $0\nu\beta\beta$ decay is the smoking gun, helps to account for matter-antimatter asymmetry problem.
For the exchange of light Majorana neutrino, the half life of $0\nu\beta\beta$ decay is [67]:

$$T_{1/2}^{0\nu\beta\beta} = \frac{1}{G^{0\nu}|M^{0\nu}|^2|m_{\beta\beta}|^2}, \tag{1.8}$$

where $G^{0\nu}$ is the phase space integral as listed in Table 1.1, $M^{0\nu}$ is the nuclear matrix element and $m_{\beta\beta}$ is the effective Majorana mass for electron neutrino. $m_{\beta\beta}$ is then related to masses of mass eigenstates by:

$$|m_{\beta\beta}| = \left|\sum_{i}^{3} U_{ei}^2 m_i\right|. \tag{1.9}$$

For the case of two neutrino double-beta ($2\nu\beta\beta$) decay, the spectrum of two electrons is a continuum, while for $0\nu\beta\beta$, the electrons no longer share their energies with neutrinos, and hence, a sharp peak at the Q-value in the summed energy spectrum will be observed if $0\nu\beta\beta$ decay exists.

The sensitivity of the half life $S_{1/2}^{0\nu}$ is given by [72]:

$$S_{1/2}^{0\nu} = \ln 2 \cdot \frac{f_{enr} N_A \epsilon}{A} \sqrt{\frac{M \cdot t}{BI \cdot \Delta}}, \tag{1.10}$$

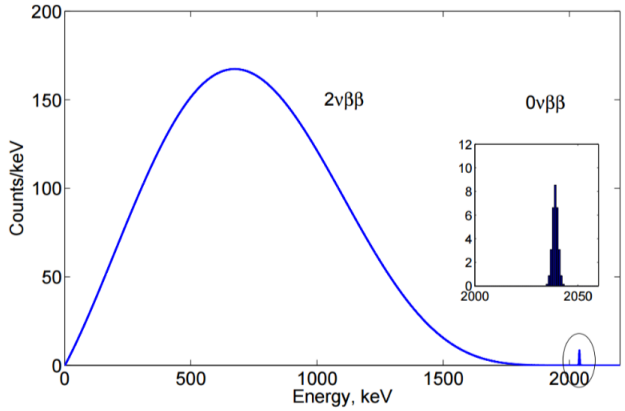

Figure 1.4: Drawing of the possible energy Spectrum of the ^{76}Ge double-beta decay. If $0\nu\beta\beta$ exist, the sharp peak at (2039.006 $\pm$ 0.050) keV, which is the Q-value, will be detected [48]. Figure from [77].

where f_{enr} is the enrichment fraction, N_A is the Avogadro's constant, A is the atomic mass of the isotope, ϵ is the detection efficiency, M is the active mass of the source, t is the exposure time, BI is the background index and Δ is the energy resolution. $M \cdot t$ is the total exposure of the experiment. A higher sensitivity requires higher enrichment fraction, greater active mass, higher detection efficiency, better energy resolution, lower background environment, and longer exposure time.

In case $BI \cdot M \cdot t \cdot \Delta < 1$, the experiment enters the "background free" regime, where the sensitivity becomes [72]:

$$S_{1/2}^{0\nu} \propto f_{enr} \cdot \epsilon \cdot M \cdot t. \tag{1.11}$$

Instead of scaling with $\sqrt{t}$, the sensitivity scales linearly with the exposure time. Hence entering the background free regime is also vital in searching for $0\nu\beta\beta$.

1.5 Experiments Searching for $0\nu\beta\beta$ Decay

The conditions for higher sensitivity in Eq. 1.10 is difficult to be satisfied all at once, and different isotopes in Table 1.1 have different advantages. For example, ^{130}Te has a naturally high f_{enr}; ^{82}Se and ^{100}Mo have higher Q-values, leading to a lower BI and less $2\nu\beta\beta$ background [72]. Besides, we should also consider if the sample is easily scalable, such that M can be increased for future experiments. The germanium crystal and liquid xenon detectors would be quite managable for scaling up. Because of all these factors, experiments use different isotopes for the search of $0\nu\beta\beta$. Table 1.2 summarized the current competitive limits set on $T_{1/2}^{0\nu\beta\beta}$ using different isotopes, as well as the projected sensitivities in future experiments. ^{136}Xe and ^{76}Ge have relatively better sensitivities. The current best lower limit for the half-life of $0\nu\beta\beta$ decay is set by Germanium Detector Array (GERDA) at 1.8×10^{26} yr at 90% confidence level [24].

Table 1.2: Current competitive sensitivity of the half life of $0\nu\beta\beta$ decay and $\langle m_{\beta\beta}\rangle$ in different experiments.

Experiment	Isotope	$T^{0\nu}_{1/2}$ limit [yr] (90% CL)	$\langle m_{\beta\beta}\rangle$ limit [meV]
GERDA [24]	^{76}Ge	1.8×10^{26}	$79 - 180$
CUORE [15]	^{130}Te	2.2×10^{25}	$90 - 305$
EXO-200 [33]	^{136}Xe	3.5×10^{25}	$78 - 239$
KamLAND-Zen [52]	^{136}Xe	1.07×10^{26}	$61 - 165$
Future Experiment	**Isotope**	**$T^{0\nu}_{1/2}$ discovery sensitivity [yr] (3σ)**	**$\langle m_{\beta\beta}\rangle$ [meV] (3σ)**
LEGEND-200 [11]	^{76}Ge	1×10^{27} (5 years data-taking)	$37 - 78$
LEGEND-1000 [11]	^{76}Ge	1.3×10^{28} (10 years data-taking)	$9 - 21$
CUPID [34]	^{100}Mo	1.1×10^{27} (10 years data-taking)	$12 - 20$
SNO+ [29]	^{130}Te	2.1×10^{26} (5 years data-taking)	$30 - 200$
DARWIN [20]	^{136}Xe	1.1×10^{27} (10 years data-taking)	$18 - 46$
nEXO [16]	^{136}Xe	0.74×10^{28} (10 years data-taking)	< 15
KamLAND2-ZEN [71]	^{136}Xe	-	~ 20

Chapter 2

The GERDA and LEGEND experiments

The GERDA and the MAJORANA DEMONSTRATOR (MAJORANA) experiments are the predecessors of the Large Enriched Germanium Experiment for Neutrinoless $\beta\beta$ Decay (LEGEND) experiment. All these experiments use high-purity germanium (HPGe) detectors enriched in ^{76}Ge, to search for $0\nu\beta\beta$ decay. As mentioned in the previous section, the signature is a peak at the Q-value of (2039.006 $\pm$ 0.050) keV as shown in Fig. 1.4 [48].

GERDA released its final result in 2020, setting a lower limit for the half life of $0\nu\beta\beta$ decay at 1.8×10^{26} yr [24]. Currently, the LEGEND-200 experiment, which is the first stage of the LEGEND experiment, has already taken over the GERDA infrastructure at Laboratori Nazionali del Gran Sasso (LNGS). It is currently in the hardware installation and the initial testing phase. The data taking process is expected to begin at the end of 2021. Table 2.1 summarizes the latest information on the GERDA, the MAJORANA, and the LEGEND-200 experiment.

Table 2.1: Summary of the latest results and expectation of the germanium experiments, GERDA, MAJORANA and LEGEND-200.

	GERDA Phase II [24]	MAJORANA[30]	LEGEND-200 (intended) [11]
Active mass [kg]	44.2	29.7	200
Enriched ^{76}Ge	$\sim$87%	88%	88% [70]
Exposure [kg yr]	103.7	26.0$\pm$0.5	1000
Resolution at $Q_{\beta\beta}$ [keV]	3.0 [27]	2.53	2.5
BI [cts/(keV kg yr)] [11]	5.2 $\times10^{-4}$	(4.7$\pm$0.8) $\times$ 10^{-3}	2×10^{-4}
$T_{1/2}^{0\nu\beta\beta}$ [yr] (90% confidence level)	$> 1.8 \times 10^{26}$	$> 2.7 \times 10^{25}$	10^{27}

In the following sections of this chapter, the properties of germanium detectors and the detection mechanism are explained, followed by detailed descriptions of the GERDA and the LEGEND-200 experiment.

2.1 Germanium Detectors for $0\nu\beta\beta$ Decay

As shown in Eq. (1.10), higher sensitivity of detecting $0\nu\beta\beta$ decay requires larger target mass, longer observation time, higher enrichment fraction, finer energy resolution, lower background rate, and higher signal efficiency. The germanium detectors are a good choice for a high sensitivity experiment. Firstly, they have excellent energy resolution, low internal background and high radio purity [46]. Secondly, they have high detection efficiency, as they act as both the source of $0\nu\beta\beta$ decay and the detector at the same time. Besides, the enrichment technology of ^{76}Ge is well established and industrialized [11].

The HPGe detector is a p-i-n junction, a bulk intrinsic semiconductor sandwich between the highly doped p-type and n-type semiconductors. The intrinsic material of the germanium detector is also p-type but with low impurities, and hence has a low amount of free charge carriers. In contrast, the highly doped p-type and n-type layers contain holes and electrons as their majority carriers respectively. Due to the concentration gradient, the majority carriers of the doped layers diffuse to the intrinsic layer. The depletion region with electric field is then developed inside the intrinsic layer. The n-type layer acts as the cathode with excess positive charge carriers while the p-type layer acts as the anode.

As shown in Fig. 2.1, when radiations and decays deposit the energy in the intrinsic layer, a proportional amount of electron-hole pairs will be created. The pairs are then separated by the strong electric field inside the layer and drift to the electrodes, leading to a flow of current and, thus, generating the electronic signal for readout.

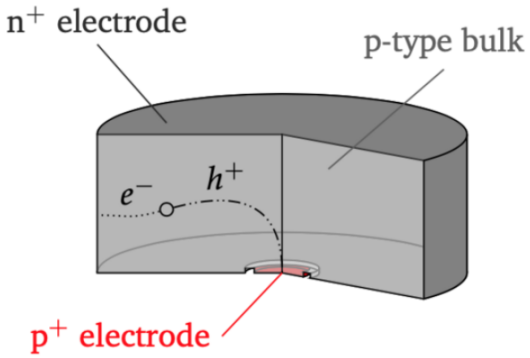

Figure 2.1: Sketch of one of the germanium detector types. "n+ electrode" refers to the n-type cathode, "p+ electrode" refers to the p-type anode. "+" indicates that the layer is heavily doped. "p-type bulk" refers to the intrinsic layer. When the interaction, as indicated by the circle, happens in the intrinsic layer, electron-hole pairs are created. The electrons drift to the n+ electrode while the holes to the p+ electrode. Figure from [67].

In case of thermal excitation, electrons would be excited to the conduction band, inducing an undesired current called the leakage current. Hence, the detectors are operated at cryogenic temperature to minimize the thermal excitation, thus the leakage current [67].

Types of Germanium Detectors

In the GERDA and LEGEND experiments, three types of enriched detectors were used, including the Broad Energy Germanium (BEGe) detector, the inverted coaxial (IC) detectors, and the coaxial (Coax) detectors. Their shapes are shown in Fig. 2.2. Although BEGe detectors had good performance, a larger size detector is more preferable as the amount of auxiliary material, such as cables, can be reduced per detector mass [78]. Therefore, in Phase II, five IC detectors, which is larger than the BEGe detectors, were used to replace the six detectors in Phase I.

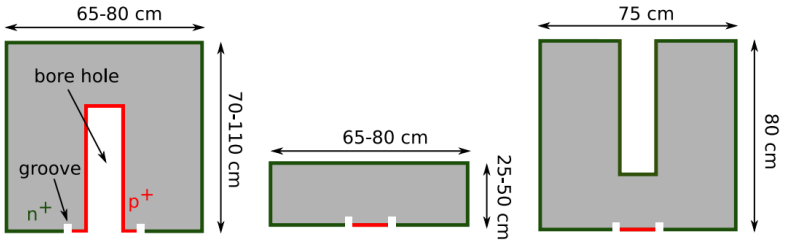

Figure 2.2: Shape of the three kinds of enriched germanium detectors. (Left) BEGe, (middle) Coax, and (right) IC detector. Figure from [72].

2.2 The GERDA Experiment

GERDA Phase I operated from November 2011 to September 2013, collecting a total exposure of 23.5 kg yr [21]. Afterwards, GERDA was upgraded to Phase II by adding the liquid argon (LAr) veto system and BEGe germanium detectors, which is introduced in Section 2.1. Phase II data taking started from December 2015, and ran till November 2019. An upgrade took place from May to July 2018, as shown in Fig. 2.3 when the data-taking stopped. During the upgrade, IC detectors were first deployed in this experiment, replacing one enriched coaxial detector and the former detectors with natural isotopic composition [78]. Besides, the instrumentation of LAr veto system was improved with better read-out and fiber curtain with higher density (Section 2.2.1) [78]. The total exposure for the entire Phase II period, i.e. before and after the upgrade, is listed in Table 2.1. In the later sections, the "pre-upgrade" period refers to the time before the upgrade, "Phase II+" refers to the time after upgrade [74].

In the following, the experimental configuration of Phase II and the signal reconstruction are introduced.

2.2.1 Experimental Setup for GERDA Phase II

The experiment was located 1400 m below the surface at LNGS. The rocks above the detector shield the cosmic rays by six orders of magnitude [24]. As shown in Fig. 2.4, the LAr cryostat is immersed inside a water tank with 590 m^3 purified water [24]. The purified

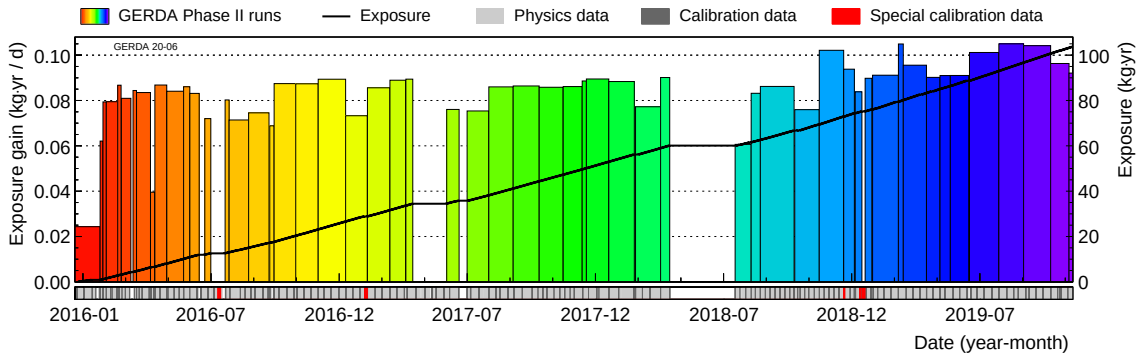

Figure 2.3: The exposure of GERDA Phase II. The axis on the right is for the accumulative exposure line, while that on the right is for the daily exposure. From May to July 2018, GERDA underwent 93 days of upgrade to Phase II+. After the upgrade, the daily exposure increased due to the slight increase of the total detector mass [78]. Figure from [74].

water further shields unwanted cosmic rays and neutrons. In addition, 66 Photomultiplier Tube (PMT) are installed on the walls of the tank to detect the Cherenkov radiation due to cosmic muons [67]. The LAr cryostat contained 64 m^3 LAr, cooling the detectors to their operating temperature as well as passively shielding more backgrounds radiations [78].

The detector array at the center of the cryostat was surrounded by the LAr veto system, which is shown on the right of Fig. 2.4. The LAr veto system aims at actively removing the events caused by external backgrounds using LAr scintillation light. Since the scintillation light peaks at 128 nm, which is lower than the detectable range of commercial photo-detectors, the light has to be shifted to visible (vis) light. Tetraphenyl Butadiene (TPB) was used in the experiment as the wavelength-shifter that shifts the LAr scintillation to visible light. The fiber curtain with 810 fibers coated with TPB was connected to silicon photomultipliers (SiPMs). Two copper shrouds with Tetratex® (TTX), which is a highly reflective fibre, coated with TPB were at the top and bottom of the fiber curtain. They were used to increase the light collection efficiency of the LAr veto system. 16 PMTs were installed at the top and bottom. Both types of photo-detectors detect the wavelength-shifted scintillation light near the detectors.

GERDA Phase II+ used three types of enriched detectors mentioned in 2.1. The detector strings had in total 41 detectors, with 30 BEGe detectors, 6 Coax detectors, and 5 IC detectors. They were mounted on seven strings as shown in Fig. 2.5. For the purpose of energy calibration, three radioactive sources of ^{228}Th were inserted next to the detectors as shown in Fig. 2.5(a), using a source insertion system during the weekly calibration runs [27, 46].

2.2.2 Signal Processing

As mentioned in Section 2.1, in case of energy deposition in the detectors, the electron-hole pairs will drift toward the electrodes. The charges on the p+ electrode are read out by a circuit with a preamplifier [69]. The signal was then digitized by Flash Analog to Digital Converter (FADC) [72]. An example of the resulting signal after the digitization is shown in Fig. 2.6.

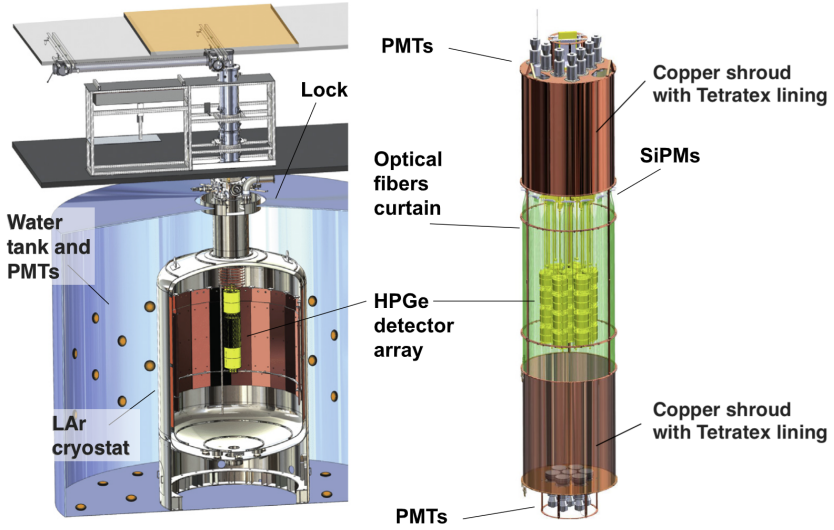

Figure 2.4: Schematic Drawings of the GERDA Phase II Setup. Figure adapted from [46].

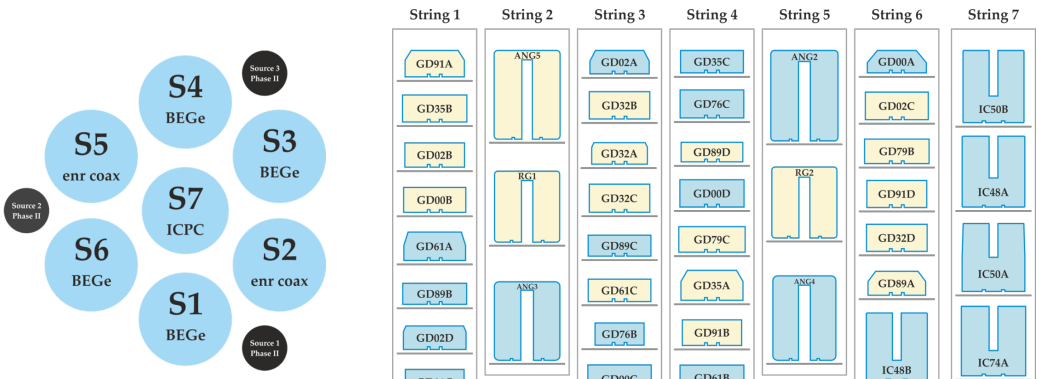

(a) Top view

(b) Detector Strings

Figure 2.5: (a) Top view of detector strings. The source next to the detector strings are for calibration purposes. In the diagram, "Enr coax" refers the Coax detector and "ICPC" refers to the IC detector. (b) Layout of the detectors of GERDA Phase II+. Internal figures from the GERDA collaboration [3].

In order to correctly calculate the energy of the signal waveform and filter out electronic noise, two signal shaping filters were applied independently to each waveform [69]. The first one is the pseudo-Gaussian filter that is robust and based on a moving average window algorithm. The signal is first differentiated, then the moving average window was applied 25 times. The height of the resulting signal, which is in quasi-Gaussian shape, is used as the energy estimator known as the "Gauss energy" [72]. With this filter, the high-frequency noise is removed.

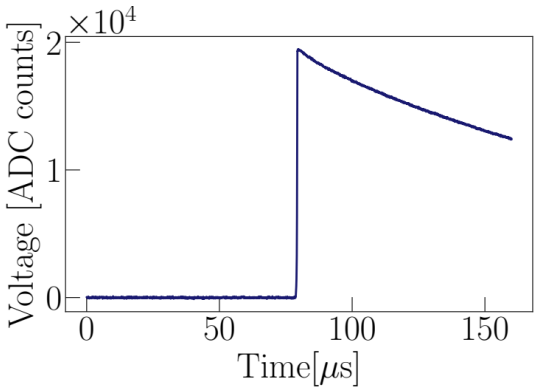

Figure 2.6: Typical signal waveform from a GERDA detector. Figure from [69].

The second filter is the Zero Area Cusp (ZAC) filter, which removes the low-frequency noise. A detailed description of the filter is given in [22]. Similarly, the height of the filtered signal is the energy estimator, called the "ZAC energy". The energy resolution when applying this filter is improved on average by ∼0.3 keV compared to the Gauss filter.

Since the parameters of the Gauss filter require no offline optimization, it is used for online monitoring [72]. In contrast, the parameters of the ZAC filters are optimized for each calibration and each detector for better performance, and requires additional offline processing [72]. The ZAC filters were used for the physics data analysis of GERDA.

2.3 The LEGEND Experiment

The LEGEND experiment is divided into two stages, the LEGEND-200 experiment and the LEGEND-1000 experiment. LEGEND-200 uses 200 kg enriched germanium detectors and will operate for about five years starting from 2021 [80]. The infrastructure of GERDA at LNGS is reused for LEGEND-200, providing the low background environment essential for LEGEND-200 [10]. The general method and operations are the same as those of GERDA [72]. However, the detector deployment system has been changed as a larger number of detectors will be loaded [80]. Also, the LAr veto system is redesigned to further improve the veto efficiency (Section 2.3.2).

Building upon LEGEND-200, LEGEND-1000 plans to use 1000 kg germanium and operate for 10 years starting from 2026-2027. The goal for LEGEND-1000 is to reach a discovery sensitivity at 10^{28} yr, as shown in Fig. 2.7. Hence, at least six times further background suppression is required [80].

The following sections are on LEGEND-200, including the experimental design and details of the LAr veto system.

2.3.1 Experimental Setup for LEGEND-200

The cryostat of LEGEND-200 is shown in Fig. 2.8(a). Apart from the detectors and the LAr veto system around the detectors, the description in Section 2.2.1 is applicable to

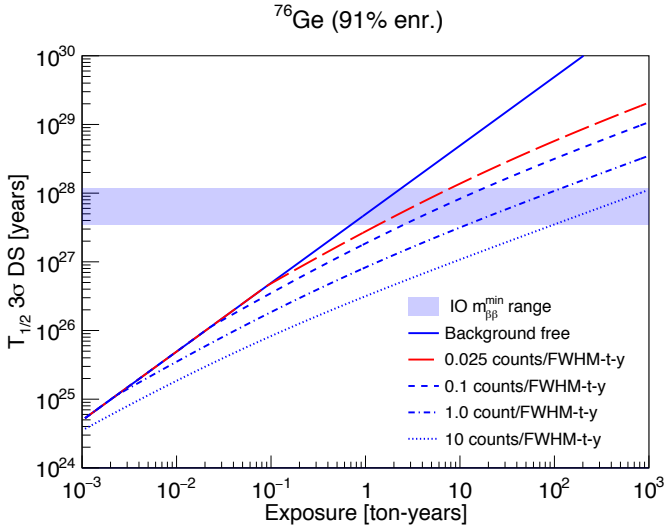

Figure 2.7: The half-life of $0\nu\beta\beta$ decay for 3σ (99.7% CL) discovery sensitivity as a function of exposure and background rate in detectors enriched in 88% ^{76}Ge. The red line indicates the background goal for LEGEND-1000. Figure from [11].

LEGEND-200. The detector strings will be arranged in the configuration as shown in Fig. 2.8(b,c). Regarding the detectors, most of them will be the newly produced IC detectors. In addition, the P-type Point Contact detectors from the MAJORANA experiment and the BEGe and IC detectors from GERDA will be reused.

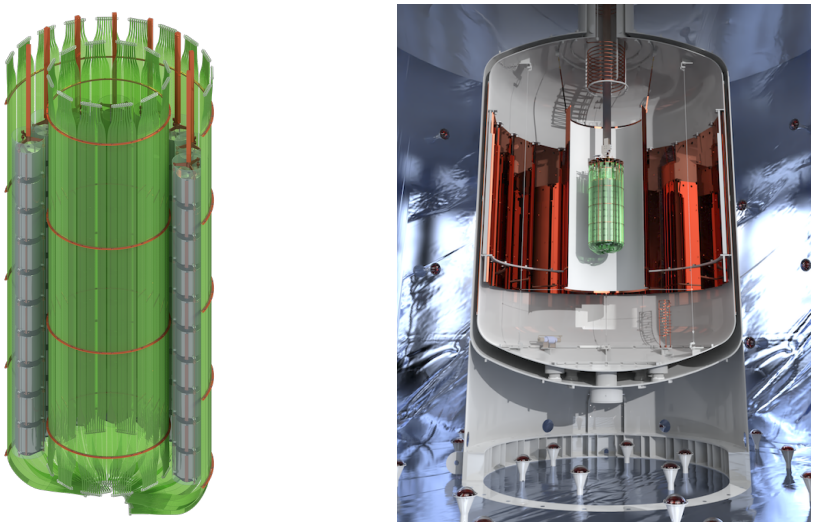

Figure 2.8: Experimental design of LEGEND-200. (Left) Detector strings with fiber curtain. (Right) LAr cryostat. Figure from [11].

2.3.2 Liquid Argon Veto System

The LAr veto system of GERDA Phase II has improved the background suppression performance compared to Phase I [23, 65, 24]. The veto efficiency of the LAr veto system increases if the light yield, which is the amount of light collected by the photo-detectors,

is higher [77, 54]. To reach the desired background level (Table. 2.1), the LEGEND collaboration redesigned the LAr veto system for the LEGEND-200 experiment such that it collects more scintillation light close to the detectors. On the other hand, as gammas far away from the detectors are shielded by LAr and do not deposit energy in the detectors, the new LAr veto system was designed to block their scintillation light in order to avoid unnecessary dead-time to the data acquisition (DAQ) of the veto system.

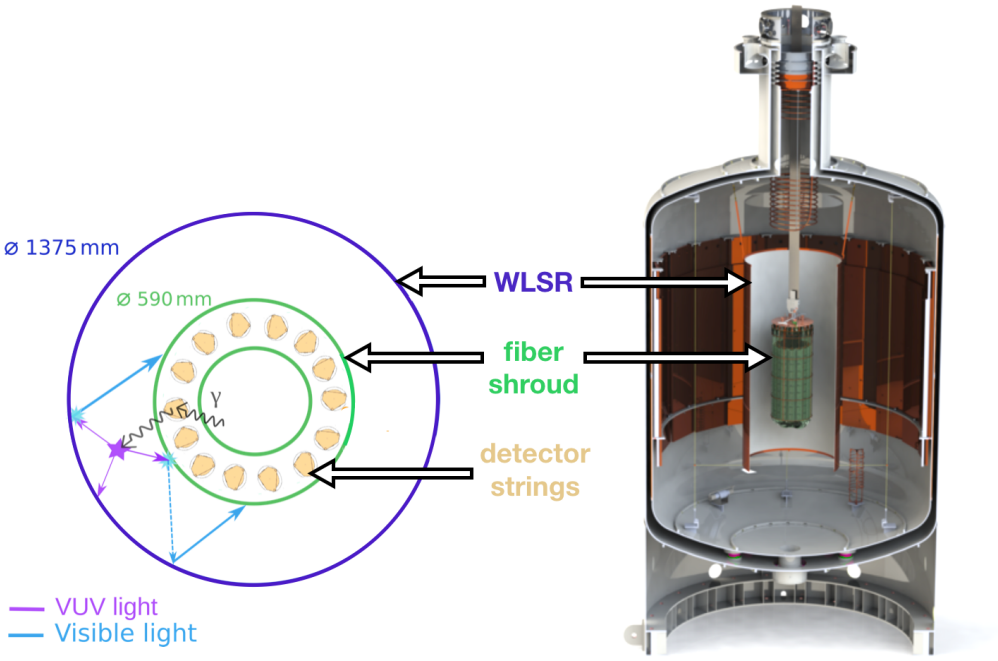

Figure 2.9: Schematic diagram of LAr Veto Mechanism. (Left) Credit: Gabriela R. Araujo. (Right) Figure from [7]. Details are described in the text.

Fig. 2.9 shows the design of the LAr veto system. As in GERDA, the fibers are evaporatively coated with TPB. The major change in the new design are on the wavelength-shifting reflector (WLSR). The WLSR consists of the TTX sheet coated with TPB and with copper at the back, as in the case of GERDA. Yet, compared to the WLSR in GERDA Phase II which was only at the top and bottom of the detector strings, the WLSR in LEGEND-200 forms the whole cylindrical shroud as shown in Fig. 2.9 (right). The copper at the back of WLSR not only provides mechanical support to the TTX sheet, but also blocks the LAr light outside the cylindrical volume from reaching the germanium detectors.

In addition, the new configuration will also increase the light collection efficiency. In case the scintillation happens between the outer fiber shroud and the WLSR in Fig. 2.9 (left), part of the light goes in the direction of the fibers and gets detected. However, since the light emission is isotropic, part of the light goes in the opposite direction. Additionally, photons reaching the fibers will be absorbed by the TPB on the surface and be re-emitted. Part of the re-emitted photons may not enter the optical fiber but, again, go away from the fiber. In the case of no WLSR, or for the configuration of GERDA, this light will not be detected. In LEGEND-200, the cylindrical WLSR will reflect these photons back to the fibers as shown in Fig. 2.9(left), hence increasing the light yield.

Besides, for the WLSR used in GERDA Phase II, the TPB was dip-coated onto TTX, i.e. the TTX was coated by pulling through a bath of solution with TPB dissolved [77]. In order to have a more uniform coating of TPB, the TPB in LEGEND-200 was evaporated onto TTX instead. Since the coating is fragile, in-situ evaporation ensure a better quality of the TPB coating. This was done in LEGEND-200, as described in Section 4.2.

Chapter 3

Low Energy Calibration for GERDA

For Gerda Phase II weekly calibration runs, the energy thresholds were always around 400 keV, except for a special calibration run with a 100 keV threshold. This part of the study analyzes the data from this special calibration run, probing the low energy region of GERDA detectors. In this chapter, high energy is referred to as the energy above 400 keV while low energy is between 100 keV and 400 keV.

In the previous calibration domain, the detector response scales linearly with the energy [27]. However, it was not confirmed whether the linearity would hold down to the low energy region. This poses unknown uncertainties in the low energy studies. Hence, in this study, the assumption of linearity of the detectors down to low energy region was checked, including those for the IC detectors.

In this chapter, the calibration sources and the calibration analysis are described in Section 3.2 and 3.3 respectively. The result of this study is presented in Section 3.4.

3.1 Motivation for Low Energy Searches

Apart from $0\nu\beta\beta$, the GERDA collaboration also conducts searches for other exotic physics with the GERDA data, for example, the bosonic Super Weakly Interacting Massive Particle (Super-WIMP) search [26]. The Super-WIMP is a dark matter candidate with mass range of keV to MeV. Since the exact mass, and thus energy, of a possible signal is not known, the search is done by scanning the full energy range of GERDA spectrum for unknown peaks [69].

Another possible study is the neutron disappearance: a bound neutron in a ^{76}Ge nucleus decays into invisible particles, such as neutrinos and dark matter particles, producing a ^{75}Ge nucleus. ^{75}Ge further decays into ^{75}As through β decay. With a certain probability, the ^{75}As is in an excited state which emits a 265 keV gamma upon de-excitation. By requiring the coincidence of this gamma and the β signal, the signal event can be selected with a supremely low background.

In addition, the dominant background in the low energy region is ^{39}Ar [23] as shown in Fig. 3.1. Even with the veto systems, this background cannot be removed. Hence, a better

background modelling is needed, and the low energy calibration is important in this case.

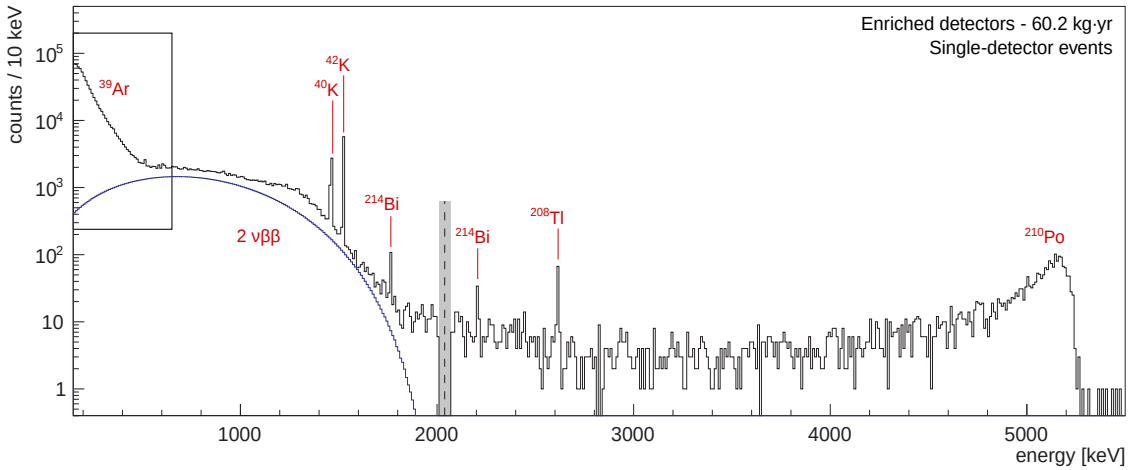

Figure 3.1: Figure extracted from [25] shows the summed energy spectrum collected in GERDA Phase II. The ^{39}Ar background is below 600 keV.

All these analyses mentioned above heavily rely on the correct energy scale of the detectors. Hence, it is indispensable to check for the linearity of the energy response of the detectors in the low energy region.

3.2 Calibration Sources

The sources used for the calibrations are ^{228}Th with activities around 10 kBq each [72]. The details of the source production are in [68]. The decay chain of this source is shown in Fig. 3.2(a). In the decay chain, gammas are emitted along with the α and β particles with a known spectrum shown in Fig. 3.2(b).

The gammas from the sources are detected by the germanium detectors with the configuration shown in Fig. 2.5(a). The detected signal was then filtered and reconstructed with the energy estimators introduced in Section 2.2.2. For each calibration run, there are three sets of data corresponding to each of the filter types applied: the FADC data which is unfiltered, the data with Gauss filter, and the data with ZAC filter. After the energy calibration, the energy in arbitrary units from these filters is converted into the energy in the physical units in keV.

3.3 Calibration and Analysis Procedure

Like other calibration runs, the energy calibration of this special calibration is carried out using a dedicated analysis package written in C++ using ROOT [40]. Modifications are made specifically for this low energy calibration run.

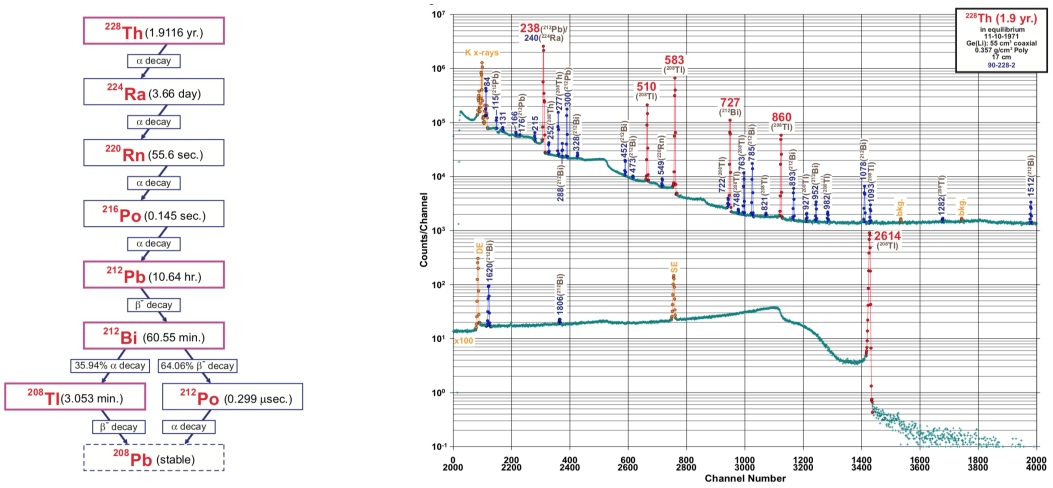

(a) Decay Chain

(b) Spectrum

Figure 3.2: (a) The decay chain and (b) the spectrum of ^{228}Th. Figures from [1].

The general approach of the project is as follows: for each detector, the calibration curves with only high energy peaks as in the normal calibrations are reproduced. These calibration curves are called the *high energy calibration curves*. Low energy peaks are identified but are not included in the calibration curves. Those that are not found by the package are fitted manually. The high energy calibration curves are then extrapolated down to the low energy region. Finally, the energy of the low energy peaks are converted to the physical unit using the high energy calibration curve and later compared with the literature values.

3.3.1 Previous Energy Calibration

The calibrations are performed for each detector and each filter. First, quality cuts are applied to the data to reject non-physical and pile-up events. The events surviving the cuts are binned into an uncalibrated energy spectrum with a bin width smaller than the resolution of all the detectors. Peaks are identified by the TSpectrum method in ROOT and shown as red triangles in Fig. 3.3. Then the threshold for peak finding is set to 5% of the height of the peak with the highest counts, which is usually the 2.6 MeV peak. The position of the peak in uncalibrated energy, U_0, with the height above this threshold is saved.

Since the peaks with energy above the 2.6 MeV peak have low intensity, the 2.6 MeV peak is regarded as the peak with the highest energy within the calibration. Thus, the peak with the highest energy in uncalibrated energy, U_{FEP}, is assigned to the 2.6 MeV peak. Assuming that the uncalibrated energy at zero corresponds to the zero in physical energy unit, a preliminary linear energy scale is obtained:

$$E_0(U_0) = \frac{2.6\ \text{MeV}}{U_{\text{FEP}}} \times U_0, \tag{3.1}$$

where E_0 is the energy in physical units, the subscript 0 is used to emphasize that the numbers are preliminary. A list of literature values of the gammas energy is defined in the analysis package, and some important values are shown in Table 3.1. Only the peaks with E_0 within 6 keV of any of the literature values are used in the calibration.

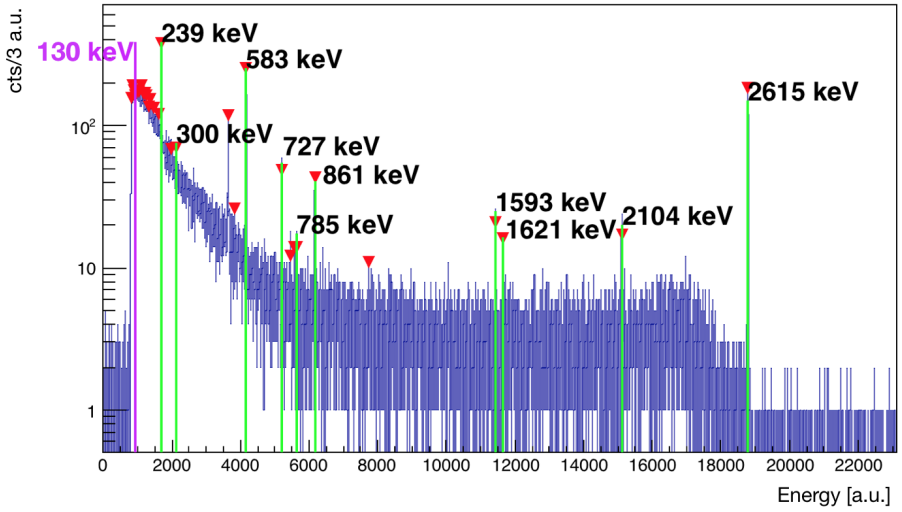

Figure 3.3: Energy spectrum of detector GD00B with ZAC filter. It represents a low energy calibration spectrum with a good peak identification. The red triangles indicate the peaks found by TSpectrum method. The green lines indicate the peaks that match the literature values. The magenta line is the estimated energy threshold of the detector.

Table 3.1: List of literature values of the gammas energies of ^{228}Th. The table is not exhaustive; only the frequently identified peaks are included. The corresponding functions in the fitting model are defined in Eq. (3.2-3.5). The meanings of FEP, SEP, and DEP are explained in Fig. 3.4. Values obtained from [1].

Peak type	Fit model	Energy [keV]	Branching ratio %
High statistics	$g + f_{lin}$	583.2	84.5
		727.3	6.6
		860.6	12.4
		2614.5 (FEP)	99.16
Low statistics	$g + h + f_{step} + f_{lin}$	785.4	1.1
		1078.6	0.6
		1620.5	1.5
SEP	$g + f_{step} + f_{lin}$	1592.5	Not Applicable
DEP		2103.5	Not Applicable

In Table 3.1, the meaning of full energy peak (FEP), single escape peak (SEP), and double escape peak (DEP) are explained by Fig. 3.4. With all the energy deposited into the detector, the energy recorded is the full energy of the gamma, giving rise to the FEP. With one escaped photon, the energy corresponding to an electron mass is lost, forming the SEP. With two photons escaped, the energy corresponding to two electron masses is lost, forming the DEP. SEP and DEP are treated differently as they have broader peaks, and are excluded for resolution estimation.

The candidate peaks are fitted with a predefined functions according to a categorization of the peak types, as tabulated in the first two columns in Table 3.1. The definition of each

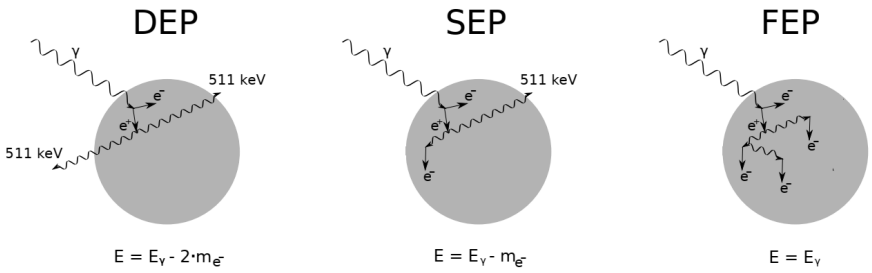

Figure 3.4: Event topology for the γ with energy 2.6 MeV. The big circle in each diagram indicates the boundary of a detector. Figure from [69].

functions are as follow:

$$g(E|N,\mu,\sigma) = \frac{n}{\sqrt{2\pi}\sigma}\exp -\frac{(E-\mu)^2}{2\sigma^2}, \tag{3.2}$$

$$f_{lin}(E|a,b) = a + b \times E, \tag{3.3}$$

$$f_{step}(E|\mu,\sigma,d) = \frac{d}{2}\mathrm{erfc}\left(\frac{E-\mu}{\sqrt{2}\sigma}\right), \tag{3.4}$$

$$h(E|\mu,\sigma,c,\beta) = \frac{c}{2\beta}\exp\left(\frac{E-\mu}{\beta}+\frac{\sigma^2}{2\beta^2}\right)\mathrm{erfc}\left(\frac{E-\mu}{\sqrt{2}\sigma}+\frac{\sigma}{\sqrt{2}\beta}\right), \tag{3.5}$$

where E is the uncalibrated energy as the independent variable; g is the Gaussian function with N, μ, σ being the amplitude, width, and mean respectively; f_{lin} is the linear function for the underlying background with a and b being the constant and slope respectively; f_{step} is the step function for modeling the Compton scattering with d being the height of the step function; h is for modeling the low energy tail due to the deficient charge collection, with c and β being the height and the slope of the tail respectively.

The mean of the Gaussian function is set as the new uncalibrated energy U, while the full width at half maximum (FWHM) of that is the resolution of that peak. Further cuts are applied based on the goodness of the fit such that only the peaks with good fitting would remain. Cuts include the resolution being greater than 1.5 keV and less than 11 keV; the amplitude of the peak being at least 10 counts and greater than 2.5 times the background level; the error of the FWHM of the Gaussian function being less than the FWHM itself. Since the FEP is always a strong peak with the highest energy, it is not passed to the cut, such that the calibration curve could always cover a wider energy range. In Fig. 3.3, the peaks that pass the fitting quality cut are indicated by green lines.

The calibration curve is determined by plotting U of the remaining peaks against their literature values and fitting the points with a linear function:

$$E_{\mathrm{keV}} = p_0 + p_1 U. \tag{3.6}$$

The error of the *calibrated energy* E_{keV} is given by the error of U, which is the standard error of the mean of the fitted peaks. An example calibration curve is shown in Fig. 3.5.

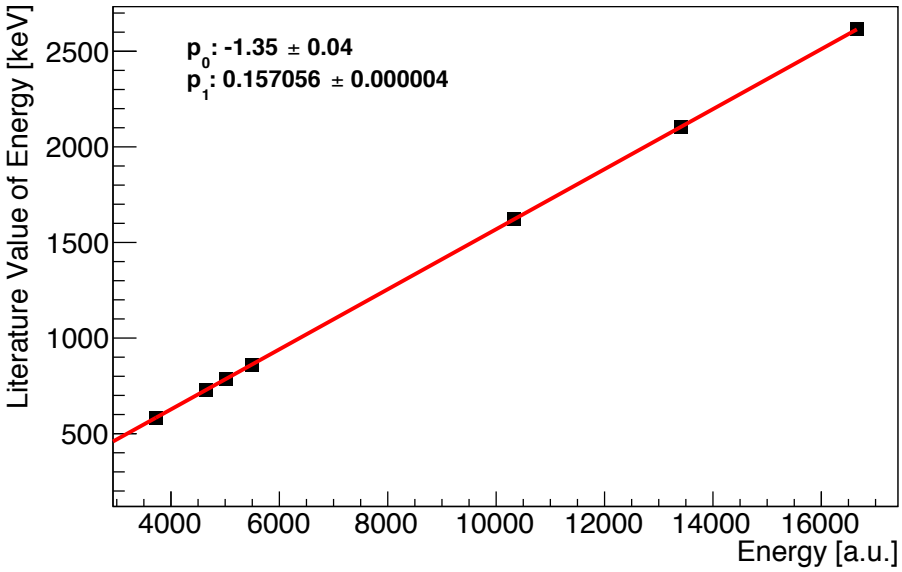

Figure 3.5: Calibration curve from detector RG1 from the FADC output.

The resolution curve, on the other hand, is obtained by plotting the FWHM against E_{keV} and fitting it with

$$\text{FWHM}_{\text{keV}} = 2.355\sqrt{p_2 + p_3 E_{\text{keV}}}, \tag{3.7}$$

while the FWHM_{keV} is given by

$$\text{FWHM}_{\text{keV}} = p_1 \text{FWHM}_{\text{a.u.}}. \tag{3.8}$$

An example resolution curve is shown in Fig. 3.6. More details of the calibration procedure can be found in [27].

3.3.2 Adding Low Energy Peaks

Since the calibration software does not include any low energy peaks in the range of 100 keV to 400 keV in Fig. 3.2, the information of some of these peaks is added, including the mean energy, the branching ratio, the fitting range, and the fitting functions. Not all the peaks in this range are added, because the peaks with a low branching ratio would have a comparable amplitude to the noise and thus might be falsely identified. Also, the matching between a found peak and the literature peak could be incorrect due to the cluster of candidates. In the end, only the peaks in Table 3.2 were added. The low energy peaks are named according to the table.

Note that the gamma from the nuclide ^{224}Ra has an energy of 240.986 keV and a branching ratio of 4.1% [1]. Although the branching ratio is not small, it is too close to the P238 in Table 3.2. It is, thus, also excluded from the list of low energy peaks. An example of P238 is shown in Fig. 3.7.

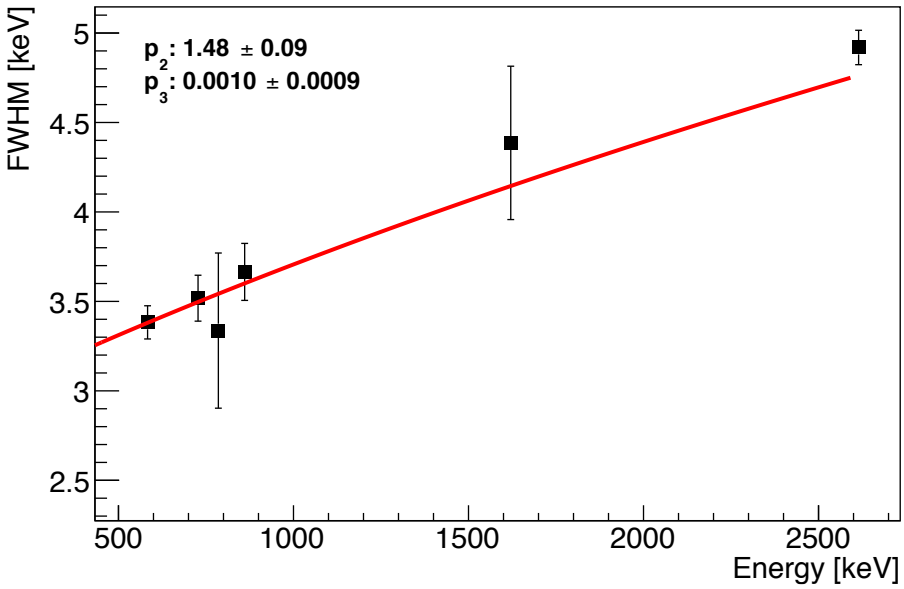

Figure 3.6: Resolution curve from detector RG1 from the FADC output.

Table 3.2: List of literature values for low energy peaks. Values obtained from [1].

Peak type	Fit model	Energy [keV]	Branching ratio %	Peak Name
High statistics	$g + f_{lin}$	238.632	43.3	P238
Low statistics	$g + h + f_{step} + f_{lin}$	277.358	6.31	P277
		300.087	3.28	P300

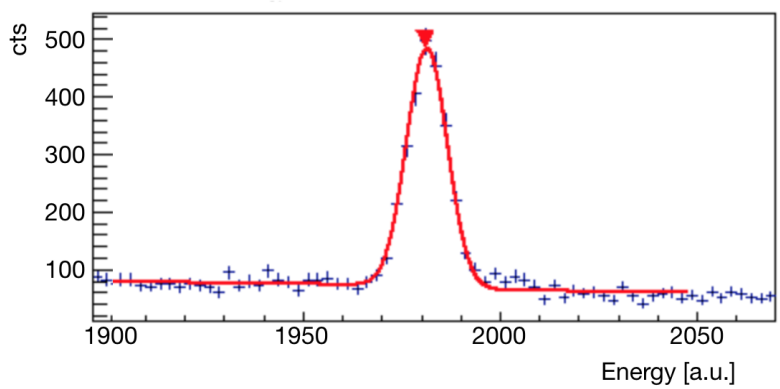

Figure 3.7: A typical spectrum of P238.

3.3.3 Modifications and Manual Fittings

Apart from adding the low energy peaks into the analysis package, the package is modified such that it only fits the high energy peaks for the calibration curve. Since the package is designed and optimized for the high energy calibrations by default, it is not efficient to process this special low energy calibration data set. In this case, certain settings in the package are modified so that it can find the lower energy peaks as well as reproduce the high energy calibration curve as in other calibration runs. Modifications include changing the peak-finding threshold, selection criteria, and the energy threshold estimation.

Some of the low energy peaks can be visually observed but not identified by the analysis package. They are fitted and selected manually. The details of the modifications and manual fittings are in Appendix A.

3.4 Results

The results presented in this section are based on the processed physics data using the ZAC filter motivated in Section 2.2.2.

3.4.1 Calibration Curve

In the case where the low energy peaks are inline with the high energy peaks, the calibrated energy from Eq. 3.6 should have values close to the literature value. The greater the deviation, the less linear the detector is across the full energy domain. In order to examine the linearity of the detectors, the literature values of the low energy peaks are subtracted by the calibrated energy using the extrapolated high energy calibration curve.

The discrepancies across all the detectors are shown in Fig. 3.8. The error is propagated from the error of the literature value of the peak from [1] and the error of fitting error of the Gaussian peaks as shown in below

$$\delta D^2 = \delta(\text{L.V.})^2 + p_1^2 \delta U^2, \tag{3.9}$$

where D is the discrepancy, L.V. is the literature value, and p_1 and U are the same as in Eq. 3.6. The error of the parameter p_1 is negligible in this equation.

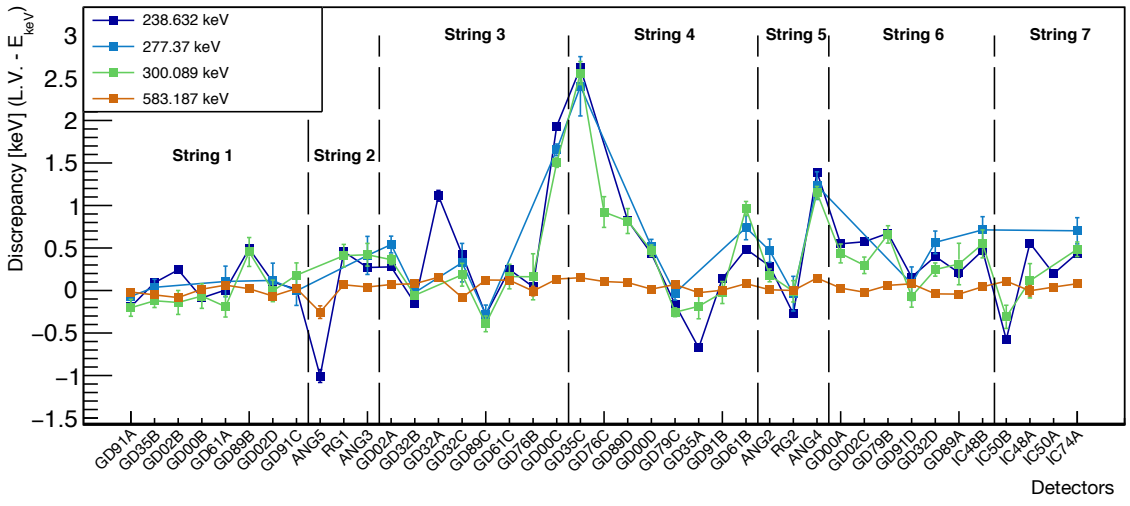

Figure 3.8: Discrepancy of the calibration curve for each detector across the three low energy peaks with the ZAC filter. A high energy peak at 583 keV is also shown for comparison. The discrepancy is the difference between the literature value and the calibrated energy.

In Fig. 3.8, the most noticeable feature is the systematic higher discrepancy of detector GD00C and GD35C on String 3 and String 4. The discrepancies of the three low energy

peaks being greater than zero implies that the correct calibration curve in the low energy region should be gentler than the high energy calibration curve as shown in Fig. 3.9. The greatest discrepancies are from GD35C. The average value of the three low energy peaks is 2.5 keV, which is $\sim$1% of the peak energy. For all the detectors, the discrepancy is around or smaller than 1%. The result of other filters is similar.

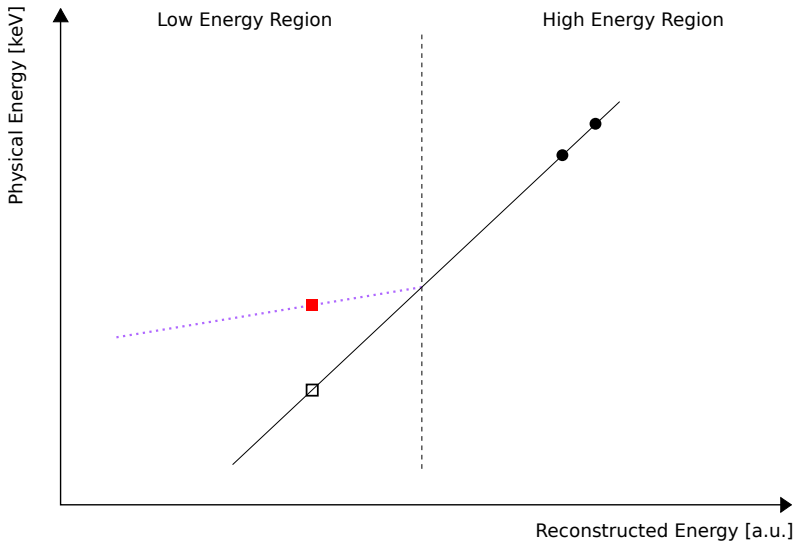

Figure 3.9: Illustration of a positive discrepancy. The solid line is the calibration curve using only high energy peaks. The solid circle represents the high energy peaks. The solid red square represents a low energy peak with the physical energy being its literature value. The hollow square also represents the low energy peak but with the energy being calibrated using the extrapolated high energy calibration curve. The discrepancy in Fig. 3.8 is the physical energy of the solid square subtracted by that of the hollow square. The dotted purple line represents a correct calibration curve in low energy region, which has the slope that is gentler than the high energy calibration curve.

The discrepancy of the calibration curve of all detectors against the full energy domain is shown in Fig. 3.10. A 1σ band around the mean discrepancy value of BEGe detectors is drawn on the same plot for reference. Although IC detectors show more uniform values across detectors compare to BEGe, the number of IC detectors is too few for such conclusion. Besides, the one standard deviation band of BEGe detectors shows that the spread across BEGe detectors is not significantly wider than those of the IC detectors and Coax detectors.

3.4.2 Resolution Curve

The resolution discrepancy for each detector is shown in Fig. 3.11. The discrepancy in this case is defined as the value predicted by the resolution curve in Eq. 3.7 subtracted by the measured FWHM of each peak. In Fig. 3.11(a), detector ANG5, GD35C and RG2 have relatively higher FWHM. However, in both Fig. 3.11(a) and (b), no significant systematic

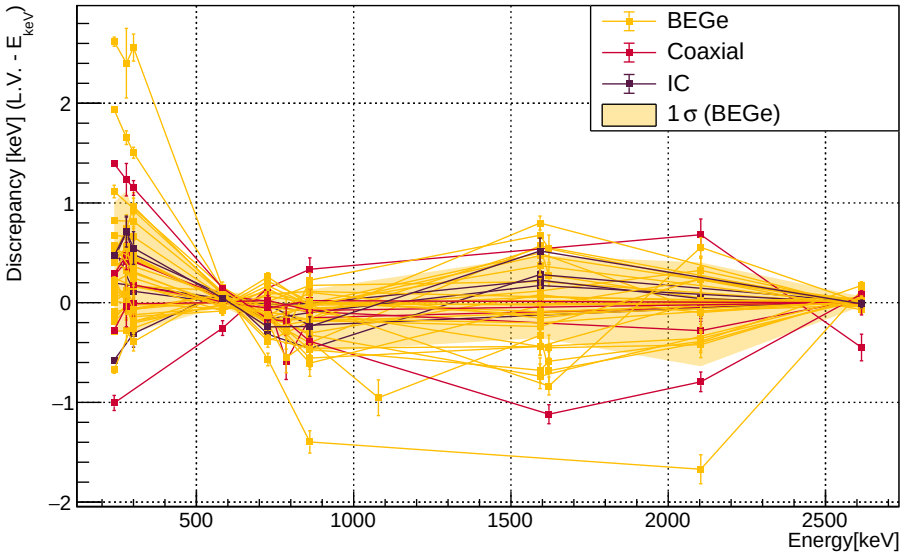

Figure 3.10: Discrepancy of the calibration curve of all detectors against the peak energies for the full energy domain for the ZAC filter. The detectors are colored according to their corresponding types. The discrepancies of low energy peaks are the same as in Fig. 3.8. For BEGe detectors, a band of one standard deviation around the mean value is also shown in the figure for reference. The limited number of peaks for the other two detector types is not ideal to calculate the standard deviation.

deviation between the low energy peaks and high energy peaks is shown, unlike the case for the calibration curve.

Fig. 3.12 shows the FWHM against the peak energies across different detector type. 1-σ band around the mean FWHM value of BEGe detectors is drawn for reference. From the figure, it can be observed that three out of the six Coax detectors have their FWHM outside the one σ reference band of BEGe. On the contrary, the FWHM of the five IC detectors all falls within the one sigma band.

3.4.3 Conclusion

The low energy peaks of detector GD00C and GD35C show systematically positive discrepancies between the literature values and the calibrated energies. The positive discrepancies imply that their actual low energy calibration curve should have a lower slope than their high energy calibration curve. However, the discrepancy is $\lesssim$1% for all the detectors. Hence, one could still assume the linearity across the high energy and the low energy range, and use the discrepancy as a measure of the uncertainty.

Regarding the resolution of detectors, there is no systematic deviation of the FWHM away from the resolution curve as in the calibration curve. However, three detectors have relatively larger discrepancies: ANG5, GD35C and RG2.

With the limited number of detectors, IC detectors are observed to have, in general, better

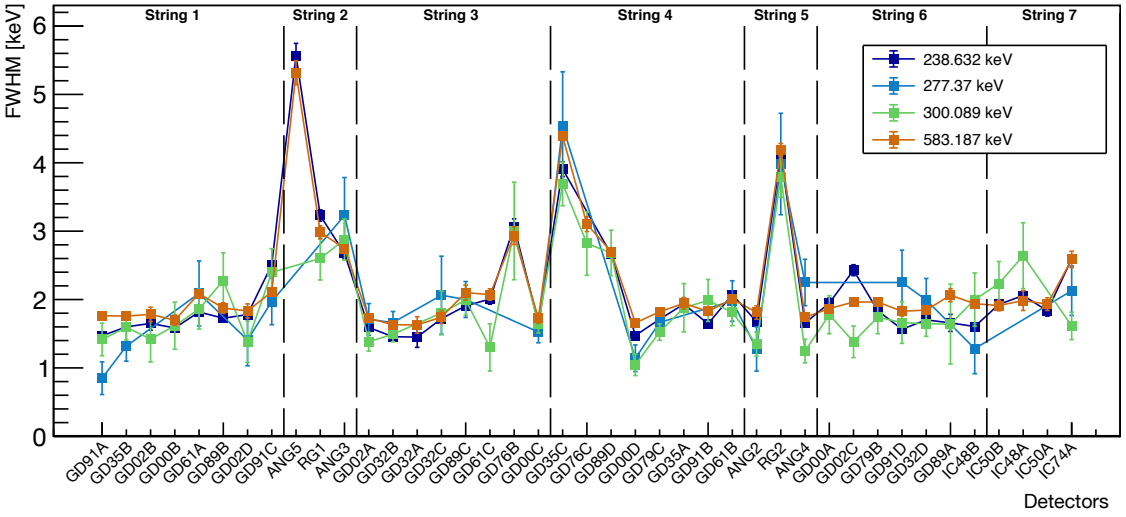

(a) FWHM of all the detectors

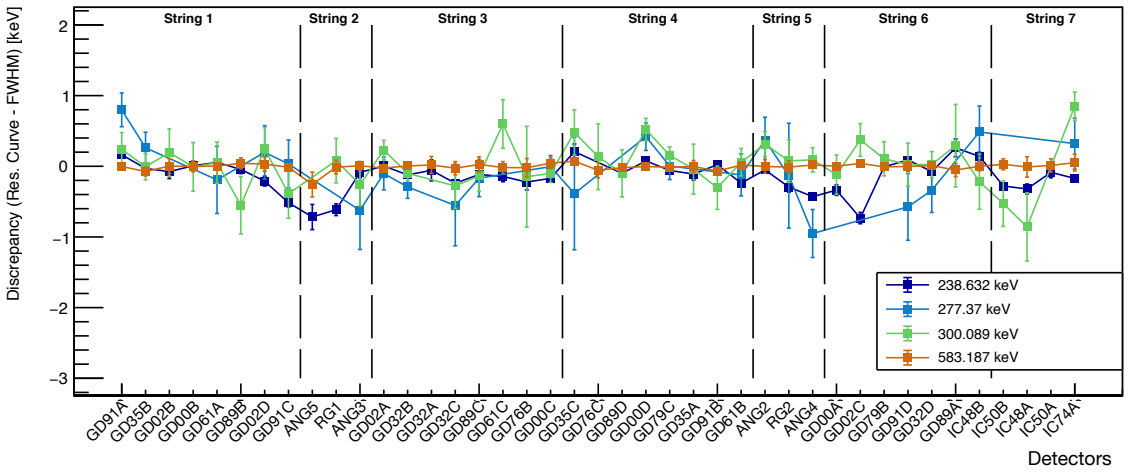

(b) Discrepancy of all the detectors

Figure 3.11: The resolution of low energy peaks for all detectors from the ZAC filter data. The y-axis is (a) the measured FWHM itself and (b) the discrepancy between the FWHM based on the resolution curve and the measured FWHM.

energy resolution and more uniform performance across the low energy and high energy regions compared to the other two detector types.

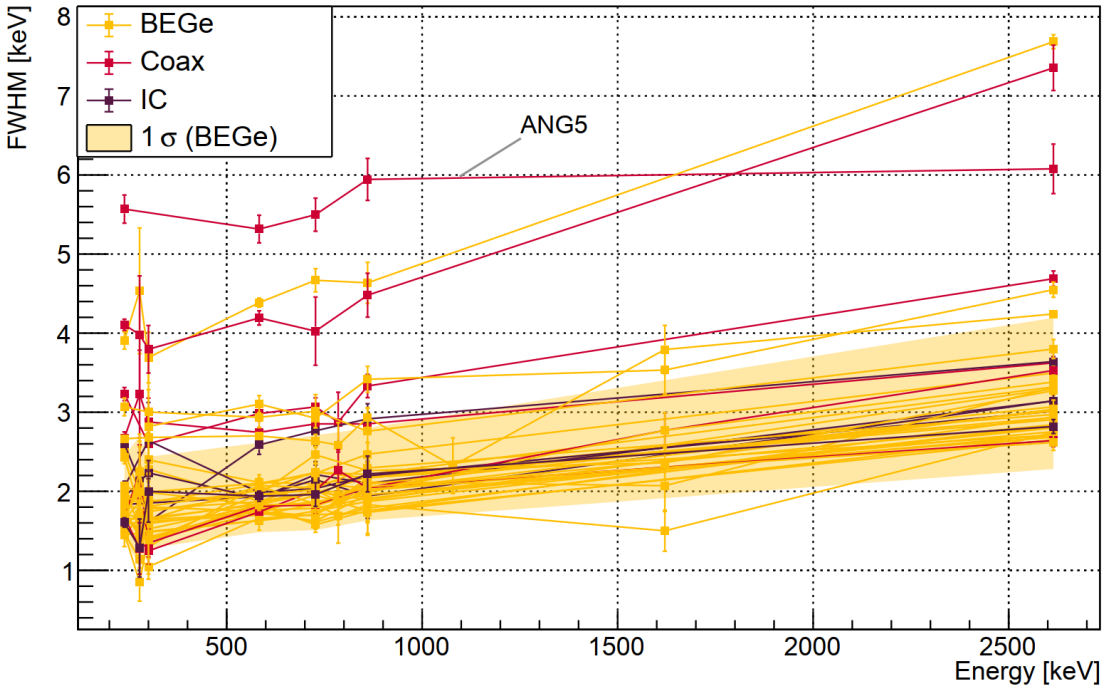

Figure 3.12: Similar to Fig. 3.10 but the y-axis is only the FWHM of each peak.

Chapter 4

Characterization of Wavelength-shifters and Reflectors in Liquid Argon for LEGEND-200

LAr is a popular choice of scintillators for dark matter experiments, for example, in WArP [60], ArDM [41], DEAP-3600 [17], and DarkSide-50 [19]. It is also popular among neutrino experiments, such as DUNE [58], GERDA [24], and LEGEND [80]. In particular, the LEGEND-200 experiment uses LAr, with its boiling point at 87.28 ± 0.02 K at atmospheric pressure[4], for cooling the detectors, as well as for shielding and vetoing backgrounds, as described in Section 2.3.2.

The LAr scintillation light spectrum peaks at 126.8 nm with FWHM of 7.8 nm as shown in Fig. 4.3 [53]. This wavelength, which is within the Vacuum Ultra-violet (VUV) range, is lower than the detectable wavelength for commercially available PMTs and SiPMs. This motivates the detailed studies of wavelength shifting materials in the LAr medium [12, 63], which can shift the VUV scintillation light of LAr to a longer wavelength in the range of visible light.

In addition, in the case of a LAr veto system, an increase in light yield, which is the amount of light detected by photo-detector(s), of the system increases the veto efficiency [77, 54]. Hence, the efficiency of light yield enhancement caused by the wavelength-shifting and reflective materials in the LAr medium is an important factor when selecting a better material for the LAr veto system. Also, the optical properties of the materials are important for simulating the LAr veto system. Therefore, the optical characterization of wavelength-shifting and reflective materials is well motivated.

In this chapter, the study determining the light yield enhancement due to two wavelength shifting and reflective samples is presented. One of them is the combination of Polyethylene Naphthalate (PEN) and TTX, and the other is the witness sample of the WLSR from LEGEND-200, which is a small sample that was prepared together with the LEGEND-200 WLSR (Section 2.3.2). The properties of LAr scintillation light are first introduced as background information (Section 4.1). The details of the samples are described in Section 4.2. The experimental setup (Section 4.3), the experimental procedures (Section 4.4), and

the analysis and results (Section 4.5) are described in consecutive sections.

4.1 Liquid Argon Scintillation Process

The mechanism of the scintillation process of LAr is illustrated in Fig. 4.1 and described in detail by [76]. First, an ionizer either excites the argon atom to an excited state, Ar^*, or ionizes the atom to argon ion, Ar^+. Ar^* forms a singlet or a triplet state excimer, also known as the excited molecule Ar_2^*. It decays back into argon atoms and emits VUV scintillation photons. On the other hand, Ar^+ forms an ionized molecule, Ar_2^+, with another argon atom. It later recombines with an electron and also becomes an excimer, which decays and emits VUV light.

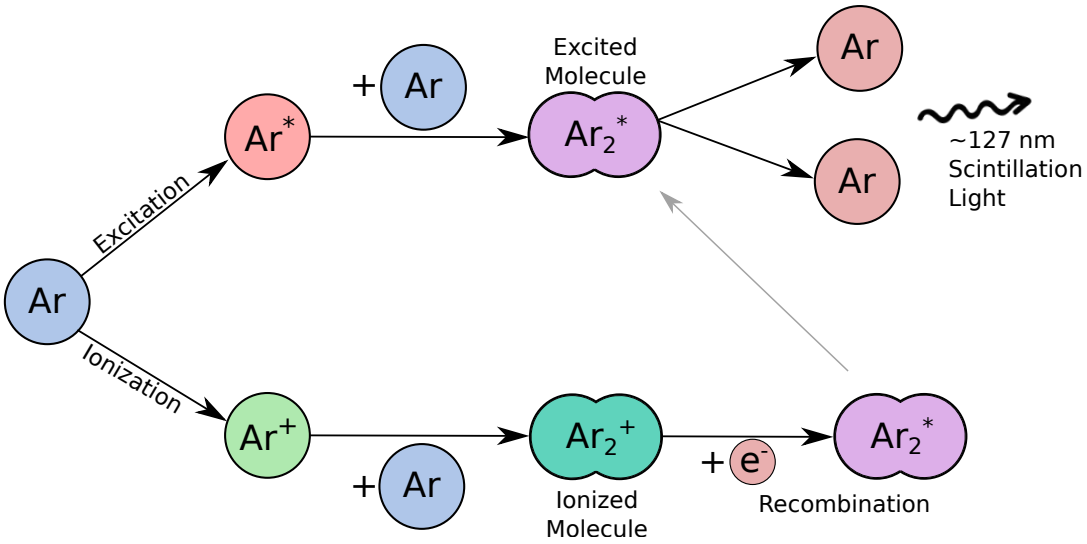

Figure 4.1: The scintillation process of Ar. Figure adopted from [31].

Fig. 4.21 shows the waveforms of LAr scintillation light being stacked together without weighting. The VUV scintillation light is, as mentioned, composed of the fast component due to the singlet excimer state, and the slow component due to the triplet excimer state. The intrinsic lifetimes of the two components are ∼7 ns and ∼1300 ns respectively [17, 56, 53]. However, it was found that an increase in impurities in LAr decreases both the amplitude and lifetime for both the singlet and triplet components [13, 14], resulting in a decrease in the integral of the signal, i.e. the light yield. As shown in Fig. 10 and 11 of [14], the triplet component is more sensitive to a change in purity, thus, the consistency of LAr purity across measurements are crucial to reduce the systematic error on light yield. The triplet lifetime is usually used to indicate the change in purity level in LAr in different experiments [77, 17], including the one described in this chapter. Because of the variable amount of impurities, the measured triplet lifetime of LAr across different

experiments have a relatively large discrepancy, ranging from 1100 to 1600 ns [55, 17, 56].

On the other hand, the ratio between the fast and slow components is different for different ionizing particle types [55, 64, 61]. Specifically, the ionization due to heavier ionizers, for example, alpha particles and fission fragments, has a larger ratio compare to the lighter ionizers, such as beta particles and gammas. For LAr, the singlet component of nuclear recoils (NR) usually consists of ∼60-70% of the total light yield, while that for electronic recoils (ER) is ∼30% [18]. Similar values were also observed in this experiment, where alpha particles are generally inducing the NR signal and the background with betas and gammas inducing the ER signal. This property was used to distinguish the signal and the background in this experiment as described in Section 4.5.3.

4.2 Wavelength-shifting and Reflective Samples

As mentioned, PEN with TTX and WLSR were the two wavelength-shifting and reflective samples being tested in this experiment. This section documents the motivations of characterizing them as well as their preparations.

(a) WLSR **(b)** PEN alone

Figure 4.2: (a) WLSR witness sample from the LEGEND-200 in-situ TPB deposition at LNGS. (b) PEN sample without reflector and without sanding (milky plastic in the photo).

As mentioned in Section 2.3.2, WLSR is made from TTX evaporatively coated with TPB. It is used as the wavelength-shifting and reflective material in LEGEND-200 in order to enhance the light yield for the veto system. However, its optical properties, such as the reflectance and the quantum efficiency[1] (QE) in a LAr medium, are not well known. They are essential for future simulations of the LAr veto system of LEGEND-200.

PEN, a wavelength-shifting plastic, is a possible alternative to TPB since it is more easily manipulated and scaled up. Without the need of a deposition stage, as required by TPB, it has the potential to save time and avoid complications especially in larger-scale LAr experiments [63, 62]. For this reason, PEN was also tested in this experiment. The emission spectra of TPB at 87 K [42] and PEN at 93 K [66] are shown in Fig. 4.3.

[1] The ratio between the number of re-emitted photons to that of absorbed photons.

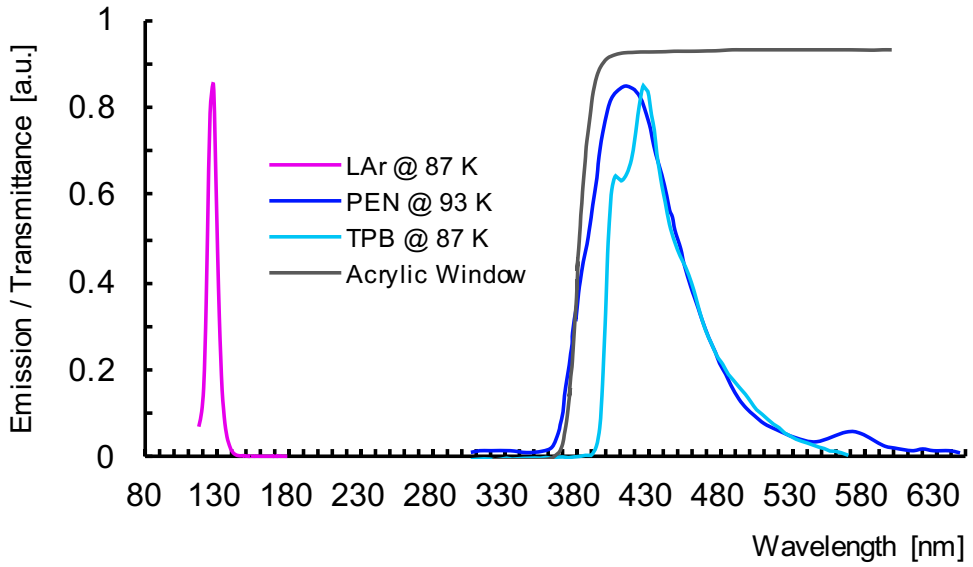

Figure 4.3: Emission spectra of LAr at 87 K [53], PEN at 93 K [66] and TPB at 87 K [42], normalized to the same amplitude. The plot also shows the transmission spectrum of the acrylic disk, as introduced in Section 4.3.1. The transmission spectrum was measured using a spectrophotometer in the Chemistry Department at the University of Zurich.

The review from Kuźniak and Szelc [62] provides some comparisons between TPB, PEN, and other materials as a wavelength-shifter. While the QE is one of the intrinsic quantities to determine the effectiveness of a wavelength-shifter, the light yield measured by the PMT also depends on the experimental setup, including the number of scatterings with the wavelength-shifting sample before reaching the PMT, refraction across optical boundaries, reflectance of TTX at LAr temperature, among others. Hence, given the light yield enhancement measured from the experiment, a Monte Carlo simulation of the setup is necessary in order to calculate the absolute reflectance and the QE of the samples. This Monte Carlo was outside the scope of this work.

Preparation of the Samples

The LEGEND collaborators, including the group from the University of Zurich, prepared the WLSR for the LAr veto system using in-situ evaporation in LEGEND-200. Before the evaporation, the TTX was attached to the cylindrical copper for mechanical support. The witness sample for this experiment was attached at the bottom of the cylinder. Then, the TTX on the cylindrical copper was evaporated with TPB in a vacuum of the order 10^{-5} mBar. The thickness of the coating is $\sim$600 nm, which was measured by the LEGEND collaborators at the Technical University of Munich.

The PEN sheet (Fig. 4.2(b)) has a thickness of 0.125 mm and was ordered from Goodfellow. By shining a VUV light source to the PEN sample, it was observed with unaided eyes that the edges of the plastic yield more light than the surfaces, implying that the light emitted by PEN experienced total internal reflection inside the raw PEN sheet. To avoid the attenuation caused by total internal reflection, the sample was sanded on both sides

with grade P240 sandpaper in random directions (Fig. 4.4(a)). This created random angles on the surface, increasing the chance for the photons to escape from multiple total internal reflections. After sanding the PEN sheet and cleaning it in an ultrasonic bath with propanol, the TTX was simply pressed against the PEN, as shown in Fig. 4.4(b). With Kapton tapes taped on the borders, no adhesives or glue were used to couple the surfaces.

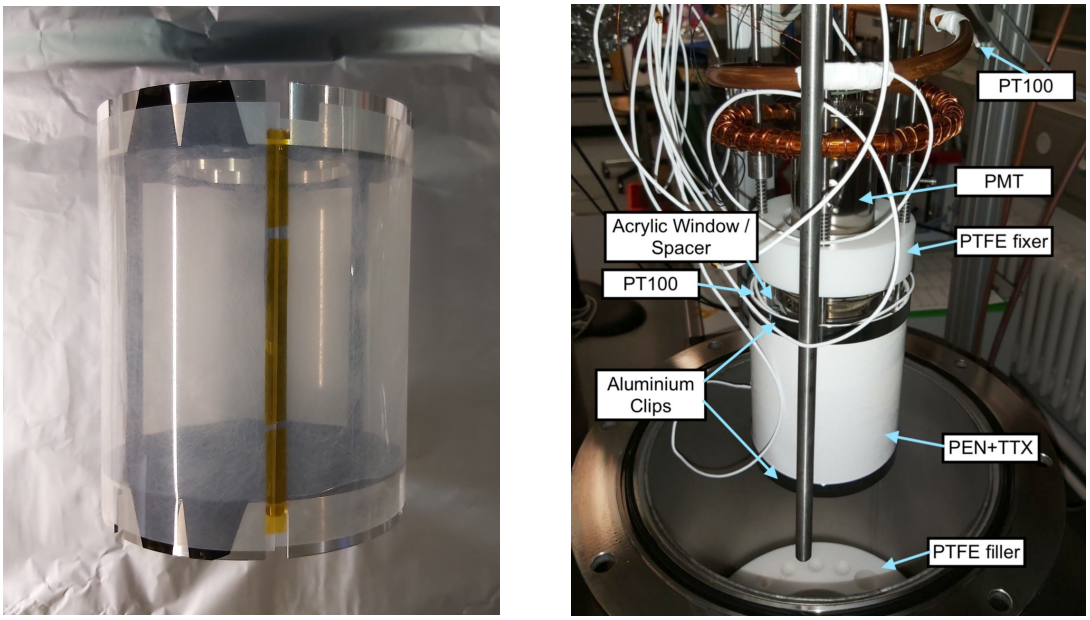

(a) Sanded PEN **(b)** PEN with TTX

Figure 4.4: (a) PEN alone on the sample holder, as described in 4.3.1. The Kapton tape is behind a supporting pillar of the sample and source holder, such as to prevent it from affecting the light yield. More details in Section 4.3.1. (b) PEN with TTX installed in the experimental setup (Section 4.3). Most of the relevant components of the setup are labeled.

4.3 Experimental Setup

The Liquid Argon Setup (LArS) at the University of Zurich was used for this experiment. The illustration and the photo of the setup are shown in Fig. 4.5 and Fig. 4.4(b) respectively. The major components include a cryostat, a cooling system, inlets and outlets for gases and a vacuum pump, electric feed-throughs, and sensors. Photodetectors and samples can be mounted inside the cryostat, which is filled with liquid or gas, for various tests.

The setup includes a levelmeter, two PT100 temperature sensors and a pressure gauge. The levelmeter is used to monitor the level of LAr filled inside the cryostat. The temperature sensors are used for cooling and stabilizing the system at a set temperature. The pressure reading is useful for monitoring the system during the filling and data-taking phase, as well as provide information when choosing a set temperature. The calibration of the sensors and stability monitoring is in Section 4.4.

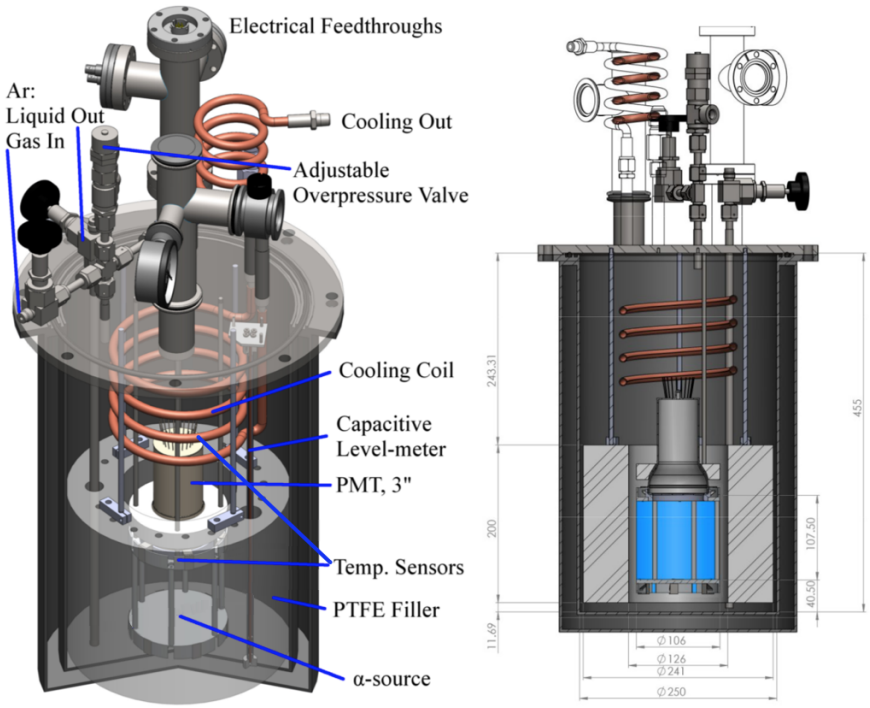

Figure 4.5: 3D (left) and 2D (right) drawings of Liquid Argon Setup from Fig. 3.8 in [77].

The signal from the photodetector is sent to an external DAQ system through the feed-through via a coaxial cable. In the case of a PMT, the high voltage is also supplied externally through the feed-through. A large Polytetrafluoroethylene (PTFE) filler block sitting at the bottom of the cryostat occupies the volume inside the cryostat, in order to decrease the amount of LAr needed and speeds up the filling.

Cooling System

At atmospheric pressure, argon has a boiling point of 87.28 ± 0.02 K and a melting point of 83.8 ± 0.3 K [4]. Since the melting point is $\sim$3.5 K lower than the boiling point in the pressure range of interest to this experiment, a well-controlled cooling system is important. If the cooling system is not reliable and the temperature dropped too much or too fast, argon would start to solidify inside the setup, lowering the condensation power of turning gaseous argon (GAr) to LAr.

The cooling system in LArS controls the temperature inside the setup to the desired set-point temperature. Specifically, the cooling system liquefies the GAr into LAr and then stabilized the temperature of the system at the condensation point of argon for this experiment. Liquid nitrogen (LN_2) was used to remove heat from the setup through the cooling pipeline. The copper pipeline enters the cryostat and coils around the upper part of the cryostat to increase surface area and thus the cooling power. After exiting the cryostat, the length of the pipeline is maximized such that the remaining LN_2 can be fully converted to gaseous N_2. The flow rate of the gaseous N_2 at the outlet valve was controlled by the temperature controller, Cryo-con 32, during the experiment. The faster the flow rate, the

higher the cooling power, and vice versa. Inside the cryostat, there are two PT100, one is on the pipeline of LN_2, one is next to the PMT window. Depending on the stage of cooling, as described in Section 4.4.2, one of the PT100 was chosen to provide feedback to the temperature controller, with which the cooling system regulated the flow rate accordingly. For example, if the setpoint temperature is lower than the reading of the PT100, the flow rate increases to increase the cooling power.

Other modes of temperature control can also be chosen, for example, using the pressure instead of temperature as the feedback for the temperature controller, or controlling the flow rate using a needle valve. However, these methods were not employed in this experiment.

4.3.1 PMT Cell

Apart from the above permanent components of LArS that were designed by previous students, additional parts, namely the *PMT cell*, were added to the setup specifically for this experiment in order to detect the absolute light yield enhancement by the wavelength-shifting and reflective samples. Fig 4.6 shows the schematic diagrams of the PMT cell. It includes a PMT, acrylic disk or spacer, sample and source holder, the testing samples, and a source for scintillation light in LAr.

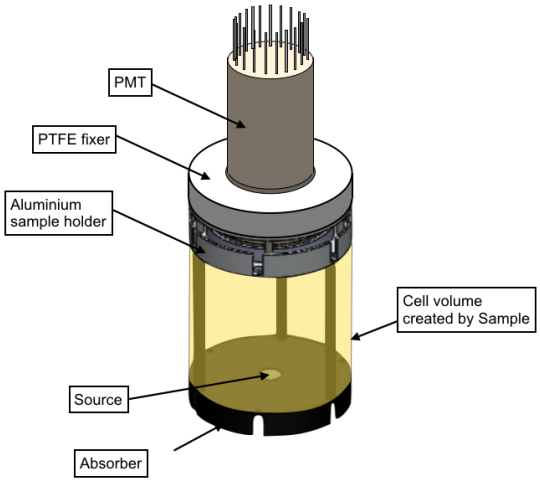

(a) PMT cell

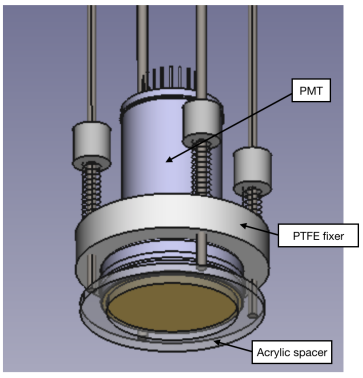

(b) Acrylic spacer under the PMT

Figure 4.6: Illustration of the PMT cell. (a) Drawing of the PMT cell. The yellow cylinder represents the position of the sample. The sample, the sample holder, and the PMT formed the cell volume. All the aluminum parts visible to the PMT were covered by the absorber. The acrylic disk or spacer, which is between the PMT and the sample holder, is not visible from the diagram, hence not labeled. (b) Drawing of the acrylic spacer underneath the PMT.

Source

The radioactive source in this experiment, ^{241}Am, is the same source used in [36]. The source, with the activity of 30 Bq, was made at PSI and was not encapsulated. However, since the source is in a disk shape and placed on a source holder such that one side of the source was covered, it is expected that around half of the alphas were depositing energy in the PMT cell volume.

The emission spectrum of the alpha particles is shown in Fig. 4.7, with mostly the alphas of the energy 5.486 MeV [36]. The alpha particles interact with the argon nucleus and induce NR scintillation light in LAr. Low energy gammas are also emitted along with the alpha particles, inducing ER scintillation light.

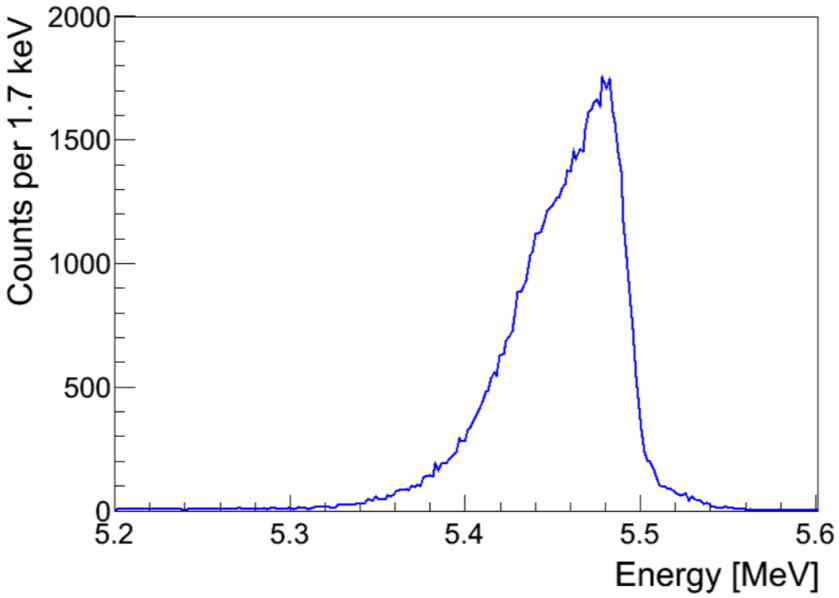

Figure 4.7: Spectrum of the source ^{241}Am. Figure from [77].

PMT and Acrylic Disk

As mentioned at the beginning of the chapter and Fig. 4.3, the wavelength of LAr scintillation light is ∼127 nm. While commercial PMTs could not see the light with this wavelength, the PMT used in this experiment could. It is a special 3-inch PMT, R11065-MOD, by Hamamatsu Photonics with the MgF_2 window which is transparent to the VUV scintillation light and the shifted visible light. Fig. 4.8 shows part of the QE[2] curve of this PMT. At ∼127 nm, the QE of the PMT is at 22.2%. On the other hand, the QE at 420 nm is 27.38% given by the datasheet of the PMT. As a result, this PMT can see both the scintillation light and the shifted light with a reasonable QE. The more in-depth characterization of the PMT is provided in Appendix B.

[2]The ratio between the number of photoelectrons (PEs) emitted from the photocathode to the number of incident photons [2].

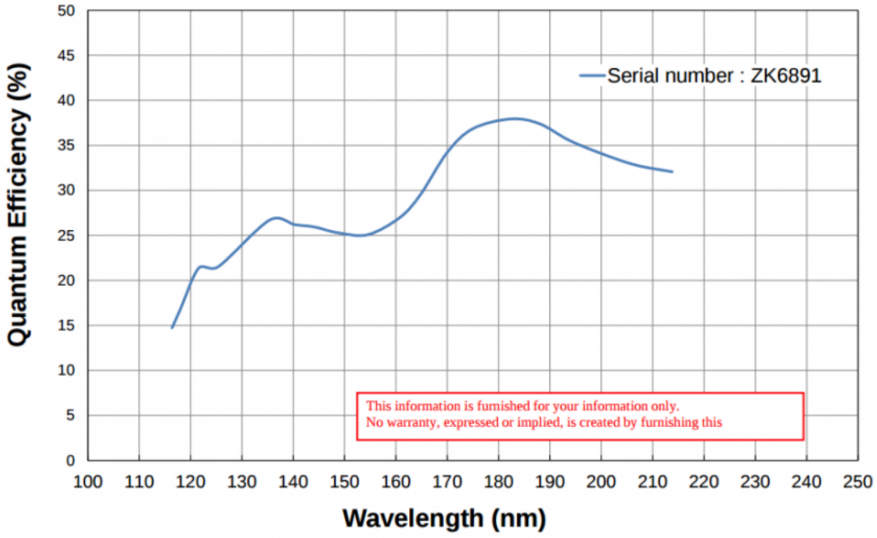

Figure 4.8: QE curve of R11065-MOD. Figure provided by Hamamatsu.

The PMT base used in this experiment is shown in Fig. 4.9. Most parts of the circuit are potential dividers that provide potentials to the electrodes of the PMT. The potential difference of the electrodes accelerates the PEs, resulting in a cascade of electrons and, thus, an amplification effect. The arrangement of the circuit was made such that the HV pin is farthest away from the ground pin to prevent a short circuit when the PMT is turned on at atmospheric pressure.

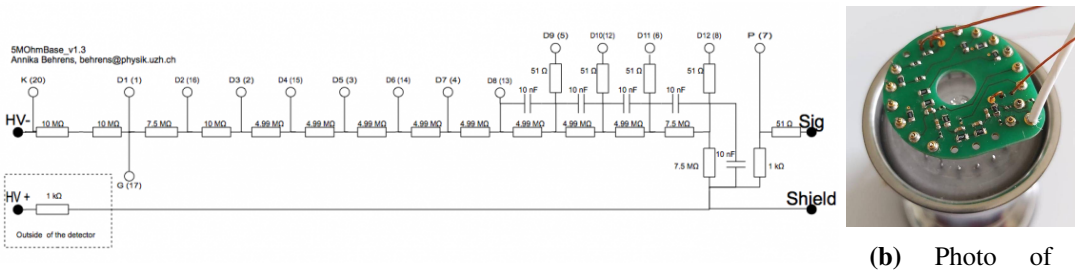

(a) Circuit diagram

(b) Photo of PMT base

Figure 4.9: (a) Circuit diagram of the PMT base shown in (b). (b) PMT base mounted on the PMT.

For the wavelength shifting and reflective sample, WLSR and PEN with TTX, two kinds of measurements were made, one with an acrylic disk, and the other with an acrylic spacer. As illustrated in Fig. 4.6(b), the PMT was fixed in place by four aluminum pillars and the PTFE fixer at the top of the PMT, while the acrylic disk or spacer was placed in front of the PMT window.

The 5 mm thick acrylic disk is opaque to the VUV light, hence it blocked the VUV scintillation light from reaching the PMT, transmitting only the shifted light. The transmittance of the disk is shown in Fig. 4.3. The acrylic spacer has the same thickness as the acrylic disk, and it was placed at the same position as the disk, as shown in Fig. 4.6(b). In this configuration, the light yield of the PMT included both the VUV and the visible light.

The same thickness of the disk and the spacer provides a fair comparison between the measurement, as the vertical distance between the source and the PMT was the same. In principle, the comparison served as a cross-check for the amount of shifted light. The interpretation of the comparison is discussed in detail in Section 4.5.

Sample and Source Holder

The sample and source holder was made of aluminum. The holder (Fig. 4.4(a)) consists of the top ring, the bottom plate, and three pillars. The testing samples were wrapped around the holder and fixed by two circular clips at the top and bottom.

As shown in Fig. 4.6, the sample, the sample holder, and the PMT formed a cylindrical *cell volume*. Only the interior surfaces and the LAr volume inside the cell contribute to the light yield measured by the PMT. Since the reflectivity of aluminum in the LAr medium is not well known, all the interior surfaces, including that of the supporting rods, the surface of the top aluminum ring, and the bottom plate of the holder, were covered by an absorber. The source, ^{241}Am, was clipped at the bottom of the chamber by a small absorber foil. The foil was then fixed by metallic screws.

The absorber produced by Acktar is a highly absorbing material that has low reflectance at the concerned wavelengths, smaller than 1% according to the datasheet provided. The reflectance is shown in Fig. 4.10. The absorber can be used in cryogenic temperature and has a low outgassing rate, and was therefore considered to be suitable for this experiment.

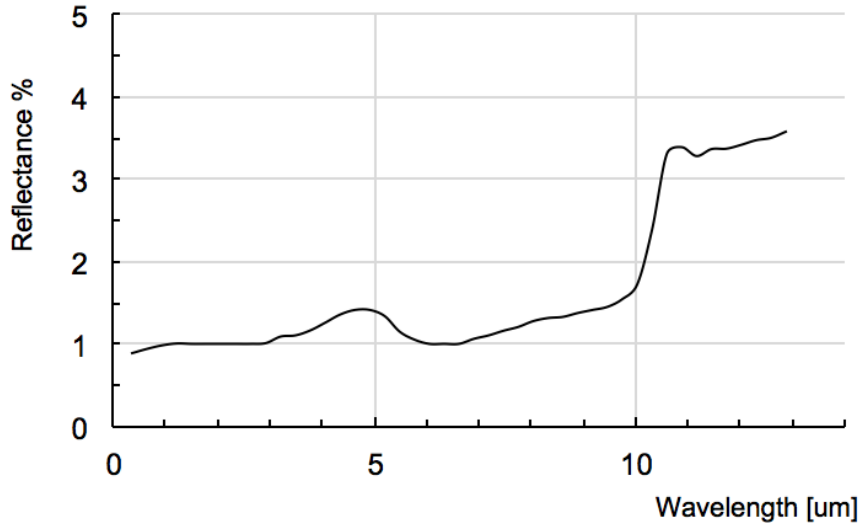

Figure 4.10: Reflectance of the absorber. Figure extracted from the datasheet by Acktar.

Samples

In addition to the 2 samples mentioned in Section 4.2, WLSR and the combination of PEN and TTX, additional samples were tested: TTX alone and the absorber sample. Table 4.1 summarizes the configuration of the measurements with different samples.

TTX is a reflective material that has a reflection coefficient above 94% in the wavelength range of the emission spectrum of the two wavelength-shifting materials at room temperature, as shown in Fig. 10 of [57]. While the reflectance in the visible range is high, that in the VUV range was not known. In the case of using TPB as the wavelength-shifter, if its absorbance of the VUV light is under 100%, some of the VUV light might pass the TPB layer and reach the TTX at the back. If TTX is also highly reflective in the VUV range, a certain proportion of the light yield might be contributed by this unshifted yet reflected light. Taking this into consideration, the goal of measuring TTX alone as a sample is to determine how much VUV light TTX reflects in LAr, such as to limit the QE and reflectance of TPB and TTX respectively, thus constraining the corresponding light yield enhancement.

When the PMT cell did not contain any light source or ^{241}Am, and the absorber wrapped around the sample holder to enclose an active volume of LAr, the PMT was measuring purely the light, either the scintillation light or Cerenkov light, due to the setup and the environment, with the minimal light enhancement. Hence, the light yield measured with the absorber being the sample but without a source was regarded as the background of the setup. This information is essential to determine the feasibility of the experiment. Since the signal from ^{241}Am is mainly alpha particles with only 30 Bq, if the setup contains another source of alpha particles with higher or comparable activity, it would be difficult to measure the light yield due to ^{241}Am. Also, the signals from the background measurement helped determine the strategy and conditions to remove the background.

Most importantly, the absorber can also serve as a reference for other measurements, considering the setup **with** ^{241}Am and the absorber as the reference sample. Assuming the induced scintillation light due to the alpha particles is close to the source, which is at the bottom center of the chamber, part of the photons would go directly to the PMT, while part of them would reach the absorber. A large portion of those reaching the absorber would be absorbed. Hence, the light yield of the PMT under this configuration would mostly be contributed to the photons going directly from the source to the PMT. For other samples, the light yield has an additional contribution from the shifted and/or reflected light. By comparing the light yield measured with other samples to that with the absorber, one can better constraint the contribution of light yield enhancement due to the samples.

Light Yield with Simplified Geometry

With the absorber as the sample in the mentioned PMT cell configuration, the PMT light yield was estimated. A few assumptions were made to simplify the calculation. First, the scintillation light was assumed to be emitted from a single point at the center of the source, since the penetration power of alpha particles is small. The calculation also omitted the reflection of light at the boundary of the PMT window and LAr, the attenuation of the

scintillation light in LAr, and the energy loss of the alpha particles before interacting with argon.

Considering the PMT cell wrapped by the absorber, all the photons reaching the wall of the cell are assumed to be absorbed by the absorber. Hence, only the photons going directly from the source to the PMT window were considered. The geometry of the light path reduced to the calculation of the solid angle of the PMT cell, as shown in Fig. 4.11 and Eq. 4.1:

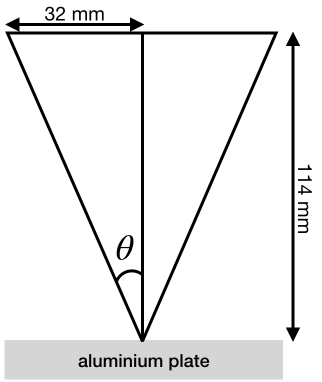

Figure 4.11: Simplified geometry of the PMT cell considered for the estimation. 32 mm is retrieved from the dimension of the PMT window. 114 mm is the distance between the source and the PMT window.

$$N_{PMT} = \frac{N_{produced}}{4\pi} 2\pi(1 - cos\theta). \tag{4.1}$$

Together with the QE of PMT at 127 nm, which is 22% given by the manufacturer, the number of PE induced at the PMT cathode was estimated to be roughly 820. More details of the light yield estimation are given in Appendix B.2.

4.4 Procedure and Data-taking

Before performing the experiment in LAr inside the cryostat, the PMT was characterized (Appendix B) and the various sensors were calibrated (Section 4.4.1). Then, LArS was filled with LAr (Section 4.4.2) and underwent the data-taking phase (Section 4.4.3).

4.4.1 Calibration of Sensors

The sensors in LArS were only calibrated at the beginning of the whole experiment, as their values between measurements did not drift significantly.

When the two PT100 were dipped into LN_2, they recorded 80.1 K and 80.8 K respectively after the reading stabilized. Since the boiling point of LN_2 is at ~77 K [6], the two PT100

have at most 3 K offset from the real value. This might be caused by the two-wire connection, instead of a four-wire connection. Since the PT100s were only dipped into a small dewar of LN_2 manually for a few minutes to check the temperature offset, hence the wire and PT100 itself were not yet in thermal equilibrium with LN_2. This would result in a slightly overestimated offset of 3 K for the PT100 readout.

The pressure was read by the PID controller, ESM4450, manufactured by RS. This controller was connected to the pressure gauge as indicated in [77]. The calibration of pressure was made by setting the pressure at 10 mBar, which was read from the pressure gauge of the pump, and the ambient pressure. The value of ambient pressure was ∼960 mBar, which is measured by the station at Affoltern, Zürich from MeteoSwiss on the day of calibration. The slow control for pressure was also made available for tracking the stability.

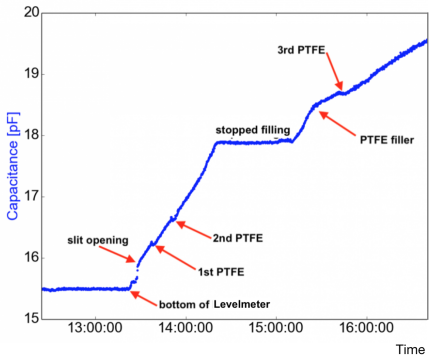

(a) Uncalibrated levelmeter reading

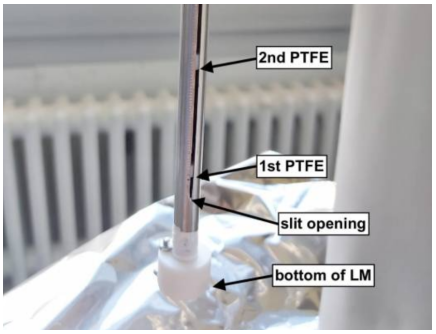

(b) Photo showing some of the features

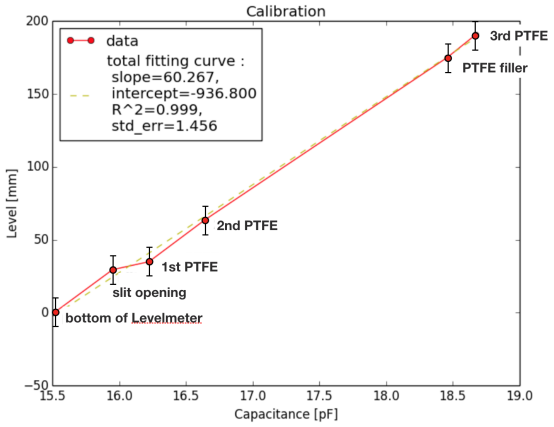

(c) Calibration

Figure 4.12: (a) Capacitance of the levelmeter during LAr filling. (b) Part of the levelmeter with some of the features marked. (c) Fitted correlation between the capacitance and the levels. 10 mm error bars are added to the level due to the rough measurement, see text.

The levelmeter is essentially a long cylindrical capacitor with a borehole and three small PTFE blocks, as shown in Fig. 4.12(b). The PTFE blocks are for calibration purposes. As the LAr fills up space inside the capacitor, the capacitance changes accordingly, hence indicating the level of the LAr. However, the relation between the two quantities requires calibrations. During the filling, several features on the time profile of LAr level were iden-

tified, as marked in Fig. 4.12(a) and (b). For example, after surpassing the PTFE filler, as the LAr has to fill up more cross-sectional area, the rising rate of level became slower. The physical vertical positions of these feasured were roughly measured. Hence, 10 mm error bars were added to the position measurement, as shown in Fig. 4.12. By plotting the vertical position against the change in capacitance of the levelmeter, the conversion between the two quantities can be estimated. The levelmeter was calibrated using the slope of the correlation. A roughly estimated vertical offset was added to match the physical depth of the cryostat.

4.4.2 Measurements inside LAr

The samples mentioned in Section 4.2 and 4.3.1 were tested in the order and configurations as summarized in Table 4.1. Each configuration was counted as one *measurement*. Once the corresponding configurations of the PMT cell in Section 4.3.1 were assembled and all connections were checked, the following procedures of filling LAr were carried out for each measurement.

Table 4.1: Schedule for the measurements

Short Name of Meausrements	Start Date of Data-taking	Sample	Acrylic Disk	Source	Amplifier
Background	25/08/20	Absorber	Absent	Absent	10x
Absorber	21/10/20	Absorber	Absent	Present	Absent
TTX	16/11/20	TTX	Absent	Present	Absent
PEN+TTX (VUV+vis)	02/12/20	PEN+TTX	Absent	Present	Absent
PEN+TTX (vis)	15/12/20	PEN+TTX	Present	Present	Absent
WLSR (vis)	21/12/20	WLSR	Present	Present	Absent
WLSR (VUV+vis)	02/01/21	WLSR	Absent	Present	Absent

The system was first pumped for roughly 2 to 3 days, such that the outgassing rate was similar for each measurement. When the pressure of the cryostat reached the vacuum level of the order 10^{-5} mBar, the valve connecting the cryostat and the pump was closed for 30 seconds. The pressure immediately increased due to outgassing. The increase in pressure during this period was used to estimate the outgassing rate. As the rate was of the order of 10^{-5} mBar/s, which is the desired level for each measurements, the valve was opened again such that the vacuum level was again of the order of 10^{-5} mBar and the setup was prepared to be filled with GAr.

For all the measurements, purified argon with the level of Grade 6[3] was used for the filling and liquefied by the cooling system of LArS (Section 4.3). As the GAr started to fill up space inside the cryostat, LN_2 started entering the cooling coil. After some time, the GAr started to be liquefied and fill the cryostat with LAr. As soon as the level was above the PTFE filler, which is certainly above the PMT window, the filling of GAr was stopped. The mode of the cooling system was then changed such that it stabilized the system to the

[3] 99.9999% purity of GAr

condensation point of argon. The setpoint was chosen at $\sim 88.5 - 89$ K (with the offset subtracted), which corresponds to a pressure at $\sim 1155 - 1200$ mBar [5]. The temperature was chosen such that less cooling power was needed compared to 87 K, while the pressure was still well below the maximum pressure of the system. Supplementary details of filling LArS with LAr are in Appendix D.

After filling, the power supply of the PMT was turned on and data was taken with the DAQ system. When the data-taking process was finished, all the LAr was evaporated, as the setup does not contain any recirculation and recuperation system and the purity of argon would be degraded if reused.

4.4.3 Data Acquisition

Each *measurement* in Table 4.1 took 2-3 days for data-taking and had at least four *data sets*, and most of them with two PMT voltages and two triggering thresholds being set. Each data set recorded 10^6 events in around half an hour to one hour. The signal measured by the PMT was read by a Analog-to-digital Converter (ADC).

In most of the measurements, except the background measurement and the absorber measurement, two triggering thresholds for the DAQ were set for different data sets, which were 4 ADC unit and 10 ADC unit away from the baseline, which is the average ADC counts in the first 50 ADC samples, as shown in Fig. 4.13. The values were set such that the DAQ system was triggered by the scintillation signal but unlikely by the noise around the baseline, and the overall data-taking time was less than one hour. Besides, the chosen threshold values also allowed some events with small signals to be recorded, which were then used for the gain calibration. The result from the two different thresholds does not show an obvious discrepancy, which is expected.

It was uncertain whether the signal due to ^{241}Am source will saturate the ADC during the measurement. Hence, the value was estimated for the case of the absorber measurement (Section 4.3.1). In Appendix B.2, it was found that the ADC will be saturated if the 10 times amplifier was used in the absorber measurements with the alpha source. Hence, the measurements with wavelength-shifting and reflective samples has an even greater chance of saturating the ADC. To prevent saturation, the amplifier was not used for the measurements with the ^{241}Am source. Therefore, the amplifier was only used for the background measurement, which is the only measurement without source, but not the other measurements.

Except for the background measurement, two voltages (1350 V and 1500 V) were applied to the PMT for different data sets in all measurements. Using 1500 V as the PMT voltage gave a better energy resolution, but with more noise. Besides, it was still uncertain whether the enhanced light yield by the wavelength-shifting and reflective samples would saturate the ADC. Hence, 1350 V, which has a lower gain, was used in some data sets (see Section 4.5.2).

[4] Observed discrepancy between the set value and the actual baseline.

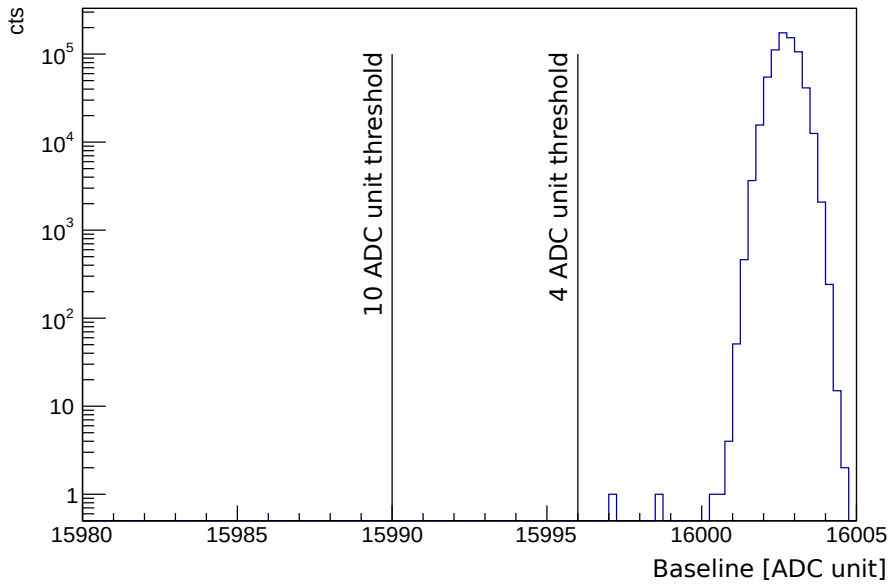

Figure 4.13: Histogram of the baseline of one of the data sets. The baseline was set at 16000 ADC unit[4]and the thresholds for the DAQ during the measurements are indicated by the black vertical lines.

The background measurement used the 12 bit ADC of type v1720 with 250 MHz acquisition rate and voltage up to 2.00 V. For all other measurements in Table 4.1, the 14 bit ADC of type v1724 with 100 MHz acquisition rate and voltage up to 2.25 V was used.

4.5 Analysis and Result

The analyses of the results are carried out using WARP, a post-processing program developed by previous students for processing the raw data from the DAQ. The program can identify peaks as well as calculate and retrieve both the global and the local properties of the events. The global properties include the integral for the full waveform, the time of the event, and the baseline. The local properties include the integral and the position of an individual peak.

It is worth mentioning the peak-finding algorithm here: a peak is identified when the ADC count surpasses the threshold. The peak ends when the count fall below the threshold for four consecutive bins. The threshold for peak finding is set to be three times the root-mean-square of the baseline.

Based on the information produced by WARP, the following analyses are carried out: correction to the triggering, gain calibration, the pulse shape discrimination (PSD), the determination of the triplet lifetime, and the determination of the light yield of different samples. They are explained in detail in the rest of this section.

4.5.1 Correction to the Triggering

During the absorber measurement, I found that the DAQ had been triggering at the wrong edge. This was because the DAQ program did not correct the polarity of the PMT signal as demanded in the configuration file. Because of this mistake, some of the large pulses were trimmed at the front (Fig. C.2), and the starting position of untrimmed pulses were not well defined. Therefore, there is a need for corrections to the absorber measurements.

The approach to making the corrections requires a closer look at the waveform. As mentioned, WARP can identify peaks and compute their properties. One of the properties, which is useful to remove the trimmed events, is the left boundary of an identified peak, as shown in the example waveform in Fig. 4.14. If the waveform of an event is trimmed at the front due to the wrong triggering edge, the left boundary of the first identified peak is smaller or equal to one ADC sample. To remove these trimmed events, the left boundary of the first peak is set to be greater than one ADC sample.

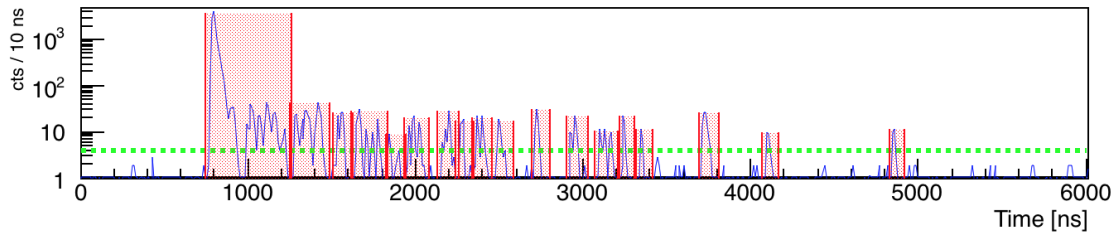

Figure 4.14: Example waveform from the TTX measurement. Each of the red boxes indicates one identified peak, whereas the red lines locates the boundaries of each peak.

Although the polarity was corrected for the measurements after the absorber measurement, it is found that the triggering position was still slightly earlier than the one being set, 1000 ns. For example in Fig. 4.16, the peaks started earlier than 1000 ns. Most of the events started ∼750 ns. In addition, as the waveforms are not perfectly triggered and start at the same position, the waveforms needed to be align when determining the triplet lifetime. The cause of the problem is not clear; yet, the left boundary of the first peak is again used to correct the wrong triggering positions and align the waveform.

In view of the issue with the wrong triggering, the pre-triggering of the signal was set for a longer period so that fewer events were trimmed. However, the post-triggering ADC samples were reduced as a consequence, which might affect the integral value and the triplet lifetime. Hence, for the later analysis, the starting position of the signal waveform of the absorber measurement is demanded to be at least 5 µs before the end of the DAQ window. For other measurements, the waveform has at least 7 µs of ADC samples with the average value being 7.25 µs. It is found that the difference in the integral of the waveform between a 5 µs range and a 7 µs range is ∼0.15%, which is negligible. More details on the effect of the wrong triggering edge are documented in Appendix C.

4.5.2 Gain Calibration

Gain calibration is performed to remove the dependence of the signal gain on the PMT voltage and the amplifier used. In this process, the measured waveform integral in one unit area of the ADC (which is dependent on the gain) is converted to the number of PE (which is independent of the gain).

The most important quantity for the calibration is the integral signal of single photoelectron (SPE), which is the signal due to one PE induced at the PMT cathode. Here the SPE signal is obtained by calculating the integral of the small peaks identified by WARP in the data set. Besides, no background or noise reduction is applied in this calibration, otherwise it might remove the small peaks signal.

Figure 4.15 shows the histogram of the integrals of the small peaks as well as the fitted Gaussian for the noise pedestal, the SPE, and the double photoelectrons (DPE). Note that the mean and the spread for the DPE are constrained to be around 2 and $\sqrt{2}$ times that for the SPE respectively.

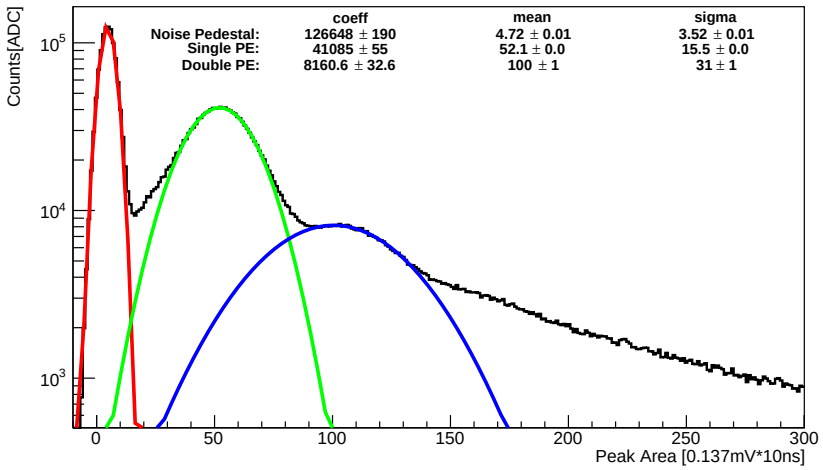

Figure 4.15: Fitted noise pedestal (red), SPE (green), and DPE (blue) for the PMT at 1350 V without the amplifier. Data taken from the TTX measurement.

The gain of a signal is the ratio between the charges collected by the ADC (which are essentially the integrals) and the charges of PEs at the PMT cathode. It can be obtained by the equation:

$$G = \frac{\text{Area [a.u.]} \times 1 \text{ ADC unit [V]} \times 1 \text{ ADC sample [s]}}{R[\Omega] \times q_e[\text{C}]}, \tag{4.2}$$

where q_e is the charge of the PE(s), "Area" refers to the integral of the signals in one unit area of the ADC due to the PE(s), "1 ADC sample" refers to the physical time corresponding to an ADC sample, "1 ADC unit" refers to the physical voltage corresponding to an ADC unit, and R is the input impedance. In the case of SPE, "Area" is the mean of the SPE peak in a unit area of the ADC μ_{SPE}, and q_e is the charge of one electron. In this

experiment, the 14-bit ADC of type V1724 was used in all the measurements except the background measurement. It has a voltage range up to 2.25 V, rate of 100 MHz, and $R =$ 50 Ohm input impedance. This results in the conversion factor of $G = 171250\ \mu_{SPE}$.

On average, the gain using 1350 V and 1500 V for the PMT is 3776063 and 8862188 respectively. After the gain calibration, the results from the two supply voltages of the PMT, 1350 V and 1500 V, are found to be compatible with each other.

4.5.3 Pulse Shape Discrimination

Background reduction is carried out for each data set and each measurement to remove the random noise and ER background. A noise cut is determined from the background measurement. Then, the alpha events are discriminated from the background using the PSD parameter.

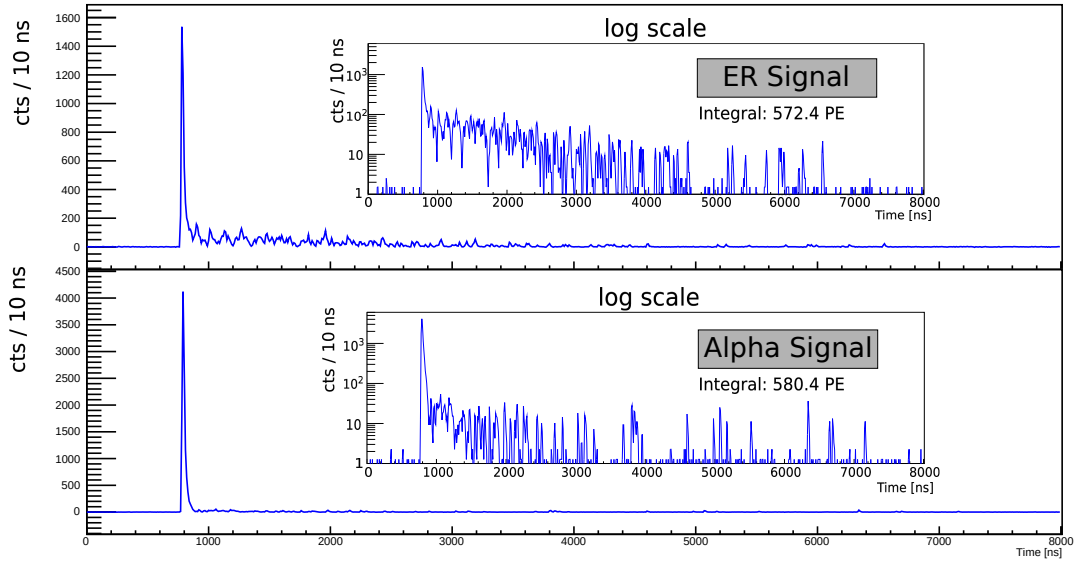

Figure 4.16: Example waveforms taken from the TTX measurement. Both waveforms have comparable integral values. The top plot shows a typical waveform of an ER event. The bottom plot shows a typical waveform of an alpha event.

As described in detail in Section 4.1 and shown in Fig. 4.16, the difference in the ratio of the fast and slow component between the two types of interaction left open the possibility of PSD. The desired signal is the light induced by alpha particles, which interact with the argon nucleus, while the background due to beta decay and gammas induce ER signal. Hence, rejecting the ER events can reduce the background efficiently.

It is later observed that the singlet component across different measurements is dominant in the first 200 ns from the start of the waveform (Fig. 4.21). Hence, the PSD parameter F_{Prompt} is introduced in this analysis, as in [75]. It is defined as

$$\mathrm{F}_{Prompt} = \frac{\text{Integral from 0 - 200 ns}}{\text{Integral of full waveform}}. \tag{4.3}$$

From this definition, F_{Prompt} is higher for NR events and lower for ER events. The histogram of F_{Prompt} of one of the data sets is shown in Fig. 4.17.

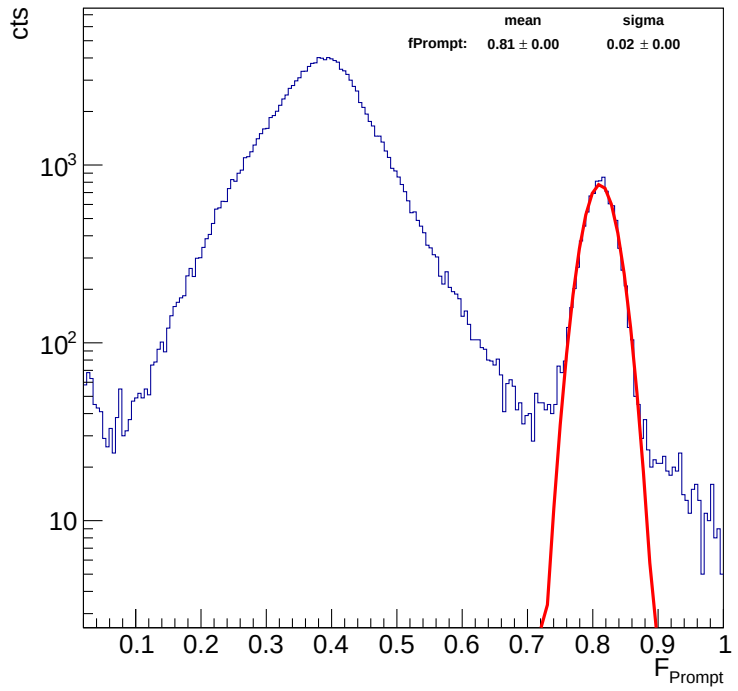

Figure 4.17: The blue line is the histogram of F_{Prompt} in a data set, the red line is the fitting of the F_{Prompt} peak for the alpha signal.

Noise Removal

While PSD can discriminate between the scintillation light due to NRs and that due to beta particles and gammas, it cannot discriminate between the alpha signal of ^{241}Am and other sources of alphas or neutrons in the setup. Hence, it is important to ensure that there was no other strong source of alpha particles or neutrons comparable to the alpha signal in either the setup or the environment.

For this purpose, the absorber was used as the sample to wrap around the sample holder during the background measurement, as mentioned in Section 4.3.1. Also, ^{241}Am was not present in this measurement. To better observe and characterize the noise level, the 10 times amplifier was used to amplify the small signals in noise. The integral value of the noise signals has been converted into the PE unit such that the result is comparable with all the other measurements that could not use the amplifier.

From the background measurement, no observable amount of NR background is present at the estimated integral value of the alpha signal, which is $\sim$820 PE, and the position of the alpha signal observed in later measurements. Hence, it is safe to use PSD to remove the ER background.

Before selecting the alpha events with the F_{Prompt} parameter, it is also important to remove the events that are triggered by noise and had a low integral value compared to the alpha signal. Instead of increasing the threshold at the DAQ stage, a noise cut is applied to remove the noise events with a low integral value. However, as shown in Fig. 4.18, when the F_{Prompt} decreased and thus the ER events start to contribute, the noise level increased. Hence, to remove the region with noise events, the mean F_{Prompt} of the alpha signal was first estimated as shown in Fig. 4.17.

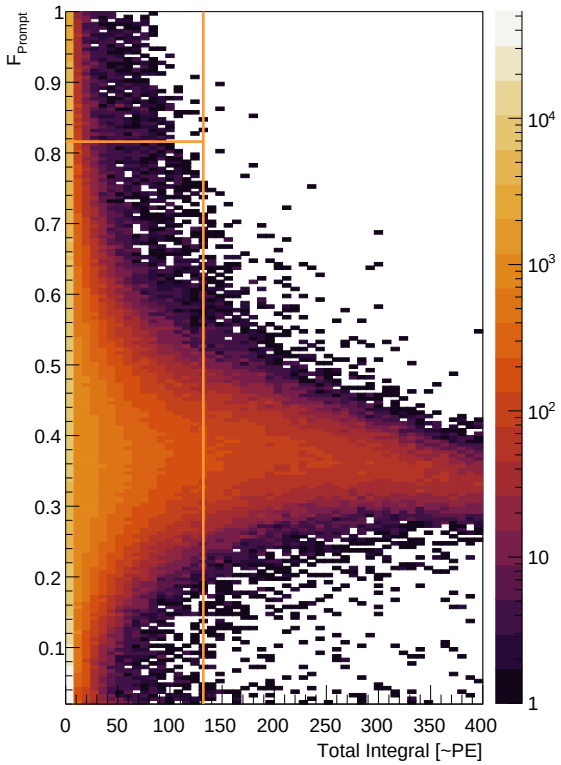

Figure 4.18: The F_{Prompt} value against waveform integral in PE. The histogram is the stack from all the data sets of the background measurement. Given the average F_{Prompt} value, indicated by the horizontal line, the corresponding vertical line indicate the position of the noise cut that removes 99.99% of the noise events within an F_{Prompt} range of 0.2.

The mean F_{Prompt} is found to be 0.82 ± 0.01 for all measurements. At this value, a noise cut, or an integral cut, is defined to remove 99.99% of the noise events within the F_{Prompt} range of 0.80 to 0.84. This range is roughly one order of magnitude wider than one standard deviation of F_{Prompt} of an alpha signal in all data sets, which is 0.02 on average. The determined noise cut is at 132 PE for all measurements.

Selection of the Alpha Events

After the removal of noise events, PSD is used to discriminate the alpha signal from the ER background. Figure 4.19 shows an example distribution of events in the parameter space of F_{Prompt} and the integral for the TTX measurement. The alpha signal appears ~600 PE

and the F_{Prompt} ~0.8. The events due to ER are centered around the F_{Prompt} value of 0.4.

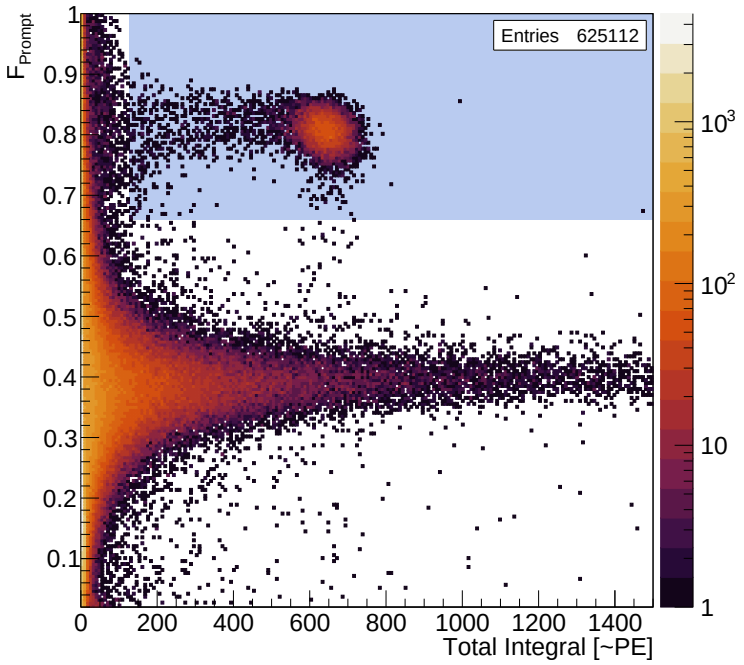

Figure 4.19: The F_{Prompt} value against waveform integral in PE. The data is taken from one of the data set of the TTX measurement. The blue, squared region is the region of interest.

For each data set, after the mentioned noise cut is applied at 132, a cleaner F_{Prompt} histogram is plotted, as shown in Fig. 4.20. Both the alpha signal and the ER signal are fitted by a Gaussian function, and the two fits are added up. The F_{Prompt} value corresponding to the minimum of the resulted functions is determined as the optimal F_{Prompt} cut, which has the optimal acceptance rate of the alpha signals and rejection rate of the ER events. The events with an F_{Prompt} above the cut are regarded as the alpha signals, while those below the cut are regarded as the ER signals. An example F_{Prompt} cut is shown in Fig. 4.20. With an improved signal-to-noise ratio due to the noise cut, F^{α}_{Prompt} is defined as the new fitted mean F_{Prompt} of the alpha signal.

4.5.4 Triplet Lifetime

The apparent triplet lifetime is commonly used as a parameter for monitoring the purity of LAr and is therefore also studied in this project; it is determined for all the data sets. Each data set is first divided into 10 *subsets* and passes through the noise cut. Brizzolari et al. showed that the NR alone, ER alone, or both together possessed different triplet lifetimes in measurement. Thus, these three types of events are studied separately. The alpha and ER events are selected using the F_{Prompt} cut. Each type of events in each subset has at least 500 events remaining after the noise cut and event selections.

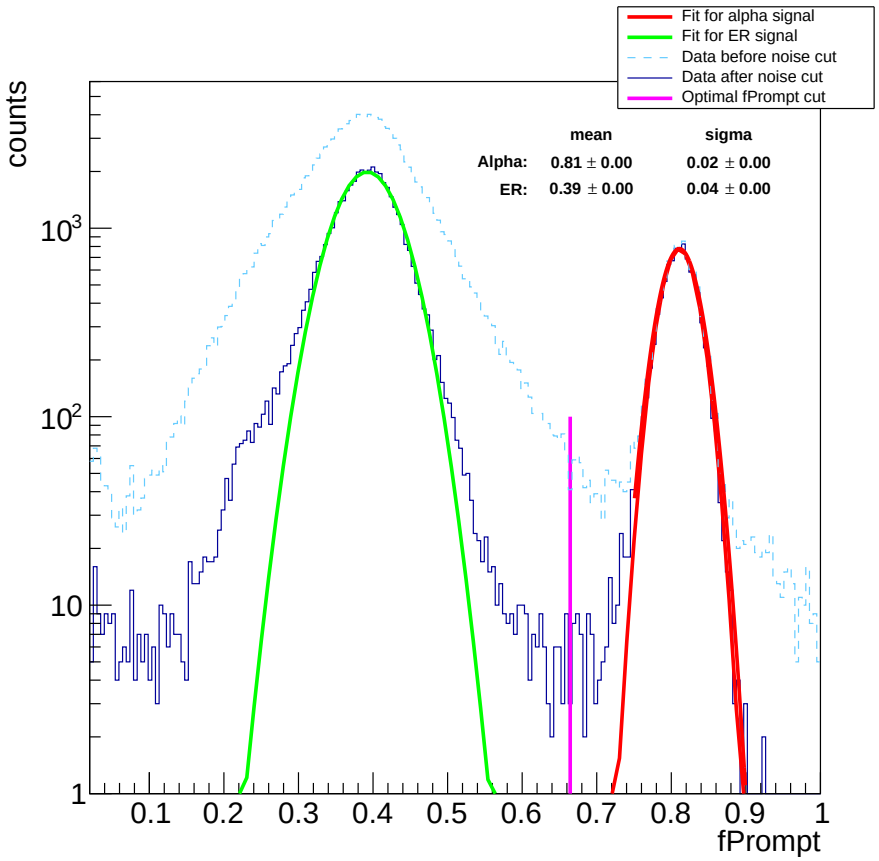

Figure 4.20: 1D histogram of F_{Prompt} before and after the noise cut. The ER events and alpha signal are fitted respectively. The optimal F_{Prompt} cut is indicated by the magenta line.

Then, the waveforms of the three types of events in each subset are aligned to the first left boundary and stacked together before fitting the triplet lifetime. Figure 4.21 shows the stacked waveforms of both alpha and ER events together. For illustration and comparison, the stacked waveforms are normalized to their peak value. Due to the fluorescence emission by the wavelength-shifters, the observed triplet lifetime of the shifted light is expected to be longer than that of the unshifted light. In the figure, the *vis* measurements, which are the measurements with the acrylic disk that blocked the unshifted VUV light, is therefore expected to have a longer measured triplet lifetime. From Fig. 4.21, both vis measurements of PEN with TTX and WLSR have a longer measured triplet lifetime than the respective VUV+vis measurements.

Previous studies show that TPB has prompt emission at 2 ns and delayed emissions in the time scale of $\mathcal{O}$(ms) [17, 62]. The delayed emission of TPB should affect the measured triplet lifetime. While for PEN, the fluorescence lifetime is approximately 20 ns [62], which is two orders of magnitude smaller than the triplet lifetime of LAr $\sim$1300 ns; therefore, it should not increase the measured triplet lifetime significantly. In Fig. 4.21, the WLSR (vis) measurement has a longer triplet component than the PEN+TTX (vis) measurement. The shape of the waveforms agree with the expectations.

On the other hand, the fluorescence lifetime of PEN is slightly greater than the singlet life-

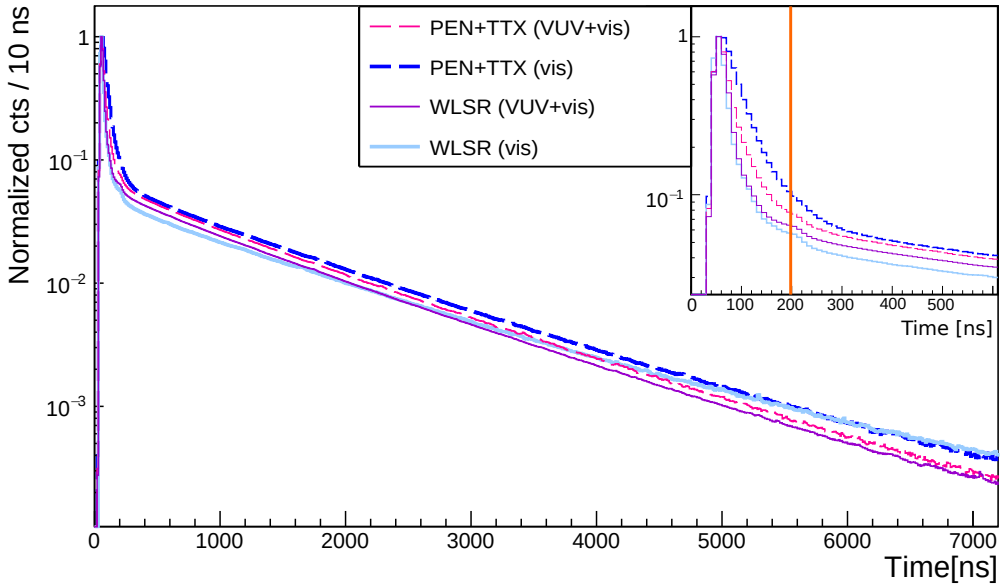

Figure 4.21: Stacked waveform of different measurements normalized to their peak values. The waveform is only stacked within one data set in each measurement. The inset zooms into the first 600 ns of the stacked waveform. The singlet component is within the first 200 ns, as marked by the orange line, where the triplet components are dominating afterward.

time of LAr, and the latter is greater than the lifetime of the prompt light of TPB. Therefore, the fluorescence emission of PEN might broaden the singlet component to a larger extent than the case of WLSR. From Fig. 4.21, the broadening of the singlet component is the most apparent in the PEN+TTX (vis) measurement, followed by the PEN+TTX (VUV+vis) measurement, as expected. The effect of prompt and delayed component of TPB on the singlet component are observed to be not significant.

After aligning and stacking the waveforms, I fit an exponential function to the triplet lifetime of each subset. A few fitting ranges are chosen. With reference to [77, 36], which is a similar experiment using the same setup and radioactive source, the fitting range is chosen to be 450 ns to 4000 ns after the start of the waveform. On the other hand, as shown in Appendix B.4, afterpulses due to the PMT is relatively prominent after $\sim$1000 ns of the signal peak. In the measurements with LAr scintillation light waveform and the wavelength shifters, the afterpulsing is broaden and also wind together with the different fluorescence emission of the samples. It is therefore not clear if the effect of afterpulses are consistent between the measurements. To avoid the effect of afterpulses, the fitting range from 2000 ns to 4000 ns is also used. In addition, a longer fitting range from 450 ns to 7000 ns is used but with an additional constant background fitting. Due to the triggering edge problem, the acquisition window of the absorber measurement is $\sim$5000 ns; thus, the absorber measurement is not fitted with the longer fitting range.

Using different event selections, I obtain three types of triplet lifetime: the triplet lifetime by stacking only the alpha signals τ_α, that by stacking only the ER events τ_{ER}, and that by stacking both signals together τ_{all}. Each of them are fitted with three fitting range. The triplet lifetimes and the error of **each data set** are respectively given by the means and one

standard deviations of the fitted triplet lifetimes of all the subsets in a data set. Based on the distribution of these values, outliers are removed, and no trend within a measurement is observed. Similarly, the mean triplet lifetimes and error of **each measurements** are respectively given by the mean and standard deviation of the triplet lifetimes of all the data sets. All of these results are shown in Fig. 4.22.

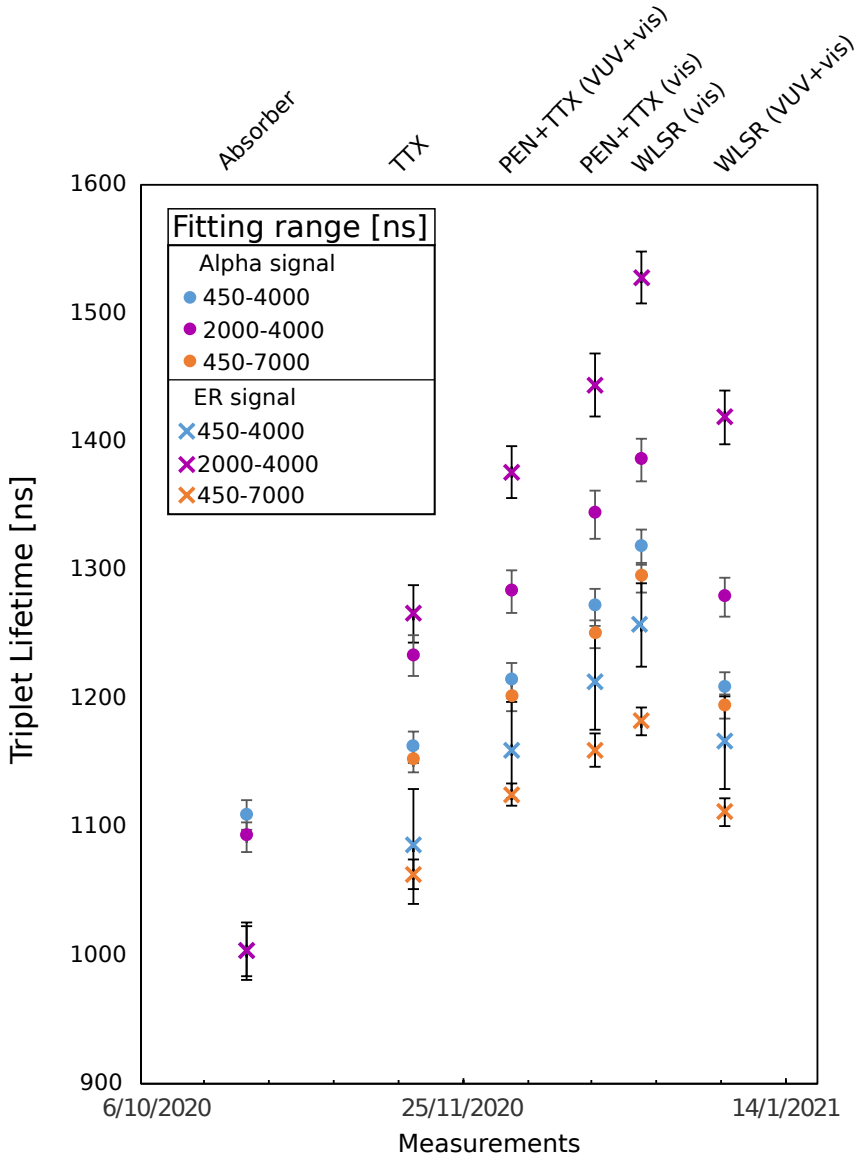

Figure 4.22: The triplet lifetimes of (circle) ER and (cross) alpha events with different fitting range.

Since the number of ER events is considerably higher than that of the alpha signal, τ_{all} is close to τ_{ER}; hence, only τ_{ER} and τ_{α} is shown in Fig. 4.22. From the figure, τ_{α} is more sensitive to the fitting range compared to τ_{ER}. This is expected as the triplet component of the alpha events by nature have fewer statistics than that of the ER events. Hence, the ER events should provide a more reliable estimation of the triplet lifetime across measure-

Table 4.2: Summary of mean and uncertainty of τ_{all}.

Measurement	τ_{ER} [ns]
Absorber	1109 ± 11
TTX	1161 ± 12
PEN+TTX (VUV+vis)	1213 ± 13
PEN+TTX (vis)	1271 ± 14
WLSR (vis)	1318 ± 14
WLSR (VUV+vis)	1208 ± 12

ments.

In [38], the reported τ_{ER} is consistently lower than τ_{α}, but this is not observed across measurements in Table 1 of [56]. In this experiment, Fig. 4.22 reveals that the measured τ_{α} is either consistently higher or consistently lower than τ_{ER} for the fitting ranges. This suggests that the relative difference between τ_{ER} and τ_{NR} might be caused by the modelling rather than intrinsic differences.

Regarding the difference between the fitting ranges, the triplet lifetimes with the fitting range of (450-7000) ns are closer to that of (450-4000) ns than that of (2000-4000) ns; it is because the number of events in (2000-4000) ns are less dominant. Consequently, it is inconclusive to which fitting range is better or if the values can be combined. In order to be comparable with previous experiment [77], τ_{ER} with the fitting range of (450-4000) ns is used as an estimate to the triplet lifetime and is reported in Table 4.2.

In [18], the authors carried out a thorough analysis on modelling the time profile of the LAr scintillation light. Different contributions to the light, such as the intermediate components of LAr light, afterpulsing and the delayed emission from TPB, were included for modelling the full waveform. According to their results, the triplet lifetime can vary by $\sim$ 13% depending on the TPB emission model used in the fitting. In this experiment, due to the limited acquisition window, it is difficult to model the TPB delayed emission. Therefore, the triplet lifetimes reported are only rough estimates.

The errors in Table 4.2 can only indicate the consistency of the values in one measurement; but they can neither indicate the effect of the smeared afterpulses and the delayed fluorescence emissions of the shifted light nor the change in purity between measurements. Nevertheless, the absorber measurement and the TTX measurement should not be affected by the delayed fluorescence as no wavelength-shifting material was presented, and the effect of afterpulses on both measurements should be the same. Also, the additional time due to reflections inside the small cell volume (Fig. 4.11) had negligible contribution to the lifetimes. Hence, the discrepancy of the estimated τ_{ER} between the TTX and the absorber measurements might be caused by the change in purity.

For the measurements using wavelength-shifters, it is difficult to distinguish between the effect on triplet lifetime due to afterpulses, the fluorescence emissions, and the purity. Hence, the discrepancies of the triplet lifetimes in these measurements do not directly and conclusively indicate the change in purity in the setup. Other measures, which will be

described later, are taken to ensure that all the possible change in purity did not affect the light yield.

4.5.5 Light Yield of Different Samples

To determine the mean light yield and the corresponding error in each measurement, each data set is divided into five subsets. The rationale behind the choice of five subsets is explained later in this section. The subsets undergo the background reduction process. With the noise cut and the F_{Prompt} cut that select the alpha events, a rectangular region of interest (ROI) in the parameter space is defined in each subset (e.g. Fig. 4.19). For each event inside the ROI, the waveform integral is calculated as the sum of ADC counts above the baseline, with the range from the triggering position to the end of the DAQ window. The integrals in PE are histogrammed as shown in Fig. 4.23. A peak in the integral histogram is the signal due to alpha particles. The figure also demonstrates that the cuts remove a substantial amount of background yet retain almost all of the alpha signals at the same position. The low integral tail of the main peak represents the degraded alphas that lose their energy before inducing the scintillation light.

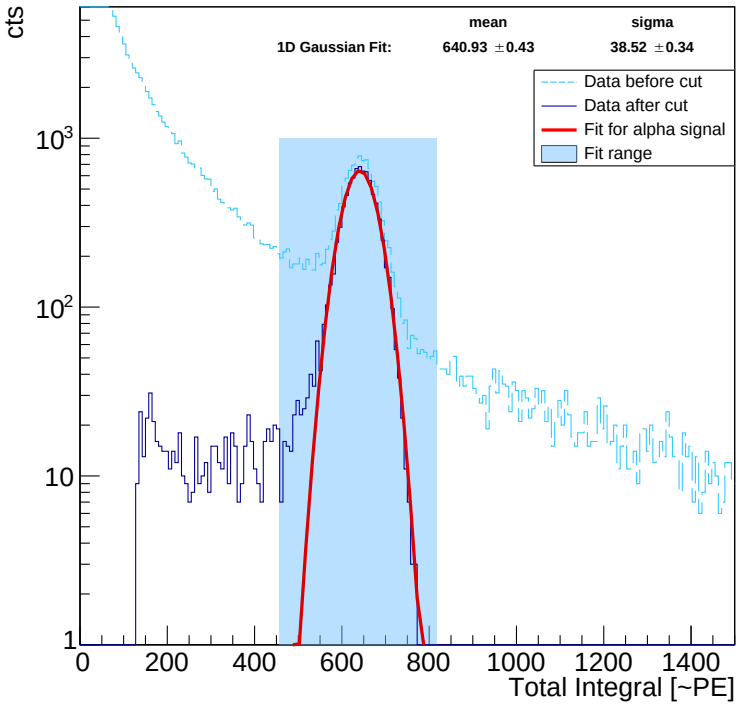

Figure 4.23: Projection of Fig. 4.19 onto the integral values. The integral histogram before event selections are also shown for comparison.

The Gaussian function is fitted to the alpha peak. The mean value of the fit is regarded as the light yield of each subset. The final light yield and error of each measurement is calculated using the mean and one standard deviation of the light yield in PE of all the subsets in the measurement. Hence, the number of subsets is set such that the total number of subsets in each measurement is at least 10, while the number of events in each subset after

Table 4.3: Summary of mean and uncertainty of the light yield for all measurements.

Measurement	Absolute Light Yield [PE]	Relative Light Yield [PE]
Absorber	567 ± 25	1
TTX	610 ± 25	1.08 ± 0.06
PEN+TTX (VUV+vis)	1071 ± 40	1.89 ± 0.11
PEN+TTX (vis)	362 ± 13	0.64 ± 0.03
WLSR (vis)	747 ± 33	1.32 ± 0.08
WLSR (VUV+vis)	1238 ± 36	2.18 ± 0.11

the background reduction is still sufficient for the Gaussian fit.

Table 4.3 and Fig. 4.24(a) show the measured absolute light yield for each measurement listed in Table 4.1. The light yield enhancement of each measurement relative to the absorber measurement is shown in Fig. 4.24(b). Again, the errors in the table and figures indicate the consistency of the value within one measurement but not the uncertainty in the change in purity between measurements or the delayed fluorescence emissions of the shifted light.

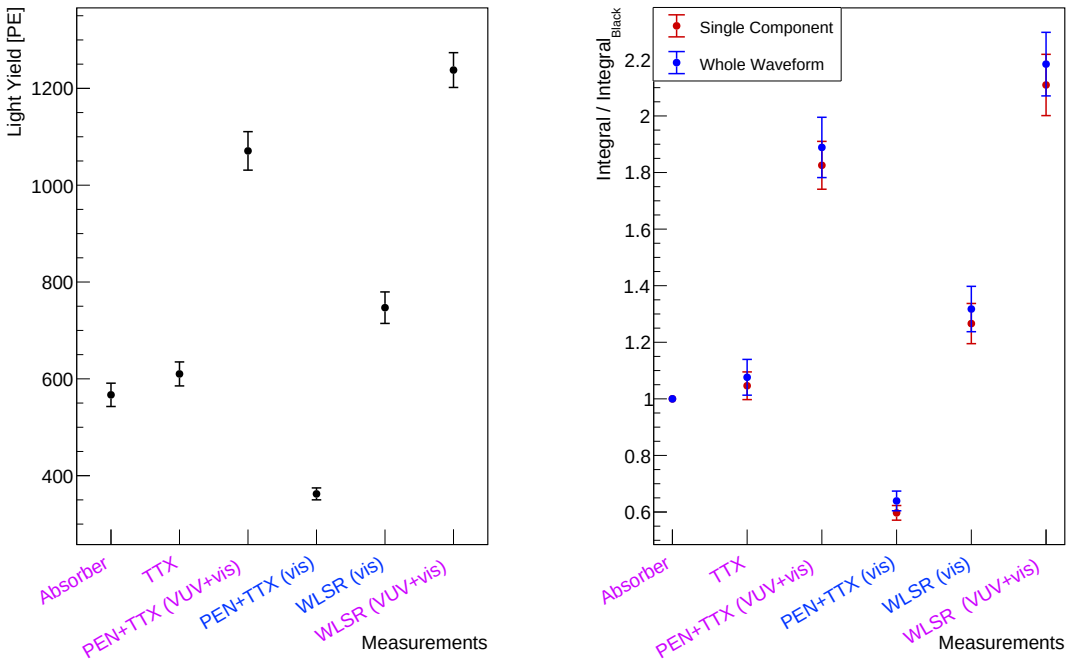

(a) Absolute LY

(b) Relative LY

Figure 4.24: (a) Absolute LY across the measurements. (b) The relative light yield to the light yield of absorber measurement.

Compared to the estimated light yield in Section 4.3.1 of the absorber measurement, which is ∼820 PE, the actual light yield measured is 567 ± 25 PE. With TTX alone, the light yield enhancement relative to the absorber measurement is only 8%, yet the possibility of 0% reflectance cannot be excluded with 2σ. This implies that the VUV light reflectivity of

TTX is not high. On the other hand, the light yields of the VUV+vis measurements for both the PEN with TTX and WLSR samples are significantly higher than that of the absorber measurement, with the percentage increase of 89% and 118% respectively. The light yield enhancement of WLSR is slightly larger than that of PEN with TTX. Note that the quoted percentage can be used to extract QE in a simulation. Various complications need to be taken into account, for example the reflection between material, the geometry of the setup, and the transmittance of the acrylic disk. Hence, a higher light yield enhancement for WLSR does not imply that the QE of TPB is higher than that of PEN.

Singlet Light Yield

In order to confirm that the light yield is not affected by a possible change in purity level, which cannot be inferred from the estimated triplet lifetime, additional checks are carried out. One check is using the singlet component of the waveform. While the triplet component in the light yield calculation is sensitive to impurities, the singlet component is less sensitive [13, 14]. Although it is incorrect to consider only the singlet component for determining the absolute light yield, the relative light yield between measurements should be the same for either the single component or the full waveform. When the relative singlet light yield deviates from the relative full light yield, it indicates the purity in that measurement has either worsened or improved so much that it cannot be compared with other measurements. This additional check can therefore be used to cross-check the result of the absolute light yield in Table 4.3.

The singlet component is chosen to be the first 200 ns of the waveform, so as to be consistent with the F_{Prompt} definition. The the mean values and the errors of the singlet light yield in each measurement is the same as that of determining the absolute light yield described above.

The singlet and the full light yield relative to that of the absorber measurement is shown in Fig. 4.24(b). The relative singlet and full light yield are consistent with each other for all measurements. This leads to the conclusion that the measured light yield in this experiment is not sensitive to the change in purity between measurements. The same result could also be supported in Fig. 10 and 11 of [14].

Acrylic Disk Measurements

Another verification is the consistency between measurements with and without the acrylic disk. For the vis measurements, that is with the acrylic disk, the unshifted light is blocked. Hence, the light yield of the two measurements is lower than the respective VUV+vis measurements, as shown in Fig. 4.24. The main contribution of the unshifted light is the light going directly from a position near the source to the PMT, which is essentially the light yield of the absorber measurement. Therefore, the sum of the light yield of the absorber measurement and the vis measurement should be comparable to the VUV+vis measurement.

For the PEN with TTX measurements, the summed light yield is 929 ± 28 PE, which is comparable to the light yield of the VUV+vis measurement (1071 ± 40 PE). For the WLRS with TTX measurements, the summed light yield is 1314 ± 41 PE, which is again comparable to the light yield of the VUV+vis measurement (1238 ± 36). Hence, the vis measurements, which served as the cross-check between measurements, generally match the expectations.

As shown in Fig. 4.3, the acrylic disk blocked more PEN emission spectrum than the WLSR spectrum. This might explain why the summed light yield in the PEN+TTX measurements are slightly lower but not for WLSR.

Although the experiment could be improved through better purity monitoring, given that the vis and the VUV+vis measurements are consistent with each other and the relative singlet light yields are consistent with the relative full light yield, the conclusion remains valid that the measured light yields in this experiment are not sensitive to the change in the purity of LAr.

4.6 Possible Improvements

If this experiment or a similar experiment will be carried out, the following improvements should be implemented to obtain better results.

First of all, redoing the absorber measurement at the end of the whole experiment is beneficial. It can serve as a stability check, confirming that the setup condition did not changed during the measurement. Although the comparison between measurements with and without the acrylic disk also checked the consistency between measurements and determined the amount of shifted light yield, the measurements were also affected by other factors at the same time, such as the transmittance of the acrylic disk. Hence, it is useful to measure the absorber measurement again to additionally confirm the stability of the setup. Furthermore, it is important to perform the absorber measurement carefully, as all measurements afterward depend largely on this reference measurement.

In addition, improvement could be made in the base of the PMT. Here, it was made of regular printed circuit board material, FR7, the outgassing rate of which is not desirable for this kind of experiment. As alternatives, a base with Cirlex substrate, which has a lower outgassing rate, could be used to obtain an even better purity of LAr and probably a better control on the purity across measurements.

Regarding future works, the reflectance of TTX for visible light in LAr should be determined as well. Although the reflectance of TTX in air is known, the simulation for this experiment also relies on the reflectance of TTX in LAr, which, however, remains uncertain. Although the setup had a blue light-emitting diode (LED) installed, the LED was not suitable in cryogenic environment as tested by dipping the LED into LN_2. Hence, the planned measurement to also determine the reflectance of TTX in LAr could not be carried out. In future measurement, a cryogenic LED light source or an LED coupled to an optical fiber is needed to measure the light yield enhancement of visible light due to TTX.

4.7 Conclusion and Outlook

In this experiment, the WLSR and PEN with TTX were characterized as the wavelength-shifting and reflective samples respectively. To achieve this, a LAr setup was used. The sensors of the setup and the PMT were calibrated and studied. The setup was filled with LAr seven times for seven different measurements, including two PEN with TTX measurements and two WLSR measurements, each one with the acrylic disk and the acrylic spacer respectively. Also, the background measurement, the absorber measurement, and the TTX measurement was carried out with the acrylic spacer for different purposes.

Table 4.2 and Table 4.3 summarize the result of this experiment, with the τ_{all} and the light yield for each measurement. The triplet lifetime quoted in the table is the value using only ER signals and only serves as an estimate.

It is observed that τ_{all} has a trend (Fig. 4.22), ranging from 1080 ns to 1285 ns, throughout this experiment. However, the change in triplet lifetime does not solely depend on the purity of LAr but also on the delayed emission of the wavelength-shifting reflective samples and afterpulsing of the PMT. Without a good modelling of the LAr scintillation light profile, it is difficult to associate the triplet lifetime to the purity. Alternatively, two measures are used to check if the possible change in purity affects the light yield. In the end, it is justified that the light yield measured is not sensitive to the change in the triplet lifetime.

From the current result of light yield, a few conclusions are made. First, the 8% light yield enhancement in the TTX measurement relative to the absorber measurements implies that the TTX does not reflect the VUV scintillation light of LAr significantly, as compares to its reflectance of visible light. Also, the light yield enhancement of WLSR relative to the absorber measurement, which is 118%, is greater than that of the non-optically coupled combination of PEN and TTX, which is 89%. Both samples significantly enhanced the light yield compare to the absorber and TTX measurement.

In order to quantify the accurate QE and reflectance of the materials, simulations must be performed, as the values depend on other parameters, for example, the solid angle, the transmittance of the acrylic disk, and the refraction across boundaries.

Apart from the result, this experiment also tested that the XUV-IR range absorber can be used for this kind of optical characterization in a LAr medium. Although the material has to be handled with care, the performance was reasonable as observed by naked eyes and from the light yield result.

Chapter 5

Conclusion and Outlook

To solve the mysteries of the nature of neutrinos and the matter-antimatter asymmetry problem, the search for $0\nu\beta\beta$ decay is ongoing with the effort of many scientists in different experiments. Among these, the GERDA and LEGEND experiments use germanium detectors, which have the best energy resolution and lowest internal background in the field. The former experiment sets the most stringent lower limit to date on the half-life of $0\nu\beta\beta$.

Energy calibration is one of the main component of these experiments. The calibration is performed by inserting ^{228}Th next to the detector array with the energy threshold at about 400 keV. While scientists are looking in the energy range below 400 keV of the GERDA data in the search for Super-WIMP, neutron disappearance and to achieve a better background modeling, it was not clear whether the linear calibration curve obtained at high energy region could be extended down to the low-energy region. In this study, by modifying the existing analysis tool, I found that the linearity of the energy scale down to 238 keV is rather good with only around 1% or smaller deviations from it. Hence, for the analysis of GERDA data in the low energy range, one can assume that the energy scale is linear down to 238 keV. The deviation can also be used as the uncertainty.

Another important aspect of these sensitive experiments is to minimize the background as much as possible. Among the techniques used to remove the background, GERDA and LEGEND use the LAr veto system, which can reject events coming from outside of the detectors as well as shield the backgrounds. The veto system collects the LAr scintillation light due to external events. The more light collected by the light detectors, the more efficient the veto efficiency will be. The use of wavelength shifters and reflectors would help increase the light yield.

In this project, two sets of wavelength-shifting and reflective sample are studied: WLSR, i.e. TPB with TTX, and PEN with TTX. The former is the witness sample from the LEGEND-200 experiment. It is found that the measurements in this experiment are consistent and comparable with each other. Hence, a few conclusions can be drawn. Firstly, only 8% light yield enhancement was measured in the TTX measurement, meaning that TTX does not reflect much VUV light. Secondly, WLSR increased the light yield by 118% relative to the absorber measurement; the combination of PEN with TTX increased

the light yield by 89%. Both samples enhanced the light yield, while WLSR showed a large enhancement compared to the PEN with TTX sample in this experiment.

With these measurements, simulations should be used to retrieve the intrinsic parameters of WLSR, PEN, and TTX, such as their reflectance and QE. The result will not only benefit LEGEND-200 for the simulation of the LAr veto system but also future large-scale LAr experiments. Moreover, the study shows that PEN with TTX is an alternative to WLSR for these LAr experiments as it also enhances the light yield which is comparable to WLSR while being easier to manipulate and scale up.

The LEGEND experiment is one of the most competitive experiment in the field, mainly searching for $0\nu\beta\beta$. The upcoming experiment is the LEGEND-200 experiment located at Laboratori Nazionali del Gran Sasso (LNGS). The experiment uses 200 kg enriched germanium detectors and is expected to begin at the end of 2021. As the first stage of the LEGEND experiment, its goal is reaching a half-life sensitivity of 10^{27} yr after five years of operations in a quasi-background-free region.

Building upon LEGEND-200, the next-generation experiment LEGEND-1000 plans to use 1000 kg germanium and operate for 10 years starting from 2026-2027. The goal for LEGEND-1000 is to reach a discovery sensitivity at 10^{28} yr with the background of 0.025 counts/FWHM-t-y [11].

Appendix A

Modifications to the Calibration Software

As introduced in Chapter 3, apart from modifying the analysis package such that it fits only the high energy peaks for the calibration curve and fit the low energy peaks, other setting were also changed to increase the calibration accuracy. This section provides the details of these modifications made specifically for this low energy calibration.

Missing Peaks

Compare to Fig. 3.3, many low energy and high energy peaks were not found by the TSpectrum method in this low energy calibration spectrum, as shown in Fig A.1(a), although the peaks are clearly visible by eye. This would affect the analysis in two ways. First, with the limited number of identified low energy peaks, the linearity of the detectors down to low energy region is inconclusive. This can be solved by manually fitting the low energy peaks, as described in a later section. More importantly, some of the high energy peaks were also not found. Although those peaks usually have lower counts and would have less effect on the final calibration curve, some detectors ended up having only two high energy peaks for the calibration curve, which is undesirable, as shown in Fig. A.1(b).

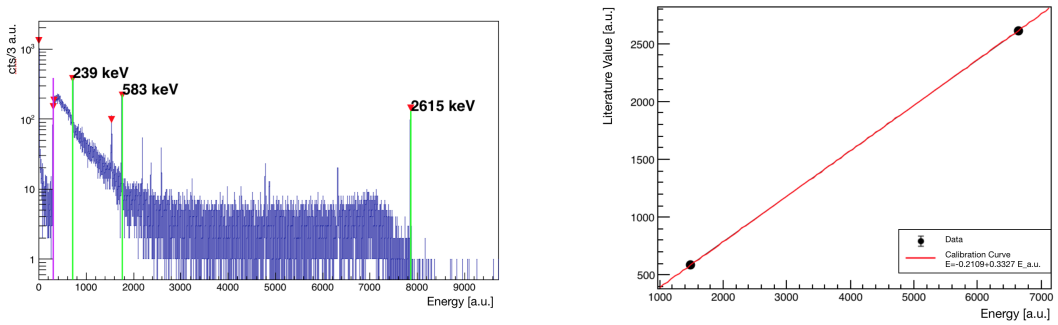

(a) Spectrum

(b) Calibration Curve

Figure A.1: Calibration spectrum and curve of detector GD00B with a Gauss filter. (a) Peaks were not found by the unmodified analysis tool. (b) The calibration curve with only two points as the peaks were missing.

In the unmodified analysis package, the peak finding threshold was set to 5% of the peak with the highest count. However, in this special calibration run with a low threshold, the

noise pedestal in FADC and Gauss filter is much higher compare to the normal calibration runs, such as in Fig. A.1(a). Instead of the 2.6 MeV peak being the peak with the highest count, the noise peak has the highest count most of the time in this calibration. This problem is not observed with the ZAC filter. To improve the situation, the noise peak in the front was trimmed for FADC and Gauss filter. The threshold was also changed from 5% to 2% of the peak with the highest count. This was done for all filters.

Modifying Cut Parameters

The fitting goodness of a peak is assessed by the fitting quality cuts mentioned in Section 3.3.1. Since the criteria are only optimized for the high energy peaks, some low energy peaks could not pass even though the fitting appears reasonably good by eye. At the same time, one should not lower the criteria too much such that wrong fittings do not pass to the next stage. One of the quality cut is to remove the peaks with their fitting amplitude smaller than 2.5 times the background level. It was observed that this cut removed many low energy peaks with good fittings. Hence, it was changed such that only the fittings with amplitude smaller than 1.5 times the background level were removed.

Threshold Estimation

In the calibration package, a baseline is set to be the root-mean-square of the noise level. The first 100 bins of the energy spectrum is chosen to calculate the baseline; hence, they are not considered in the peak finding process. For the spectrum after the first 100 bins, if the spectrum has an abrupt change in the number of counts, i.e. 8 times greater than the baseline, an energy threshold of spectrum is defined there, shown as the magenta line in Fig. 3.3. The peaks in following 20 bins of the energy threshold threshold are removed from the set of peaks as they are considered to be too close to the threshold. Yet, this method of estimating the energy threshold failed for the ZAC filter data set of the low energy calibration run.

Since the ZAC filter is optimized for each detector, the energy scale can change from detectors to detectors [72], resulting that some detectors have a low energy threshold in arbitrary units. For detectors RG2, GD79B, GD91D, GD32D, GD89A, and IC48B, their actual energy threshold after energy reconstruction is less than the first 100 bins of the spectrum in the arbitrary unit. Hence, the baseline was pulled to a much higher number of counts. Then, the first abrupt change after the baseline became P238 instead of the actual energy threshold, as shown in Fig. A.2 in comparison to Fig. 3.3.

As this lowered the number of statistics for P238, the energy threshold estimation was removed by setting the 100 bins baseline to 0 bin baseline. The modification did not cause additional problems as the matching and fitting cuts already removed the peaks that are too close to the actual energy threshold.

Manual Fitting

Some of the peaks were still not identified or fitted after the modifications above. Hence, they were fitted manually. This was done only for P277 and P300. Despite that P238 was

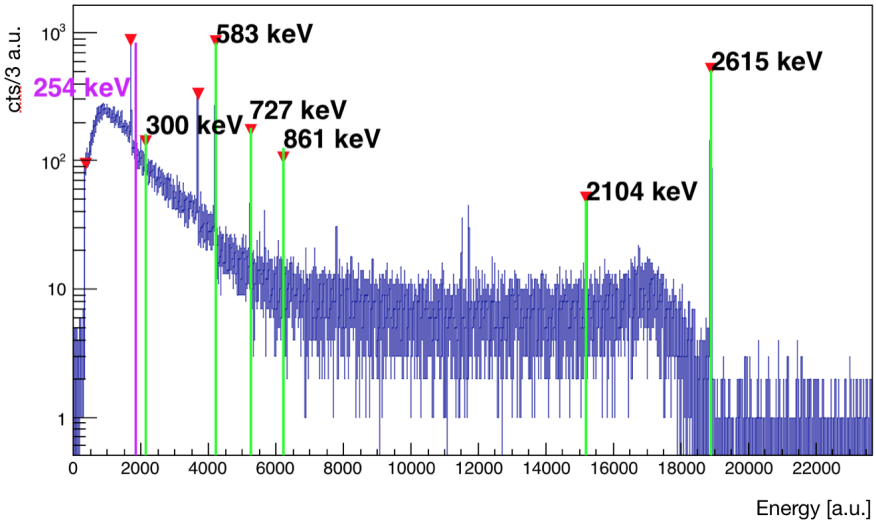

Figure A.2: Spectrum of detector GD91D with ZAC filter. From the histogram, the threshold, which is in magenta, is estimated at 254keV, thus trimming the peak P238.

also sometimes missing, the number was insignificant compare to P277 and P300. Hence, P238 with high statistics was not fitted manually.

As described in previous sections, P277 and P300 are peaks with low statistics. Hence, a Gaussian function with a linear background was used to fit the peaks. The initial guess position was estimated by the calibration curve from the high energy result. Then the peaks were fitted using the same mechanism as in the analysis tool. The fittings were then examined manually, so that some good fits which do not pass the goodness check were remained.

Fig. 3.3 shows an example spectrum after all these modification was made, where both low energy peaks and high energy peaks were found.

Appendix B

PMT Characterization

The preliminary PMT characterization has several purposes. Although the calibrated gain was not used in late experiments, the characterization helped foresee that the PMT would be stable within each data-taking, predict whether the signal from the alpha source might saturate the Analog-to-digital Converter (ADC), and determine if the dark count (DC) rate affects the measurement. The effect of afterpulse was also checked.

Since the purpose is to characterize the PMT, no LAr or samples were involved. The PMT was installed inside a light-tight, grounded black box with PMT feed-throughs. A blue LED was also presented in the black box. The PMT was connected to a power supply of type N1470 from CAEN, which provided the supply voltage of 1500 V. The output signal of the PMT was amplified roughly 10 times by a differential amplifier, which is an amplifier made internally, before entering the ADC. The ADC used in this characterization is the 14 bit ADC of type V1724 from CAEN with the acquisition rate at 100 MHz.

B.1 Gain Calibration

As mentioned in Section 4.5.2, the most important quantity for the calibration is the integral signal from a single photoelectron (SPE). To measure the small SPE signal, the blue LED light, which acted as the light source, was set as dim as possible for the characterization. The light was connected to an external signal generator. The signal generator provided the triggering for the DAQ at the same time. The voltage output from the signal generator was 2.1 Vpp, with a frequency at 3 kHz, and a pulse width of 80 ns.

The histogram of integrals of the signals detected by the PMT when pulsing the dim LED is shown in Fig. 4.15.

Since the ADC used in this characterization is type V1724 as well, hence the conversion is the same as in Section 4.5.2. With the PMT supply voltage of 1500 V and the x10 signal amplification, μ_{SPE} is at 316.9 ± 0.6 unit area of ADC, as shown in Fig. 4.15. Hence, the gain is around 54.3×10^6.

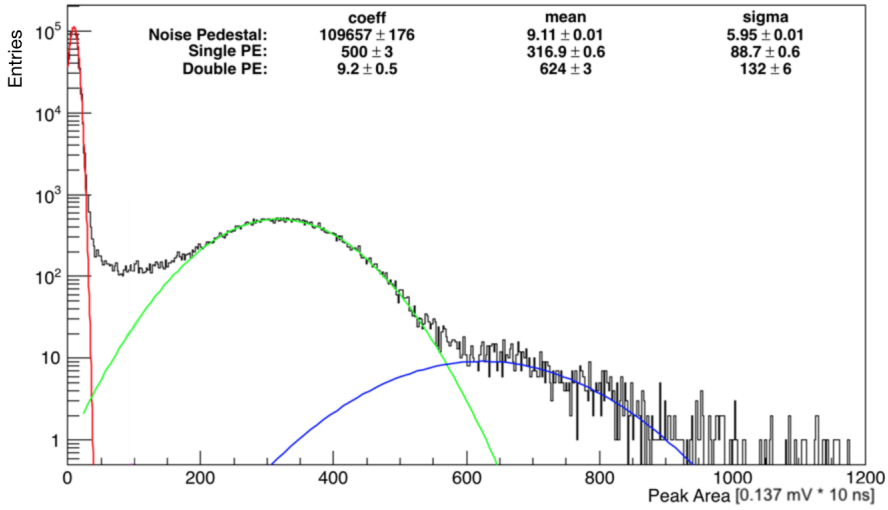

Figure B.1: Fitted noise pedestal (red), SPE (green), and double PE (blue) for the PMT in 1500V and with x10 amplifier.

B.2 Saturation

It was estimated whether the signal due to ^{241}Am source would saturate the ADC in the measurement with absorber as the sample. The calculation also provided the expected value of the light yield in the measurement.

The emission spectrum of the alpha particles is shown in Fig. 4.7, with mostly the alphas of the energy 5.486 MeV [36]. To simplify the calculation, only the alpha with this energy was considered. The W-value[1] of alpha in LAr was measured in [47] to be 27.1 eV , meaning that 27.1 eV energy deposition can induce one scintillation photon. Hence, one alpha particle with energy 5.486 MeV would induce roughly $5486/27.1 \approx 203$k photons.

With the assumptions and geometry of the PMT cell mentioned in Section 4.3.1, the number of photons reaching the PMT would be roughly 3274 photons. Corrected by the QE of PMT at 127 nm, which is 22% given by the manufacturer, the number of PE detected would be roughly 820 PE.

As mentioned, with the PMT voltage of 1500 V and x10 amplifier, 820 PE would create the signal with roughly 260k ADC unit area using the conversion in Section 4.5.2. As mentioned in Section 4.1, for the alpha waveform, around 60-70% of the light yield concentrates in the singlet component, which is roughly the first 90 ns. Then, for the signal with around 260k ADC unit area, around 182k ADC unit area will be concentrating in the first 90 ns, that is 9 ADC sample for the ADC v1724 with 100 MHz. Even if the signal spread equally in the first 9 ADC sample (90 ns), the ADC count would have exceeded 20000 unit. In comparison, the 14-bit ADC has only 16384 ADC unit. Hence, for a real signal waveform with the exponential decay shape, like in Fig. 4.21, the amplified light yield of the ^{241}Am source would easily saturate the ADC in the absorber measurement, let

[1] The energy deposition needed to produce one scintillation photon.

alone the measurements with wavelength-shifting and reflective samples. To prevent saturation, either the ^{241}Am source is absent or the amplifier is removed from the measurement.

B.3 DC Rate

DC rate is the rate of the current signal due to the thermal excitation of the electrons in the PMT. To measure the genuine DC rate, the PMT was settled in dark for 2 days before the measurement. The number of ADC samples taken was 5000, equivalent to 50 μs for each event and 20000 events were recorded. Hence, the ADC samples for all events last for 1 second in total. The ADC was triggered by the computer with a constant frequency at 10000 Hz. Since the ADC was triggering at a constant period of time, no threshold being set was being set at the level of DAQ.

During the offline analysis, different thresholds in PE for the peak integral were set, so as to check the dependence of the DC on the thresholds. A peak with the integral above the given threshold was counted as a DC. The DC rate was calculated by dividing the number of counts by the time measured by the ADC samples.

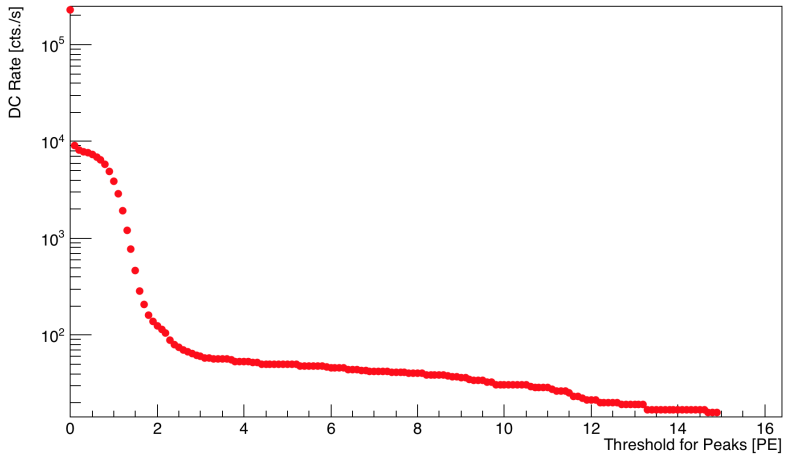

Figure B.2: DC rate with the threshold lower than 15 PE.

Fig. B.2 shows the DC rate for each threshold. From the figure, with the threshold at around 2PE, the order of DC rate dropped drastically to O(100 Hz). Starting from the threshold of 10 PE, the DC rate starts to drop below 30 Hz. In addition, during the measurements, the DC rate should be further reduced when the PMT was immersed in LAr. The drop in temperature reduces the thermal noise substantially. However, the true DC rate at LAr temperature was not determined in this experiment. Even without a radioactive source, the scintillation light and Cerenkov radiation in LAr due to other backgrounds, apart from the DC, could contribute to the signal measured by the PMT. Hence, it was only estimated from the above information that the DC would not be an issue for this measurement.

Apart from the temperature of PMT, the DC rate also depends on the gain of the signal, which depends on the PMT voltage and amplification. In this DC measurement, x10 amplifier was used; while for most of the measurements in Table 4.1, no amplifier was presented, which the DC rate might further decrease. A lower PMT voltage, 1350 V, was also used during those measurements in LAr, resulting in a further reduction in DC rate.

The estimated light yield value due to the *alpha signal*, which is 820 PE, is way above the region with a high DC rate in Fig. B.2. With the further reduction of DC rate in LAr, the DC would not be in competition with the alpha signal, which might have the activity of around 15 Bq, in LAr.

B.4 Afterpulse

Afterpulses of PMTs are the signals produced by various causes shortly after the main signal [39]. Depends on the time scale and intensity, it may affect the determination of the triplet lifetime. Hence, the afterpulse of the PMT in this experiment, R11065-MOD, was checked using the blue LED inside the black box.

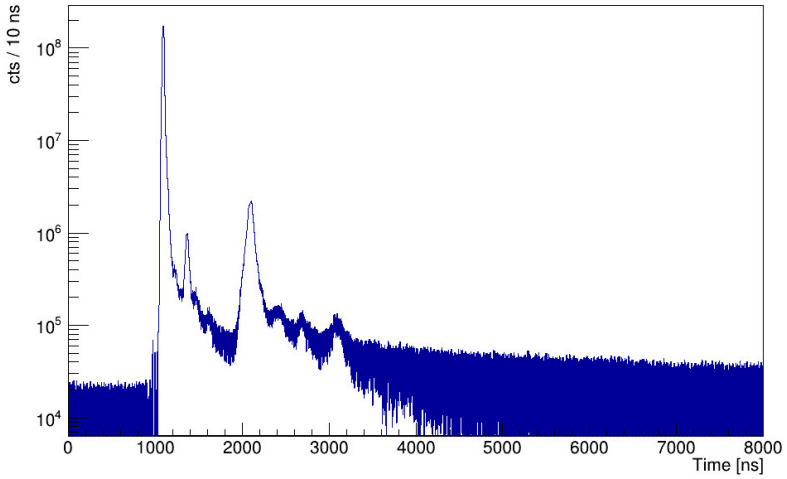

Figure B.3: Afterpulses from the PMT.

The settings of the signal generator were the same as those for gain calibration measurement. Fig. B.3 shows the afterpulses of this PMT using LED as the light source. The peak at 1000 ns is the signal due to the LED light, while the rest after 1000 ns is due to afterpulses. From the figure, the intensity of the most prominent afterpulse at around 1 μs is far less than that of the LED light. Besides, instead of having a long component, the afterpulses have an iconic peak at around 1 μs. In case the intensity of the afterpulses are comparable to the triplet component of the LAr scintillation light, the iconic peak can be easily identified. Hence, afterpulse was a problem for this experiment.

Appendix C

Triggering Edge Problem

Because of the wrong triggering edge and that the pre-triggering was only 3000 ns for the absorber measurement, some of the large pulses were trimmed, as shown in the top figure of Fig. C.2. Exceptionally, two data sets with pre-triggering with only 800 ns were removed from the measurement. The background measurement was not corrected during the analysis as the pulses were small and should not be affected.

By requiring a cut on events that the left boundary of the first peak to be greater than one sample, the trimmed events due to the wrong triggering edge could be removed. Fig. C.1 shows that with the wrong triggering edge, many events with high integral got trimmed. Their F90 values were even lower than ER as the fast component were trimmed. Fortunately, these high integral events would not contribute to the alpha signal, since their integral is larger than that by the alpha signal even being trimmed.

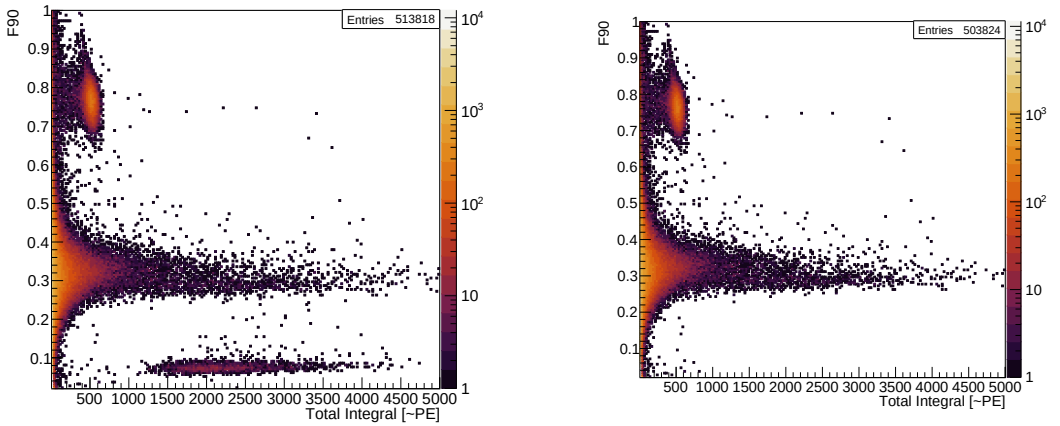

(a) No cut

(b) Trimmed events removed

Figure C.1: The two plot shows the comparison of (b) with and (a) without removing the trimmed events with the left boundary cut.

If one considers only the region of integral between 0 to 700 PE and applied the mentioned cut, most of the removed events, which are the trimmed events, are large pulses as shown in the top trace in Fig. C.2. Such a large pulse has a different pulse shape as an

alpha signal, of which a large portion of the integral concentrates in a window of around $\mathcal{O}(100\ \text{ns})$, as shown in the bottom trace in Fig. C.2. Hence, all the trimmed events should not contribute to the alpha signal.

Apart from solving the triggering edge problem of the absorber measurement, the left boundary of each event was also used to align the events when stacking the waveform of all measurements.

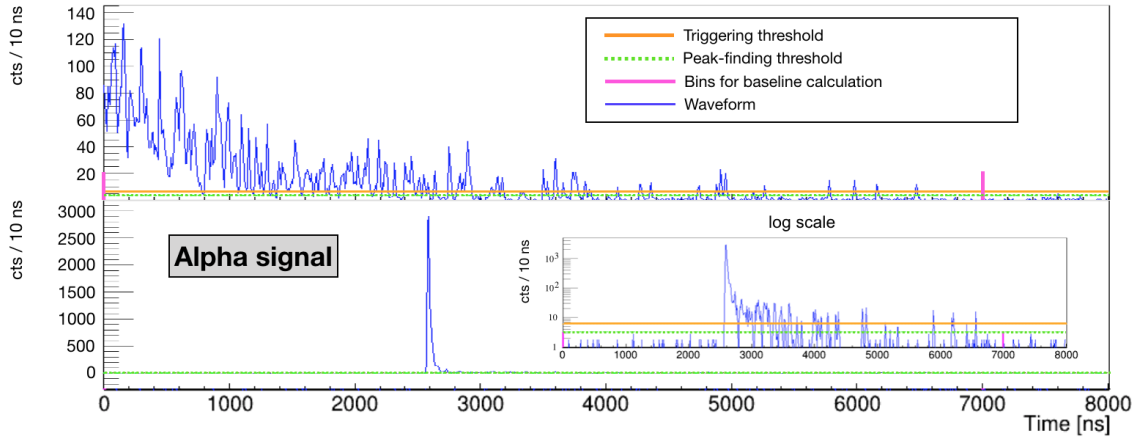

Figure C.2: Waveform from the absorber measurement. The plot below shows a typical waveform of an alpha event. The plot above shows a waveform that is trimmed due to the triggering edge problem. The triggering is at 3000 ns. Both waveforms have integrals smaller than 700 PE.

Appendix D

Detailed Procedures of Filling Liquid Argon

Before the filling, the temperature controller, PID controller, the levelmeter, and the related electronics were turned on. One also ensured if the values are expected and the slow control system functioned normally, such that the quantities were monitored throughout the filling process and data-taking.

LN2 was the cooling agent of this experiment. Hence, LN2 was prepared in a 180-liter dewar. The amount was sufficient for filling the LAr above the PTFE filler and stabilizing the system for 2 days.

The GAr bottle was first connected to LArS through a gas regulator and a pipeline, but not opened yet. The regulator was used to control the flow rate of GAr and monitored the amount of remaining GAr in the bottle. The valve and the adjustment knob was complete opened for pumping.

Before closing the cryostat, the electronic connections were checked. The pipe connections were also checked so as to avoid any potential leakage, which prevented the system from going down to the desired vacuum level. Also, all the valves were closed except the one connecting to the vacuum pump and the one connecting to the gas regulator. The HiCube 80 Eco vacuum pump by Pfeiffer Vacuum was then turned on with the turbopump initially off. When the pressure reached the vacuum level of 1 mBar using only the rough pump, the turbopump was turned on. During pumping, the pressure was monitored from the panel of the vacuum pump. With the same reason of choosing highly purified GAr, vacuuming the system was owing to the fact that the light yield would increase with a higher purity of LAr, as stated in Section 4.1.

After reaching the desired vacuum level and measuring the outgassing rate, as described in Section 4.4.2, the valve connecting the cryostat and the vaccume pump was completely closed to protect the turbopump. The valve and the adjustment knob on the regulator was immediately opened right after, so as to minimize the amount of outgassing as much as possible. The adjustment knob of the regulator was adjusted for a desired flow rate of GAr. As soon as the pressure inside the cryostat reached above 10 mBar, the pressure was

monitored through the PID controller, as the pressure readout of the vacuum pump became inaccurate.

The maximum operating pressure of the system is 2000 mBar, hence the overpressure valve was set to release at 1900mBar. When the pressure of GAr reached the level above atmospheric pressure while still below 1900 mBar, typically 1200 mBar in this experiment, the valve on the LN2 dewar was opened such that LN2 started flowing into the cooling coil.

As LN2 cooled down the gas, the lowered pressure due to the decrease in temperature was immediately compensated by the inlet of GAr from the bottle due to the presence of the regulator. Hence, the pressure inside the cryostat was decreasing slowly even when the cooling system is activated. The adjustment knob was manually turned more and more open throughout the filling so that the pressure was constantly above atmospheric pressure.

During filling, a cooling scheme which is fast yet not freezing the argon should be chosen. As the PT100 attached to the cooling coil reflects more accurately the cooling power and responses faster upon a change in the flow rate than the PT100 next to the PMT window, the former PT100 was chosen to provide the feedback to the temperature controller to control the flow rate. Also, the ramping mode was selected in the controller for a better control of the ramping rate. If the LAr starts to freeze, the efficiency of turning GAr to LAr decreases and the solid Ar grows continuously. Since the condensation point depends on the pressure in the system [5], both the temperature and the pressure was monitored to avoid the temperature going below the condensation point of LAr at the corresponding pressure. Fig. D.1(a) and (b) show the readouts of the sensors during filling.

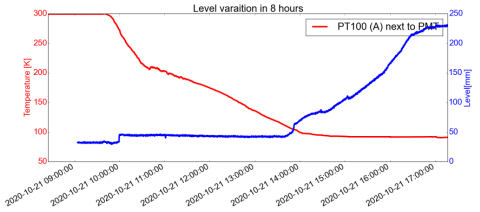

(a) Levelmeter reading

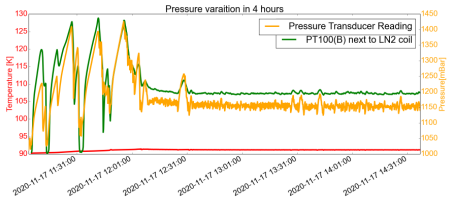

(b) Pressure and temperature

Figure D.1: (a) Blue line is the levelmeter reading while the red line is the reading of the PT100 next to the PMT. The plot shows the change in level and temperature during filling. (b) The orange line is the pressure readout; the green line is the PT100 at the cooling coil. The plot shows the system entering the post-filling stage.

After reaching the level around 220 mm, which is above the PTFE filler, the whole setup was changed to a stabilizing phase, where the valve of GAr was closed. The temperature controller was changed to received feedback from the PT100 next to the PMT and switched to the PID controlling mode. The PID values were chosen such that the controller stabilized the system.

Bibliography

[1] Gamma-ray spectrum catalog of isotopes, 2003. URL http://www.radiochemistry.org/periodictable/gamma_spectra/index.html.

[2] Characteristics of photomultiplier tubes, 2007. URL https://www.hamamatsu.com/resources/pdf/etd/PMT_handbook_v3aE-Chapter4.pdf.

[3] Upgrade 201805, 2018. URL https://www.mpi-hd.mpg.de/gerdawiki/index.php/Upgrade_201805.

[4] Argon, 2018. URL https://webbook.nist.gov/cgi/inchi?ID=C7440371&Mask=4.

[5] Saturation properties for argon — temperature increments, 2018. URL https://webbook.nist.gov/cgi/fluid.cgi?TLow=80&THigh=300&TInc=0.2&Applet=on&Digits=5&ID=C7440371&Action=Load&Type=SatP&TUnit=K&PUnit=bar&DUnit=kg%2Fm3&HUnit=kJ%2Fmol&WUnit=m%2Fs&VisUnit=uPa*s&STUnit=N%2Fm&RefState=DEF.

[6] Nitrogen, 2018. URL https://webbook.nist.gov/cgi/cbook.cgi?ID=C7727379&Mask=4.

[7] Legend-200, 2021. URL https://legend-exp.org/science/legend-pathway/legend-200.

[8] K. Abe et al. Indication of Electron Neutrino Appearance from an Accelerator-produced Off-axis Muon Neutrino Beam. *Phys. Rev. Lett.*, 107:041801, 2011. doi: 10.1103/PhysRevLett.107.041801.

[9] K. Abe et al. Constraint on the matter–antimatter symmetry-violating phase in neutrino oscillations. *Nature*, 580(7803):339–344, 2020. doi: 10.1038/s41586-020-2177-0. [Erratum: Nature 583, E16 (2020)].

[10] N. Abgrall et al. The Large Enriched Germanium Experiment for Neutrinoless Double Beta Decay (LEGEND). *AIP Conf. Proc.*, 1894(1):020027, 2017. doi: 10.1063/1.5007652.

[11] N. Abgrall et al. The Large Enriched Germanium Experiment for Neutrinoless $\beta\beta$ Decay: LEGEND-1000 Preconceptual Design Report. 7 2021.

[12] Y. Abraham et al. Wavelength-shifting performance of polyethylene naphthalate films in a liquid argon environment. *JINST*, 16(07):P07017, 2021. doi: 10.1088/1748-0221/16/07/P07017.

[13] R. Acciarri et al. Effects of Nitrogen and Oxygen contamination in liquid Argon. *Nucl. Phys. B Proc. Suppl.*, 197:70–73, 2009. doi: 10.1016/j.nuclphysbps.2009.10.037.

[14] R. Acciarri et al. Effects of Nitrogen contamination in liquid Argon. *JINST*, 5: P06003, 2010. doi: 10.1088/1748-0221/5/06/P06003.

[15] D. Q. Adams et al. High sensitivity neutrinoless double-beta decay search with one tonne-year of CUORE data. 4 2021.

[16] G. Adhikari et al. nEXO: Neutrinoless double beta decay search beyond 10^{28} year half-life sensitivity. 6 2021.

[17] P. Adhikari et al. The liquid-argon scintillation pulseshape in DEAP-3600. *Eur. Phys. J. C*, 80(4):303, 2020. doi: 10.1140/epjc/s10052-020-7789-x.

[18] P. Adhikari et al. Pulseshape discrimination against low-energy Ar-39 beta decays in liquid argon with 4.5 tonne-years of DEAP-3600 data. 3 2021.

[19] P. Agnes et al. DarkSide-50 532-day Dark Matter Search with Low-Radioactivity Argon. *Phys. Rev. D*, 98(10):102006, 2018. doi: 10.1103/PhysRevD.98.102006.

[20] F. Agostini et al. Sensitivity of the DARWIN observatory to the neutrinoless double beta decay of ^{136}Xe. *Eur. Phys. J. C*, 80(9):808, 2020. doi: 10.1140/epjc/s10052-020-8196-z.

[21] M. Agostini et al. Results on Neutrinoless Double-β Decay of ^{76}Ge from Phase I of the GERDA Experiment. *Phys. Rev. Lett.*, 111(12):122503, 2013. doi: 10.1103/PhysRevLett.111.122503.

[22] M. Agostini et al. Improvement of the energy resolution via an optimized digital signal processing in GERDA Phase I. *Eur. Phys. J. C*, 75(6):255, 2015. doi: 10.1140/epjc/s10052-015-3409-6.

[23] M. Agostini et al. LArGe: active background suppression using argon scintillation for the Gerda $0\nu\beta\beta$-experiment. *Eur. Phys. J. C*, 75(10):506, 2015. doi: 10.1140/epjc/s10052-015-3681-5.

[24] M. Agostini et al. Final Results of GERDA on the Search for Neutrinoless Double-β Decay. *Phys. Rev. Lett.*, 125(25):252502, 2020. doi: 10.1103/PhysRevLett.125.252502.

[25] M. Agostini et al. Modeling of GERDA Phase II data. *JHEP*, 03:139, 2020. doi: 10.1007/JHEP03(2020)139.

[26] M. Agostini et al. First Search for Bosonic Superweakly Interacting Massive Particles with Masses up to 1 MeV/c^2 with GERDA. *Phys. Rev. Lett.*, 125(1):011801, 2020. doi: 10.1103/PhysRevLett.125.011801.

[27] M. Agostini et al. Calibration of the Gerda experiment. *Eur. Phys. J. C*, 81(8):682, 2021. doi: 10.1140/epjc/s10052-021-09403-2.

[28] Q. R. Ahmad et al. Direct evidence for neutrino flavor transformation from neutral current interactions in the Sudbury Neutrino Observatory. *Phys. Rev. Lett.*, 89: 011301, 2002. doi: 10.1103/PhysRevLett.89.011301.

[29] V. Albanese et al. The SNO+ experiment. *JINST*, 16(08):P08059, 2021. doi: 10.1088/1748-0221/16/08/P08059.

[30] S. I. Alvis et al. A Search for Neutrinoless Double-Beta Decay in ^{76}Ge with 26 kg-yr of Exposure from the MAJORANA DEMONSTRATOR. *Phys. Rev. C*, 100(2): 025501, 2019. doi: 10.1103/PhysRevC.100.025501.

[31] C. Amsler, V. Boccone, A. Buchler, R. Chandrasekharan, C. Regenfus, and J. Rochet. Luminescence quenching of the triplet excimer state by air traces in gaseous argon. *JINST*, 3:P02001, 2008. doi: 10.1088/1748-0221/3/02/P02001.

[32] F. P. An et al. Observation of electron-antineutrino disappearance at Daya Bay. *Phys. Rev. Lett.*, 108:171803, 2012. doi: 10.1103/PhysRevLett.108.171803.

[33] G. Anton et al. Search for Neutrinoless Double-β Decay with the Complete EXO-200 Dataset. *Phys. Rev. Lett.*, 123(16):161802, 2019. doi: 10.1103/PhysRevLett.123.161802.

[34] W. R. Armstrong et al. CUPID pre-CDR. 7 2019.

[35] R. Arns. Detecting the Neutrino. *Phys. perspect*, 3:314–334, 2001. doi: 10.1007/PL00000535.

[36] L. Baudis, G. Benato, R. Dressler, F. Piastra, I. Usoltsev, and M. Walter. Enhancement of Light Yield and Stability of Radio-Pure Tetraphenyl-Butadiene Based Coatings for VUV Light Detection in Cryogenic Environments. *JINST*, 10(09):P09009, 2015. doi: 10.1088/1748-0221/10/09/P09009.

[37] A. Biland. Astro-particle physics part ib: Cosmic rays $\leq$ 10tev, 2021. URL http://ihp-pc47.ethz.ch/APP/Vorlesung.html. Lecture Slides.

[38] C. Brizzolari et al. Enhancement of the X-Arapuca photon detection device for the DUNE experiment. 4 2021.

[39] A. Brown. *Search for Elastic and Inelastic Dark Matter Interactions in XENON1T and Light Detection for XENONnT*. PhD thesis, University of Zurich, Zurich, Switzerland, 2020. URL https://www.physik.uzh.ch/dam/jcr:a9cd6398-58ad-45e9-b87d-85e8f2490d1d/abrown_thesis_final.pdf.

[40] R. Brun and F. Rademakers. Root - an object oriented data analysis framework. In *Proceedings AIHENP'96 Workshop*, Nucl. Inst. & Meth. in Phys. Res. A 389, pages 81–86, Lausanne, 1997. URL https://root.cern/.

[41] J. Calvo et al. Backgrounds and pulse shape discrimination in the ArDM liquid argon TPC. *JCAP*, 12:011, 2018. doi: 10.1088/1475-7516/2018/12/011.

[42] J. M. Corning, G. R. Araujo, P. C. F. Di Stefano, V. Pereymak, T. Pollmann, and P. Skensved. Temperature-dependent fluorescence emission spectra of acrylic (PMMA) and tetraphenyl butadiene (TPB) excited with UV light. *JINST*, 15(03): C03046, 2020. doi: 10.1088/1748-0221/15/03/C03046.

[43] C. L. Cowan, F. Reines, F. B. Harrison, H. W. Kruse, and A. D. McGuire. Detection of the free neutrino: a confirmation. *Science*, 124(3212):103–104, 1956. ISSN 0036-8075. doi: 10.1126/science.124.3212.103. URL https://science.sciencemag.org/content/124/3212/103.

[44] G. Danby, J. M. Gaillard, K. A. Goulianos, L. M. Lederman, N. B. Mistry, M. Schwartz, and J. Steinberger. Observation of High-Energy Neutrino Reactions and the Existence of Two Kinds of Neutrinos. *Phys. Rev. Lett.*, 9:36–44, 1962. doi: 10.1103/PhysRevLett.9.36.

[45] F. Deppisch. *A Modern Introduction to Neutrino Physics*. Morgan& Claypool Publishers, 2019.

[46] N. Di Marco. Searching for neutrinoless double-beta decay with GERDA. *Nucl. Instrum. Meth. A*, 958:162112, 2020. doi: 10.1016/j.nima.2019.04.066.

[47] T. Doke, A. Hitachi, J. Kikuchi, K. Masuda, H. Okada, and E. Shibamura. Absolute scintillation yields in liquid argon and xenon for various particles. *Japanese Journal of Applied Physics*, 41(Part 1, No. 3A):1538–1545, mar 2002. doi: 10.1143/jjap.41.1538. URL https://doi.org/10.1143/jjap.41.1538.

[48] G. Douysset, T. Fritioff, C. Carlberg, I. Bergstrom, and M. Bjorkhage. Determination of the Ge-76 double beta decay Q value. *Phys. Rev. Lett.*, 86:4259–4262, 2001. doi: 10.1103/PhysRevLett.86.4259.

[49] K. Eguchi et al. First results from KamLAND: Evidence for reactor anti-neutrino disappearance. *Phys. Rev. Lett.*, 90:021802, 2003. doi: 10.1103/PhysRevLett.90.021802.

[50] Y. Fukuda et al. Evidence for oscillation of atmospheric neutrinos. *Phys. Rev. Lett.*, 81:1562–1567, 1998. doi: 10.1103/PhysRevLett.81.1562.

[51] M. Fukugita and T. Yanagida. Baryogenesis Without Grand Unification. *Phys. Lett. B*, 174:45–47, 1986. doi: 10.1016/0370-2693(86)91126-3.

[52] A. Gando et al. Search for Majorana Neutrinos near the Inverted Mass Hierarchy Region with KamLAND-Zen. *Phys. Rev. Lett.*, 117(8):082503, 2016. doi: 10.1103/PhysRevLett.117.082503. [Addendum: Phys.Rev.Lett. 117, 109903 (2016)].

[53] T. Heindl, T. Dandl, M. Hofmann, R. Krucken, L. Oberauer, W. Potzel, J. Wieser, and A. Ulrich. The scintillation of liquid argon. *EPL*, 91(6):62002, 2010. doi: 10.1209/0295-5075/91/62002.

[54] M. Heisel. *LArGe – A liquid argon scintillation veto for GERDA*. PhD thesis, University of Heidelberg, Heidelberg, Germany, 2011. URL https://www.mpi-hd.mpg.de/gerda/public/2011/phd2011_MarkHeisel.pdf.

[55] A. Hitachi, T. Takahashi, N. Funayama, K. Masuda, J. Kikuchi, and T. Doke. Effect of ionization density on the time dependence of luminescence from liquid argon and xenon. *Phys. Rev. B*, 27:5279–5285, May 1983. doi: 10.1103/PhysRevB.27.5279. URL https://link.aps.org/doi/10.1103/PhysRevB.27.5279.

[56] M. Hofmann, T. Dandl, T. Heindl, and et al. Ion-beam excitation of liquid argon. *Eur. Phys. J. C*, 73:2618, 2013. doi: 10.1140/epjc/s10052-013-2618-0.

[57] M. Janecek. Reflectivity spectra for commonly used reflectors. *IEEE Transactions on Nuclear Science - IEEE TRANS NUCL SCI*, 59:490–497, 06 2012. doi: 10.1109/TNS.2012.2183385.

[58] D. Kim. Beyond the Standard Model physics prospects at the Deep Underground Neutrino Experiment. *PoS*, ICHEP2020:257, 2021. doi: 10.22323/1.390.0257.

[59] K. Kodama et al. Observation of tau neutrino interactions. *Phys. Lett. B*, 504:218–224, 2001. doi: 10.1016/S0370-2693(01)00307-0.

[60] P. Kryczynski. Pulse Shape Discrimination in liquid argon and its implications for Dark Matter searches using depleted argon. *Acta Phys. Polon. B*, 43:1509–1520, 2012. doi: 10.5506/APhysPolB.43.1509.

[61] S. Kubota, M. Hishida, and A. Nohara. Variation of scintillation decay in liquid argon excited by electrons and alpha particles. *Nuclear Instruments and Methods*, 150 (3):561–564, 1978. ISSN 0029-554X. doi: https://doi.org/10.1016/0029-554X(78)90128-3. URL https://www.sciencedirect.com/science/article/pii/0029554X78901283.

[62] M. Kuźniak and A. M. Szelc. Wavelength Shifters for Applications in Liquid Argon Detectors. *Instruments*, 5(1):4, 2020. doi: 10.3390/instruments5010004.

[63] M. Kuźniak, B. Broerman, T. Pollmann, and G. R. Araujo. Polyethylene naphthalate film as a wavelength shifter in liquid argon detectors. *Eur. Phys. J. C*, 79(4):291, 2019. doi: 10.1140/epjc/s10052-019-6810-8.

[64] W. H. Lippincott, K. J. Coakley, D. Gastler, A. Hime, E. Kearns, D. N. McKinsey, J. A. Nikkel, and L. C. Stonehill. Scintillation time dependence and pulse shape discrimination in liquid argon. *Phys. Rev. C*, 78:035801, 2008. doi: 10.1103/PhysRevC.81.039901. [Erratum: Phys.Rev.C 81, 039901 (2010)].

[65] W. Maneschg. First results from phase ii of the neutrinoless double beta decay experiment gerda. TeV Particle Astrophysics 2016, 2016.

[66] D. Mary, M. Albertini, and C. Laurent. Understanding optical emissions from electrically stressed insulating polymers: electroluminescence in poly(ethylene terephthalate) and poly(ethylene 2,6-naphthalate) films. *Journal of Physics D: Applied Physics*, 30(2):171–184, jan 1997. doi: 10.1088/0022-3727/30/2/004. URL https://doi.org/10.1088/0022-3727/30/2/004.

[67] M. Miloradovic. Emanation measurement system and gerda phase ii calibration. Master's thesis, University of Zurich, Zurich, Switzerland, 2015. URL https://www.physik.uzh.ch/groups/groupbaudis/darkmatter/theses/gerda/Master_Miloradovic.pdf.

[68] M. Miloradovic. *Characterisation of Inverted Coaxial Detectors and Calibration Source Production for the GERDA Experiment*. PhD thesis, University of Zurich, Zurich, Switzerland, 2020. URL https://www.physik.uzh.ch/dam/jcr:94fa6df0-e441-413a-a31d-59f89e375970/miloradovic_thesis.pdf.

[69] R. Mingazheva. *Calibration, Background Study, andSearch for New Physicswith the GERDA Experiment*. PhD thesis, University of Zurich, Zurich, Switzerland, 2019. URL https://www.physik.uzh.ch/dam/jcr:1c037fcf-eee7-487d-9336-4b8cc88f6710/MingazhevaThesis.pdf.

[70] J. Myslik. LEGEND: The Large Enriched Germanium Experiment for Neutrinoless Double-Beta Decay. In *13th Conference on the Intersections of Particle and Nuclear Physics*, 10 2018.

[71] R. Nakamura, H. Sambonsugi, K. Shiraishi, and Y. Wada. Research and development toward KamLAND2-Zen. *J. Phys. Conf. Ser.*, 1468(1):012256, 2020. doi: 10.1088/1742-6596/1468/1/012256.

[72] C. Ransom. *Energy Calibration for the Gerda and Legend-200 Experiments*. PhD thesis, University of Zurich, Zurich, Switzerland, 2021. URL https://www.physik.uzh.ch/dam/jcr:b1dfb03f-7d9b-4c4c-b3a7-12e9ff2e513c/Chloe_Thesis.pdf.

[73] A. D. Sakharov. Violation of CP Invariance, C asymmetry, and baryon asymmetry of the universe. *Pisma Zh. Eksp. Teor. Fiz.*, 5:32–35, 1967. doi: 10.1070/PU1991v034n05ABEH002497.

[74] F. Salamida. Search of neutrinoless double beta decay with gerda. LXX International conference "NUCLEUS – 2020. Nuclear physics and elementary particle physics. Nuclear physics technologies", 2020. URL https://indico.cern.ch/event/839985/contributions/3986292/attachments/2121707/3571242/Gerda_salamida_Nucleus2020.pdf.

[75] E. Segreto. Properties of Liquid Argon Scintillation Light Emission. *Phys. Rev. D*, 103(4):043001, 2021. doi: 10.1103/PhysRevD.103.043001.

[76] M. Suzuki, J. zhi Ruan(Gen), and S. Kubota. Time dependence of the recombination luminescence from high-pressure argon, krypton and xenon excited by alpha particles. *Nuclear Instruments and Methods in Physics Research*, 192(2): 565–574, 1982. ISSN 0167-5087. doi: https://doi.org/10.1016/0029-554X(82)90874-6. URL https://www.sciencedirect.com/science/article/pii/0029554X82908746.

[77] M. Walter. *Background Reduction Techniques for the Gerda Experiment*. PhD thesis, University of Zurich, Zurich, Switzerland, 2015. URL https://www.physik.uzh.ch/groups/groupbaudis/darkmatter/theses/gerda/PHD_Walter.pdf.

[78] C. Wiesinger. Post-upgrade performance of GERDA Phase II. *J. Phys. Conf. Ser.*, 1468(1):012109, 2020. doi: 10.1088/1742-6596/1468/1/012109.

[79] F. L. Wilson. Fermi's Theory of Beta Decay. *Am. J. Phys.*, 36(12):1150–1160, 1968. doi: 10.1119/1.1974382.

[80] A. J. Zsigmond. LEGEND: The future of neutrinoless double-beta decay search with germanium detectors. *J. Phys. Conf. Ser.*, 1468(1):012111, 2020. doi: 10.1088/1742-6596/1468/1/012111.

[81] P. A. Zyla et al. Review of Particle Physics. *PTEP*, 2020(8):083C01, 2020. doi: 10.1093/ptep/ptaa104.